Heat Transfer and Convective Structure of Evaporating Films under Pressure-Modulated Conditions

Juan Carlos Gonzalez

A dissertation submitted in partial fulfillment of
the requirements for the degree of

Doctor of Philosophy

University of Washington
2015

Reading Committee:
James C. Hermanson
Robert Breidenthal
Dana Dabiri

Program Authorized to Offer Degree:
Aeronautics and Astronautics

In presenting this dissertation in partial fulfillment of the requirement for the doctoral degree at the University of Washington, I agree that the Library shall make its copies freely available for inspection. I further agree that extensive copying of the dissertation is allowable only for scholarly purposes, consistent with "fair use" as prescribed in the U.S. Copyright Law. Requests for copying or reproduction of this dissertation may be referred to ProQuest Information and Learning, 300 North Zeeb Road, Ann Arbor, MI 48106-1346, 1-800-521-0600, to whom the author has granted "the right to reproduce and sell (a) copies of the manuscript in microform and/or (b) printed copies of the manuscript made from microform."

Signature 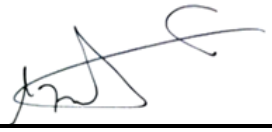

Date **3/19/2015**

University of Washington

Abstract

Unsteady Evaporating Films under Pressure-Modulated Conditions

Juan Carlos Gonzalez

Chair of Supervisory Committee:
Professor James C. Hermanson
Aeronautics and Astronautics

This work examines the fluid mechanical and heat transfer characteristics of evaporating films under cyclical superheat conditions. This research was motivated by the need to further understand the instability drivers in films undergoing unsteady and cyclical evaporation. The superheat was controlled modulating the system pressure. An isolated test cell allowed the films to evaporate into their own vapor without non-condensable present. A non-intrusive thickness measurement technique was used to yield dynamic heat flux measurements. A double pass schlieren system was employed to capture convective structures. System temperature and pressure measurements completed the diagnostics.

The primary conclusions are briefly summarized as follows:

- The evolution of thermal profile within evaporating films has a strong impact on the development of convective structure and heat transfer. In some cases convective

structure appears within the film under pressure-modulated conditions even when the evaporation intervals are sufficiently short that conduction is expected to be the only heat transfer mode within the film.

- Convective structure appears to persist in many cases even after evaporation is stopped.
- Stopping the evaporation for short time intervals appears to have a negligible effect on the temperature profile in the film.
- Complex, multi-wavelength convective structure behavior can be induced through cyclical superheating of the films.
- A modest gain in short-term heat flux is achievable under some pressure-modulated conditions.
- Surface instabilities of quasi-steady evaporating films do not lead to an increase in the evaporation rate.
- Reduced gravity tests were seriously compromised by unsteady g-levels and g-jitter.

Table of Contents

List of Figures

List of Tables

Acknowledgment

To say that I have learned quite a few things during the Ph.D. process is a slight understatement. However, nothing is clearer to me now than the fact that no one reaches the end of a Ph.D. by him or herself. It is always a group effort, and my experience was no exception. There are countless people who without their help, this journey would have been simply impossible and to whom I will be forever grateful. There are also a greater number of people who made the process easier and more bearable at times when the end seemed out of reach. These are just some of those individuals.

Mr. Robert Gordon was a never ending source of knowledge and guidance with hardware set-up. Mr. Art Blair and Ms. Fiona Spencer and Mr. Carl Knowlen were just as indispensable. Mr. Denis Peterson and Mr. Dzung Tran provided invaluable help with the design and machining of parts.

The entire administrative staff, Ms. Carmela Halos, Mr. Dave Erickson, Ms. Jenny Park, Ms. Kimberly Maczko, Mr. Patrick Gibbs, Ms. Lynn Catlett, Mr. Jack Ross, Mr. Brian Leaverson, Mr. Josh Bean, Mr. Ed Connery were an enormous help in coordinating just about everything, from travel arrangements, to shipping and receiving, to technical help with computers and general hardware. Their help allowed my efforts to stay focused on the research. Ms. Wanda Frederick deserves a special mention since she was involved in my UW experience from the very beginning to the very end. I would simply not be here without her.

This research, of course would not have been possible without the support from NASA, under the cooperative agreement NNX09AL02G.

Several NASA personnel at Glenn and Johnson Space Centers were also essential to the completion of this project. None exemplify this dedication more than out technical contact, Mr. Eric Golliher, who went above and beyond to help every step of the way.

The entire department faculty, all of whom I went to for help at one point or another, and particularly those who took time to help as members of my committee, Prof. Eli Livne, Prof. Alberto Aliseda, Prof, Dana Dabiri and Prof. Robert Breidenthal.

Our collaborating team and Michigan Tech, in particular Prof. Jeff Allen, provided the numerical simulation guidance needed during most of the research.

Everyone at the fluids lab Wei Tien, Greg Rixon, Eric Lin, Ying-Hao Liao, Jun Kim, Arun Tamilarasan, and all the students who volunteered their time to help advance this project. The list is simply too big, but their efforts will be forever appreciated.

Dr. Jeramy Kimball, my predecessor, deserves an enormous amount of credit for all his helpful input and guidance during this time. It would have taken an unreal amount of time to culminate my studies without his help.

Finally I would like to thank Prof. James Hermanson. His patience and dedication are hard to put into words. He made this journey both challenging and exciting, and I will be forever indebted to him. There is really no other adviser I could envision who could have led me here today.

Chapter 1. Introduction

Evaporation is a widely used phenomenon in a great number of engineering problems. Some of those applications involve fuel vaporization [0, [2]], flame propagation over liquid fuels [[3], [4]], hardening of plastics [[5]], drying and cooling [[6]]. An example is the increasingly compacting trend of modern electronic components, which inevitably requires more effective means of heat rejection. The high heat flux and constant temperature associated with phase change can be exploited in order to meet this challenge in thermal control [[7]]. Several thermal control systems [[8]] have been created which take advantage of the aforementioned high heat flux levels enabled by phase change. Some of these systems include capillary pumped loops [[9]] and loop heat pipes [[10], [11]]. Within the field of evaporation and phase change, film evaporation in particular is of special importance for many industrial processes such as crystal growth in semi-conductor materials and texturing of surfaces in magnetic storage devices [[3]]. The flat evaporating film, however complex, is much simpler than many other cases involving phase change such as evaporating droplets, flow in heat exchangers and forced convection flows in general. Therefore, achieving a greater understanding of the evaporation phenomena may lead to the successful developments of new and improved techniques of heat rejection.

Numerous studies of the fundamentals of evaporation have been conducted [[2], [12], [13], [14], [15]], including evaporation of stagnant films, [[13], [16], [17]], falling films, [[18], [19]], climbing films [[20]] and heat pipes [[9]]. Evaporation is an extremely complicated phenomenon, involving the combined and often competing effect, of several physical mechanisms. For example, the body force associated with the changes in density due to bulk heating of the liquid can lead to instabilities [[21]]. Thermocapillary traction also can also play

an important role in film evaporation [[9], [11]]. Also, instabilities can be caused by the destabilizing effects of mass loss and vapor recoil during evaporation [[19], [22]].

The current investigation studies the physical phenomena associated with thin films undergoing phase change under transient conditions. This contrasts with the bulk of research conducted in evaporating films to date, which have involved evaporating films under steady or quasi-steady (QS) conditions, meaning, films where the temperature difference between the liquid surface and the bottom is held at a constant value. Most of the work in this investigation focuses on the effects of cycling the superheat between a finite value and a near zero level. For the current work, superheat will be used to refer to the degrees above the vapor saturation temperature. One focus of the work is whether the time-averaged rate of heat rejection might be maximized through the use of transient evaporation, in particular, achieving a net gain when compared to QS evaporation.

The rest of this chapter consists of a theoretical background, highlighting the most relevant experimental and theoretical work that studied convective instabilities in liquid films.

1.1 Theoretical Background

The convective behavior of liquid films undergoing heating and/or phase change has been comprehensively studied for over a century. The first experiments were developed by Bénard [[23]]. Rayleigh expanded on the Bénard's experiments and performed some improved theoretical analysis of the phenomena [[24]]. Since then, our understanding of the phenomena has increased considerably. Nevertheless, there is still no comprehensive theory on the exact behavior of convective structures, heat flux, and overall stability of convective films. For example, there is evidently still no definitive explanation of why the preferential steady pattern in many cases is the hexagonal cell [[25]]. Equally, no explanation exists that can adequately

explain the interaction between subcritical patterns observed at lower Rayleigh numbers when convective structures are not fully developed and are, generally induced by the shape of the boundary of the test geometry (square, circular, etc.), and the super-critical cells hexagonal cells [[25]].

It is relevant to discuss initially the classical case, that is, the nature of the evolution of film stability for the case of *non-evaporating* films. This naturally leads to a discussion of the evolution of film stability for the case of *evaporating* films, which then leads into a brief discussion of the heat transfer of evaporating films.

The fundamental nature of both buoyancy-driven and surface-tension driven fluid instabilities can be considered by the following derivation of Koschmieder [[25]]. Beginning with convective heat transfer theory, in which a thin fluid layer is heated from below and/or cooled from above, the governing equations include continuity,

$$\frac{\partial \rho}{\partial t} = \nabla \cdot (\rho \mathbf{v}) \,, \qquad \text{Eq. 1.1}$$

where ρ represents the fluid density and $\boldsymbol{v}$ is the fluid velocity vector. The Navier-Stokes equation is

$$\rho \frac{\partial \mathbf{v}}{\partial t} = -\nabla p + \rho \mathbf{g} + \mu \nabla^2 \mathbf{v} \,, \qquad \text{Eq. 1.2}$$

where p is the pressure, g the gravitational acceleration, and μ the dynamic viscosity. The equation of thermal conduction ignoring viscous dissipation and assuming constant pressure is

$$\frac{dT}{dt} = \alpha \nabla^2 T \quad , \qquad \text{Eq. 1.3}$$

in which α is the thermal diffusivity. A common simplification to the body force term in the Navier-Stokes equation for the case of small density variations is to relate the density changes to temperature changes linearly, commonly known as the Boussinesq approximation

$$\rho = \rho_0\left(1+\beta\Delta T\right), \qquad \text{Eq. 1.4}$$

where β is the volumetric expansion coefficient. The Boussinesq approximation for current purposes means that the material property changes are negligible given a small temperature variation in the liquid phase, and that density changes due to temperature only influence the fluid motion in vertical direction. The equations for a fluid film at rest are thus

$$\mathbf{v} = 0, \quad \frac{d^2T}{dz^2} = 0, \quad \frac{dp}{dz} = \rho_0 g\left[1-\beta\left(T(z)-T_0\right)\right], \qquad \text{Eq. 1.5}$$

with ρ_0 representing the density of the fluid at the initial temperature T_0. With the use of the following non-dimensional parameters

$$x_i' = \frac{x_i}{d}, \quad t' = \frac{\alpha t}{d^2}, \quad u' = \frac{du}{\alpha}, \quad \theta' = \frac{\beta g d^3\theta}{\nu\alpha}, \quad p' = \frac{pd^2}{\rho_0\alpha^2}, \qquad \text{Eq. 1.6}$$

where u is a horizontal velocity component, θ is an infinitesimal deviation in the vertical linear temperature distribution, ν is the kinematic viscosity and d is the depth of the fluid, the governing equations become simply

$$\nabla\cdot\mathbf{v} = 0 \qquad \text{Eq. 1.7}$$

$$\frac{\partial\mathbf{v}}{\partial t} = -\nabla p + Pr\ \theta\mathbf{e}_z + Pr\ \nabla^2\mathbf{v} \qquad \text{Eq. 1.8}$$

$$\frac{\partial\theta}{\partial t} = \nabla^2\theta + Ra\cdot w, \qquad \text{Eq. 1.9}$$

where w is the vertical velocity component and $\mathbf{e}_z$ is the unit vector in the vertical direction. It should be noted that equation 1.7 are in dimensionless form. The prime symbols after the variables were dropped for mathematical convenience. Ra is the Rayleigh number defined as

$$Ra = \frac{\beta g \Delta T d^3}{\nu \alpha}, \qquad \text{Eq. 1.10}$$

which represents the ratio of buoyant to conductive heat transfer. *Pr* is the Prandtl number defined as

$$Pr = \frac{\nu}{\alpha}, \qquad \text{Eq. 1.11}$$

and it represents the ratio of the momentum diffusion due to viscosity to the thermal diffusion rate. After eliminating the pressure, horizontal velocity components, and the infinitesimal deviation of normalized temperature from the originally linear vertical temperature distribution, θ, the result is the following equation, which focuses on the vertical velocity *w* only

$$\left[\frac{\partial}{\partial t} - \nabla^2\right]\left[\frac{1}{Pr}\frac{\partial}{\partial t} - \nabla^2\right]\nabla^2 w = Ra \cdot \nabla_2^2 w \qquad \text{Eq. 1.12}$$

where ∇_2^2 is the two-dimensional Laplace operator $\partial^2/\partial x^2 + \partial^2/\partial y^2$. The boundary condition on a rigid surface is

$$\theta = 0, \qquad w = \frac{\partial w}{\partial z} = 0. \qquad \text{Eq. 1.13}$$

With some mathematical manipulation [[25], [26]], and the aid of the two-dimensional wave equation

$$\nabla_2^2 f(x,y) + a^2 f(x,y) = 0, \qquad \text{Eq. 1.14}$$

where *a* is the wave number, equation 14 reduces to

$$\nabla^6 w = Ra \nabla_2^2 w, \qquad \text{Eq. 1.15}$$

Skipping over some details [[25], [26]], the resulting solution for the critical *Ra* number is given by

$$Ra = \frac{(\pi^2 + a^2)^3}{a^2\{1 - 16a\pi^2 \cosh^2(a/2)/[(\pi^2 + a^2)^2(\sinh a + a)]\}}, \qquad \text{Eq. 1.16}$$

The result is plotted in Fig. 1.1 where the minimum determines the critical *Ra* number, which can be thought of as the number at which Rayleigh-Bénard (*RB*) convection is expected to occur. This is in fact something of an oversimplification of the problem in some cases, since it is known that there is important sub-critical behavior, such as subcritical rolls along the boundary [[27]]. The linear approximation is also a very crude assumption in some cases, such as in very volatile films which undergo very rapid evaporation. However, the linear approximation is appropriate for the modestly-heated, evaporating films considered in this research. It should also be noted that the critical *Ra* number just derived predicts the level at which convection within the entire film can be expected to commence, with or without the presence of evaporation.

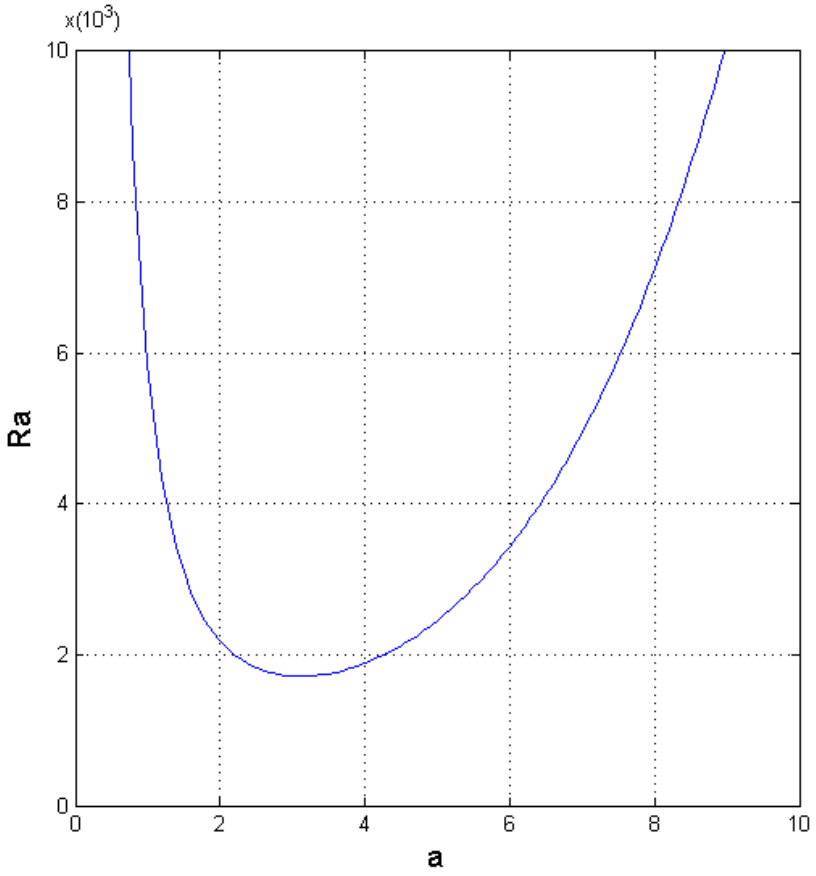

Figure 1.1. Neutral *Ra* number as a function of wave number. The minimum on the curve corresponds to the critical Ra number for non-evaporating films with a flat wall at the upper boundary. The stable region lies below the curve whereas the unstable region lies above. *Rac* = 1707 and *ac* =3.117 for this case.

For the case of Marangoni-Bénard (*MB*) convection, which is surface-tension driven, a similar procedure using linear theory can be followed in order to obtain the critical Marangoni number at which the flow instability is guaranteed to take place. The Marangoni number *Ma* can be defined as

$$Ma = \frac{\partial \mathrm{S}}{\partial T}\frac{\Delta T d}{\rho \nu \alpha}\ , \qquad \text{Eq. 1.17}$$

where *S* is the surface tension. The corresponding solution for the critical *Ma* number is

$$Ma = \frac{8a(a\cosh a + Bi\cdot\sinh a)(a - \sinh a\cosh a)}{a^3\cosh a - \sinh^3 a}\ , \qquad \text{Eq. 1.18}$$

where $Bi = hd/k$ is the Biot number, h being the heat transfer coefficient of the film. Fig. 1.2 shows the neutral stability plots for different Biot numbers. This solution was first obtained and plotted by Pearson [[28]] and it is only appropriate when considering a film on a thermally conductive wall. A slightly different solution is needed for the insulating wall case. Nield [[29]] accomplished this by combining buoyancy and surface tension into a model that represented both *RB* and *MB* convective effects. It should also be noted that since the *RB* convection scales with the cube of film thickness d while *MB* convection scales linearly with d, *RB* requires a smaller ΔT for thicker films, while *MB* is dominant in thinner fluid layers, when all other conditions are constant. This has been extensively validated experimentally for the case of heated films not undergoing evaporation.

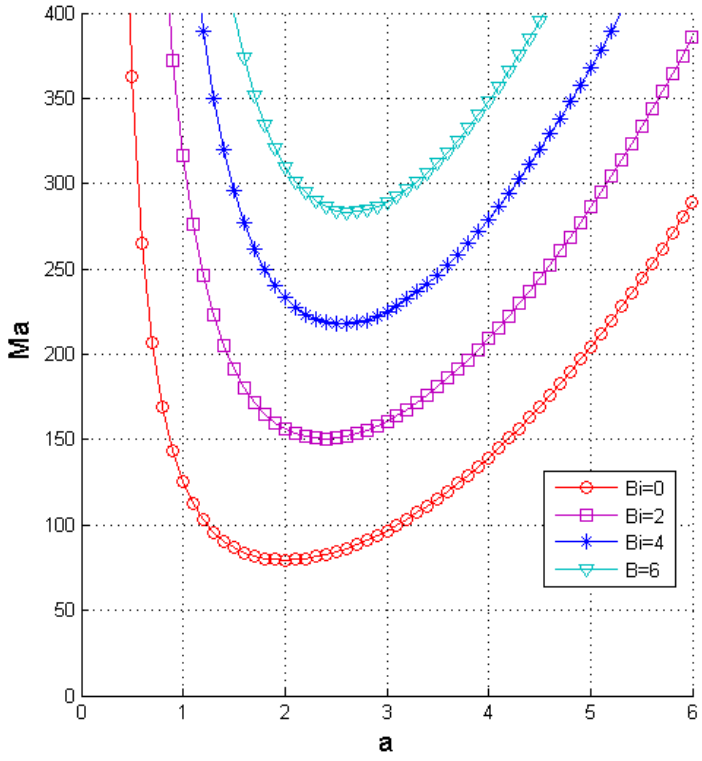

Figure 1.1. Neutral stability plots of *Ma* number as a function of wave number for different Biot numbers.The minima give the critical conditions for non-evaporating films, with a flat-wall at the upper boundary.

1.2 Heated Films with Phase Change (Evaporation)

The previous discussion focuses, as have the bulk of the experiments of thin, heated liquid layers to date, on the stability analysis of non-evaporating films. Stability analyses of evaporating films differ considerably from the previous case. For example, thermocapillary traction, which can be a considerable driving factor for the case of heated films, and the cause of *MB* convection, does not appear to be significant in liquid films when phase change is involved. This is due to the inherent temperature equilibrium effects induced by the evaporation, which suppresses temperature variation across the liquid surface. This is in close agreement with Kimball [[30]], who reported that significant variations in the *Ma* number did not have a measurable impact on the heat flux, concluding that thermocapillary effects had a negligible effect on evaporating films.

The lack of thermocapillary traction for evaporating films just mentioned does not imply that *RB* convection becomes the only instability driver in a film undergoing phase change. In fact, the coupling of hydrodynamic effects and phase change can generate instabilities that can lead to convective structures on the surface of the film, internal convective cells, or can even result in perturbations of the film thickness [[31]]. These instabilities are generally classified in short-wavelength, meaning that they are comparable in size to film thickness, and long-wavelength, in cases that there are many times greater film thickness [[31]]. Transitions between short to long-wavelength instabilities as films thins down due to evaporation have been reported. These transitions can result in dynamic interface structures, including film rupture [[31]] Numerical simulations to predict the behavior of film stabilities were conducted by Narendranath *et al.*, by solving a liquid evolution equation, which included terms to account for the effects of surface tensions, gravity, evaporation, vapor recoil, thermocapillarity and disjoining pressure.

The equation was solved until film rupture was reached, for both zero gravity and terrestrial gravity levels. Since gravity has such a considerable stabilizing effect, simulations of similar film conditions (superheat, liquid type, etc.) carried out under zero gravity levels, would expose phenomena that can impact the stability such as vapor recoil, and thermocapillary traction. Although the focus of Narendranath, *et al.* was on microgravity stability, the reported results highlight the complexity added when considering evaporating films due to the several physical phenomena taking place.

1.3 Heat Transfer in Evaporating Films

The Nusselt number, *Nu* is the fundamental parameter that characterizes the effectiveness of convective heat transfer. It is defined as

$$Nu \equiv \frac{hL}{k}, \qquad \text{Eq. 1.19}$$

where h is the convective heat transfer coefficient, L is the characteristic length (typically the film thickness) and k is the thermal conductivity of the liquid film. Hinkenbein and Berg [**Error! Reference source not found.**] published an extensive study of heat transfer through the non-evaporating liquid films, with a free surface. The authors found that for relatively thick films, the *Nu* numbers is a relatively weak function of the *Ra* number. This is particularly the case for *Ra* numbers much larger than the critical value of 1707. For films near or below the critical *Ra* number, the *Nu* number becomes a function of film thickness (for comparable *Ra* numbers). The authors also found that the *Nu* number fluctuates slightly around unity for very thin films, or films subjected to modest heating, which is indicative of a stagnant film.

Heated films undergoing evaporation add another layer of complexity to an already rich problem. Zhang *et al.* [[33]] performed a comprehensive study of evaporating layers, though

there were some limitations in the measurement techniques used to measure the film temperatures, and the experiments were restricted to a limited range of experimental times. In their study, the authors evaporated the working fluid situated on a polished copper surface into ambient air. The temperature profile through the liquid layer was measured with an array of micro-thermocouples. The film thickness was measured with a needle gage touching the film surface. One interesting result from that research was that, even when the liquid film was cooled from below, transient convective structures were still present.

Some authors had reported the presence of transient changes to the temperature profile within the film, as well as transient convective behavior. Zhang's results were limited by capabilities of the measurement techniques, as was previously mentioned. Other studies did not go much further than simply reporting on the observation of transient phenomena [[34]]. Arguably, one of the most in-depth studies of films evaporating into their own vapor to date was produced by Kimball [[30]]. The basic experiment consisted of films (both quasi-steady and transient) evaporating into their own vapor. This configuration provided a considerable simplification over previous studies in which films evaporated into air. Kimball's experiment hence eliminated complications due to diffusion through non-condensable gases. In addition, the pure liquid and vapor approach also allows for a precise measurement of saturation conditions because it removes any uncertainties introduced by partial pressures of vapor/non-condensable mixture. Kimball also considerably improved the quality of the measurement technique by developing a set of non-intrusive diagnostics tools which allowed for an extremely accurate calculation of the film thickness and evaporation rate without risking disturbing the liquids.

For quasi-steady evaporating films, Kimball found the relation between heat flux and *Ra* number (Fig. 1.3) which was in close agreement with those of Villaroel [[35]]. Both studies

found the *Nu* number was essentially unity for *Ra* number values below the critical threshold of 1707. Above that, the *Nu* number rose sharply, reaching a value of around 2 at a *Ra* number of 4500. The *Nu* number continued to increase, though more slowly, for higher *Ra* numbers.

Kimball also reported on the evolution of the convective structure for quasi-steady evaporating films (Fig 1.4). The images were captured by a schlieren method, and correspond to an evaporating film starting at approximately 2.7 mm. Initial dynamic and open structures (Image A) with a *Ra* number of 3.2×10^4 give way to more stable, closed structures in (Image B) at a *Ra* number of 1.1×10^4. It should be noted that these cells most closely resembled the hexagonal cells typically associated with *RB* convection. The structures then began to transition at a *Ra* number of 4500 (Image C), to a long toroidal rolls and concentric rings, completing the transition in Image D, with a corresponding *Ra* number of 2200. The toroidal patterns then pinched off into smaller, closed cells (Image E) at a *Ra* number of 1700. This value of *Ra* number is slightly below the critical threshold, which explains why the structures lasted only a few seconds before disappearing, leaving a seemingly quiescent liquid layer. The instability wavelength decreased continuously with film thickness, although the rate of change was faster after the point corresponding to Image C.

Kimball also conducted experiments for films undergoing transient evaporation, meaning films in which the superheat is impulsively applied. Two distinct rises in heat flux were reported, each with peak values as much as 2-3 times higher than the heat flux seen under quasi-steady evaporation conditions (Fig, 1.5). The first peak in the heat flux occurred approximately 1 second after the film was subjected to the impulsive superheating and it was reported to be associated with conductive heat transfer between the relatively warmer film and the saturation temperature at the fluid interface. The second peak in heat flux occurred typically around 11

seconds after superheat was applied, it coincided with a significant change in the wavelength of the observed convective structure. Kimball found that there was no significant heat flux rise at the apparent onset of convection, though the cause for this observation was not apparent.

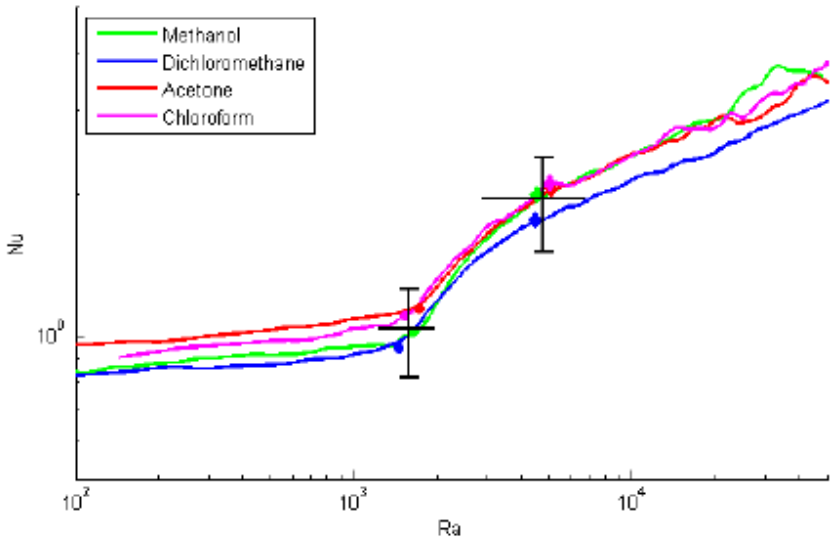

Figure 1.2. Dependence of buoyancy on heat flux. Note the near-constant value of *Nu* number below the critical *Ra* number [30].

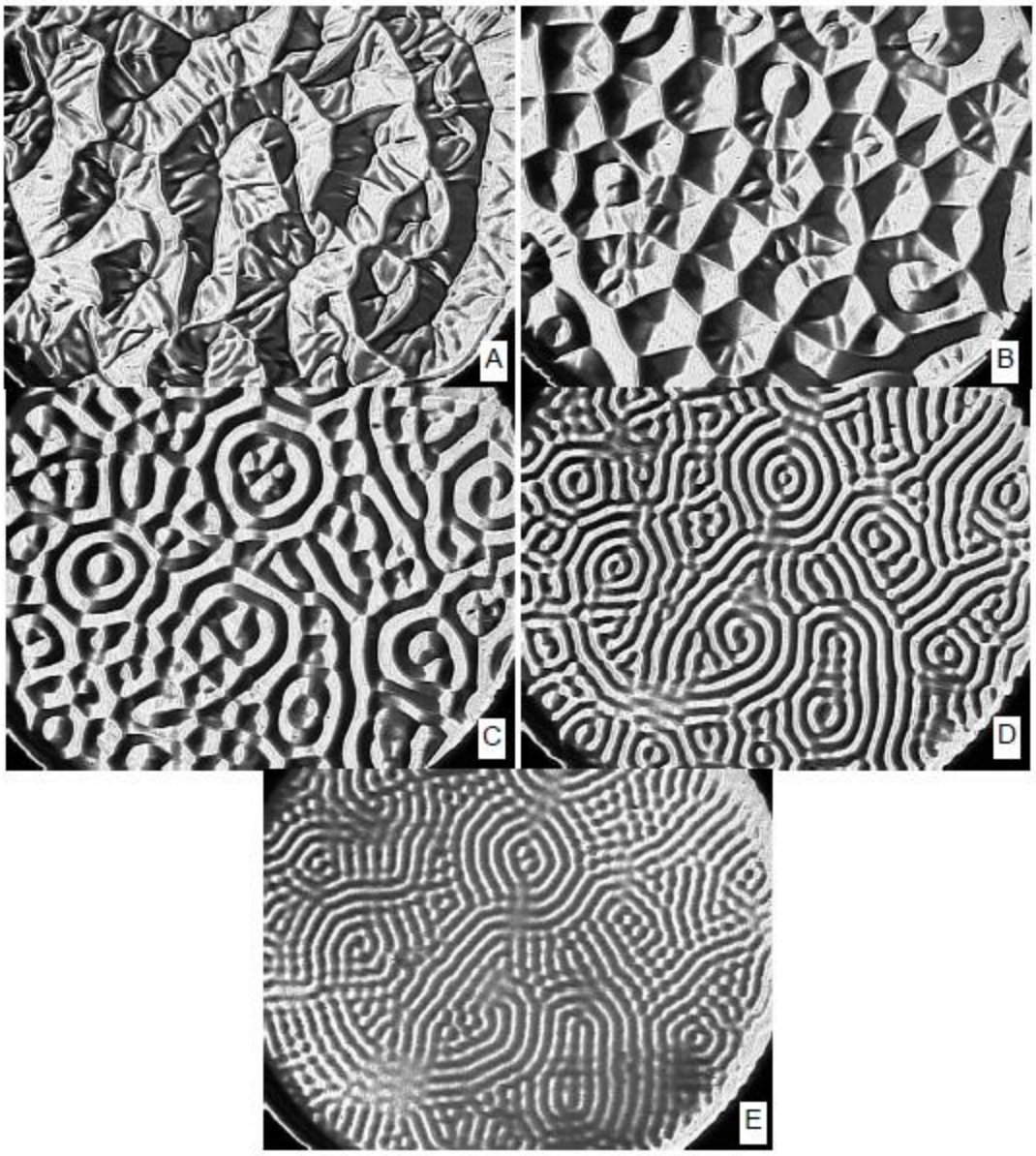

Figure 1.3. Convective structure evolution of an evaporating liquid layer of dichloromethane, between 2 mm (A) and 0.5 mm (E).

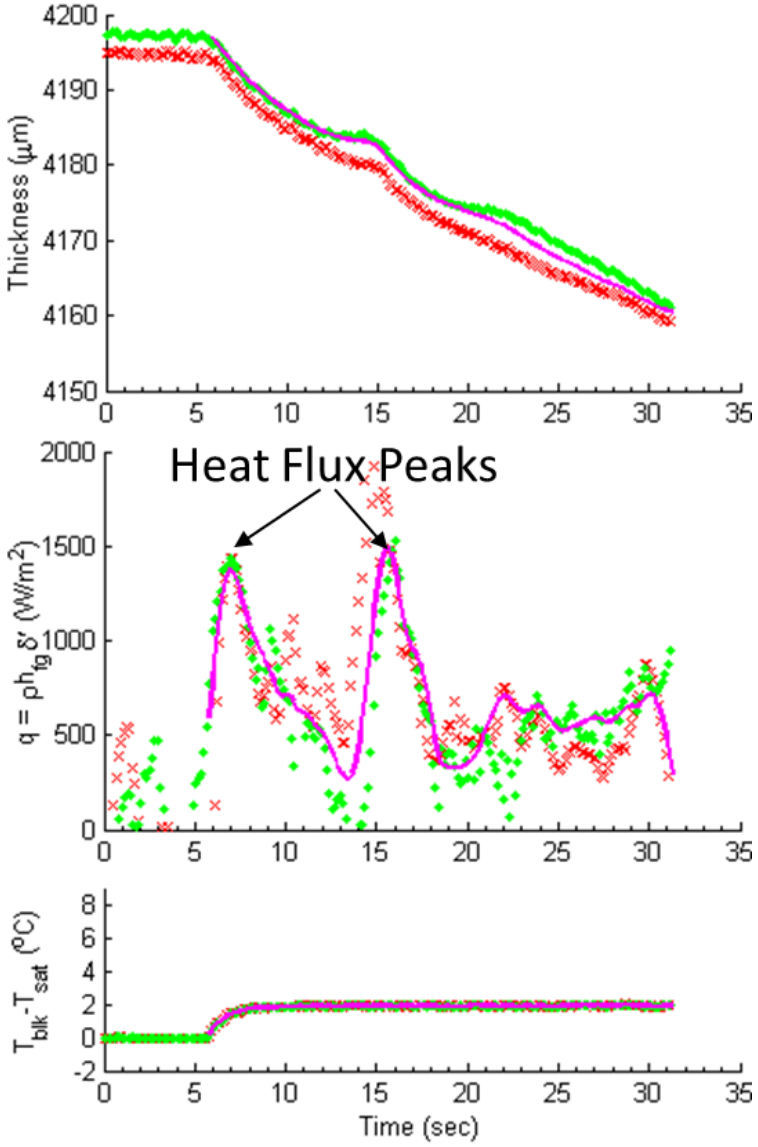

Figure 1.4. Trends in thickness (top), heat flux (middle) and superheat (bottom) for a film evaporating under impulsive superheat conditions.

1.4 Research objectives

There were several overall study objectives during this research. One was to study the heat flux under unsteady evaporation conditions, and the evolution of the convective structures. It was also relevant to research the behavior of unsteady, evaporating films under reduced-

gravity conditions, where the effects of buoyancy are removed, potentially revealing other, weaker effects on film behavior, such as thermocapillary traction and vapor recoil. More detailed research into the heat transfer behavior during the apparent conductive and convective regimes was deemed equally relevant. There was also a technical aspect of this research which sought to investigate conditions under which a net gain in the time-averaged heat flux might be achieved.

The research questions addressed in this work can be summarized as follows.

1. What are the changes in the convective behavior under non-stationary conditions?
2. How is the film stability impacted by the evaporation process?
3. How do the convective structures within unsteady evaporating films evolve into the structure reported for quasi-steady evaporating films?
4. How do the changes in convective structure impact the surface heat flux?
5. How do unsteady evaporating film convective and heat transfer behavior changes under reduced-gravity conditions?

Research questions 1 through 3 will be covered in sections 3.1 through 3.7, and 3.9. Chapter 4 will be dedicated entirely to examining research question 5. The research questions just listed can be further focused into key specific questions and issues to be explored in the current research, as outlined below:

- How does the convective structure develop under cyclical, transient evaporation conditions?
- How do the convective structures and heat transfer evolve over the course of multiple cycles as the level of superheating and evaporation is modulated?

- How the convection in the evaporating films suppressed as superheating is removed?
- Does taking advantage of the reported heat flux spikes in films undergoing evaporation under transient conditions lead to a higher net heat transferred when compared to quasi-steady conditions?
- If a net heat transfer gain is possible, how would the boundary conditions have to be modulated in order to achieve it?
- To what extent do surface waves impact the rate of evaporation?
- What are the differences in convective and heat transfer behavior for films undergoing unsteady evaporation under reduced gravity conditions compared to standard gravity?

Chapter 2. Experimental Set-Up

2.1 Experimental System Overview

The experimental system was designed to carry out controlled evaporation of a planar, liquid film into its own vapor under a range of specific experimental conditions including quasi-steady, impulsively-changed, and modulated-superheat conditions. The superheat level within the film, for a given wall temperature, was varied by dynamically controlling the system pressure as described later in this section. The superheat level, however, varies in a non-trivial way in response to the system pressure change. The experimental system can be divided into the following sub-systems: fluid handling, diagnostics, data acquisition systems, vibration isolation and ventilation. These components are discussed further below.

Two different experimental set-ups were used for the experiments reported here. One was specifically designed for reduced-gravity experiments aboard NASA's parabolic-trajectory aircraft, and will be discussed further in Chapter 4. The reduced-gravity experiment had to rapidly control the system's thermodynamic conditions due to critically time-limited test durations. Since these limitations did not apply to laboratory experiments, the reduced-gravity system was used on a limited basis in lab-based experiments. The bulk of the laboratory experiments were conducted using an experimental setup similar to that previously used by Kimball [[30]]. That system will be the focus of the description in this section. It is worth mentioning however, that both systems are very similar in terms of their basic components (isolated test chamber, temperature-controlled evaporating surface, etc.). The diagnostics systems, schlieren, ultrasound, and thermodynamic measurement devices are virtually identical and interchangeable between both versions of the experimental set-ups.

2.2 Fluid Handling System

The main units of the fluid handling system were the test chamber, the vapor generator, and the exhaust system. A photograph of the test chamber/vapor generator setup is shown in Figs. 2.1-2.3. The vapor generator consisted of a glass flask with an aluminum flange the top. This flange contained several ports which served as fluid inlet and outlet lines, and a temperature probe. The working fluid for all tests was neat dichloromethane (DCM) (CH_2Cl_2). The DCM liquid was poured into the vapor generator then heated with an electric heater coiled around the vapor-generator chamber and controlled with a Digi-Sense closed-loop temperature controller (Model Number 89000-00). As the liquid was heated, vapor was generated and delivered to the test chamber as needed. The set temperature inside the vapor generator was closely monitored to achieve the desired experimental conditions in the test chamber, since this set temperature had a marked effect on the experimental outcome, such as nucleation and hydrodynamic disturbances of the liquid film. The temperature of the liquid inside the vapor generator typically fluctuated by less than ±1.5 °C.

The test chamber is where the evaporating liquid films resided. The test chamber used in the lab consisted of a tubular Teflon body, a cylindrical copper block with a planer surface on which the evaporating film was situated, and a glass window which serves as an optical port. The Teflon wall and the copper plate mated at an angle of approximately 50 degrees (see Fig. 2.4). This geometry was implemented to minimize any effects of a liquid meniscus at the film boundary [[30]]. The optical window was made from standard, 7/32 inch (5.56 mm)-thick tempered glass, which allowed for double-pass schlieren imaging. The test chamber was held together by two aluminum plates and threaded rods which provided compression sufficient to seal the O-rings and isolate the system.

The copper block on which the evaporating film resided was central to the experiment. Previous FEM analysis [[30]] verified that the copper plate provides a sufficiently uniform temperature and heat flux at the surface, with expected deviations less than 0.1 °C. The copper surface was lapped, polished, and then plated with a layer of nickel and then gold. The gold plating guarantees a non-reactive surface while also providing a highly-reflective surface to facilitate optical imaging. The flatness of the evaporating surface was comparable to that of Kimball, which cited a surface flat to ½ wave of visible light, and smooth to 5nm. The copper plate had 23 ports machined into the bottom, opposite to the surface on which the evaporating film resided, for ultrasound transducers for thickness measurements at different locations (the ultrasound technique is discussed further below), and three taps which housed the temperature probes. Besides such ports, there were four passages through the copper block which ran parallel to the surface, allowing the circulation of water to control the block temperature. The constant-temperature water was provided by a Cole Parmer Polystat Constant Temperature Circulator model 12103.

The pressure in the test cell was dynamically controlled by a pneumatic system consisting of a Tescom ER-3000 valve controller and a Tescom 44-4790-24-052 back pressure regulator. This controller-regulator tandem controlled the test cell pressure by regulating the discharge of vapor out of the test cell, and will be referred to as simply the Electronic Pressure Regulator (EPR). This system used a closed-loop, Proportional-Integral-Derivative (PID) control to maintain the pressure level as set in the LabVIEW program and could hold the pressure to within ± 0.5 kPa of the specified value.

A proportional solenoid valve admitted vapor into the test cell from the vapor generator. The valve had a maximum flow factor of 0.5, which was sufficiently large for this application,

allowing for the rapid increase in the pressure inside the test cell, or, depending on the type of test, making very fine pressure adjustments. The LabVIEW program controlled the inlet valve through a Kepco BOP 20-10M Bipolar Power Supply/Amplifier. The Kepco unit was used to increase the power that can be delivered to the valve, since the available power from the NI module was not sufficient to operate the valve.

The combination of these two valves allowed for a very accurate and responsive pressure control of the test chamber, which was important for the impulsive- and pressure-modulated experiments conducted in this research, as well as for the quasi-steady baseline case. The system could maintain a pressure level to within ± 0.4 kPa, and could raise or lower the cell pressure 3 kPa (the amount typically needed to apply or eliminate the superheat) in generally less than 1 second. Considering the stable temperature control within the copper block which could be achieved with the Cole Parmer water system, a wide range of experimental conditions could be achieved and maintained. The experimental test conditions are discussed below in chapter 3.

The bulk of the fluid handling system (except for the vacuum pump) was completely contained within a ventilation hood with a flow capacity of 100 SCFM, which prevented any potential accumulation of vapor. The exhaust line of the vacuum pump also discharged into the ventilation hood.

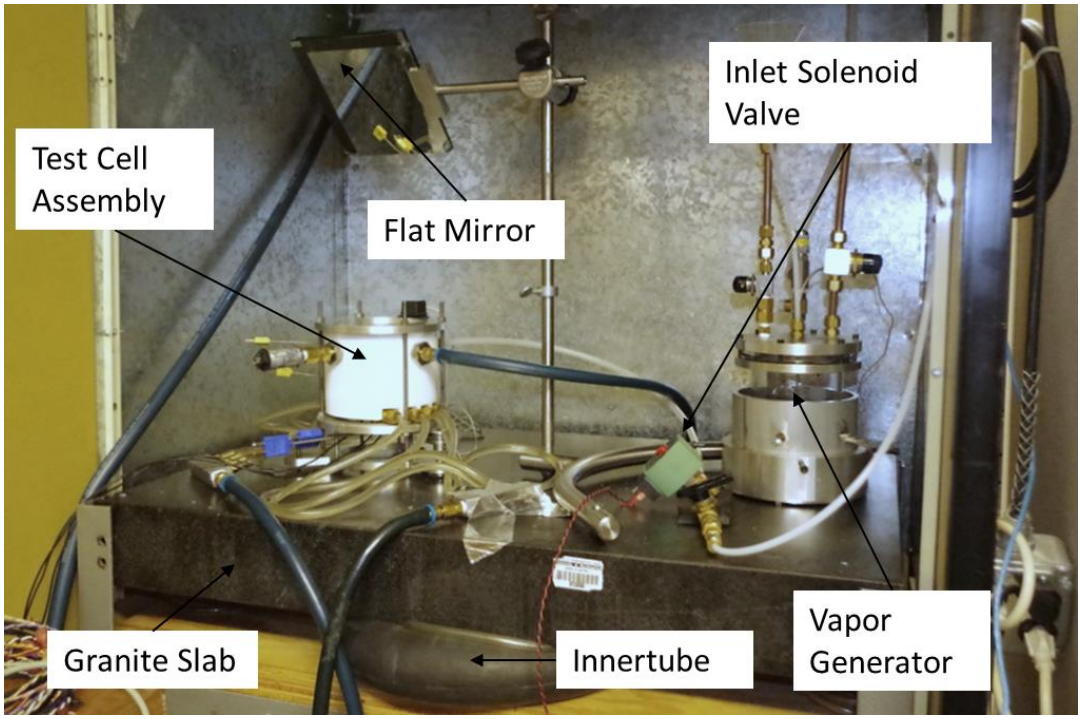

Figure 2.1. Image of the experimental hardware.

Figure 2.2. Vapor generator sub-system (diameter approximately 15 cm (6 inches)).

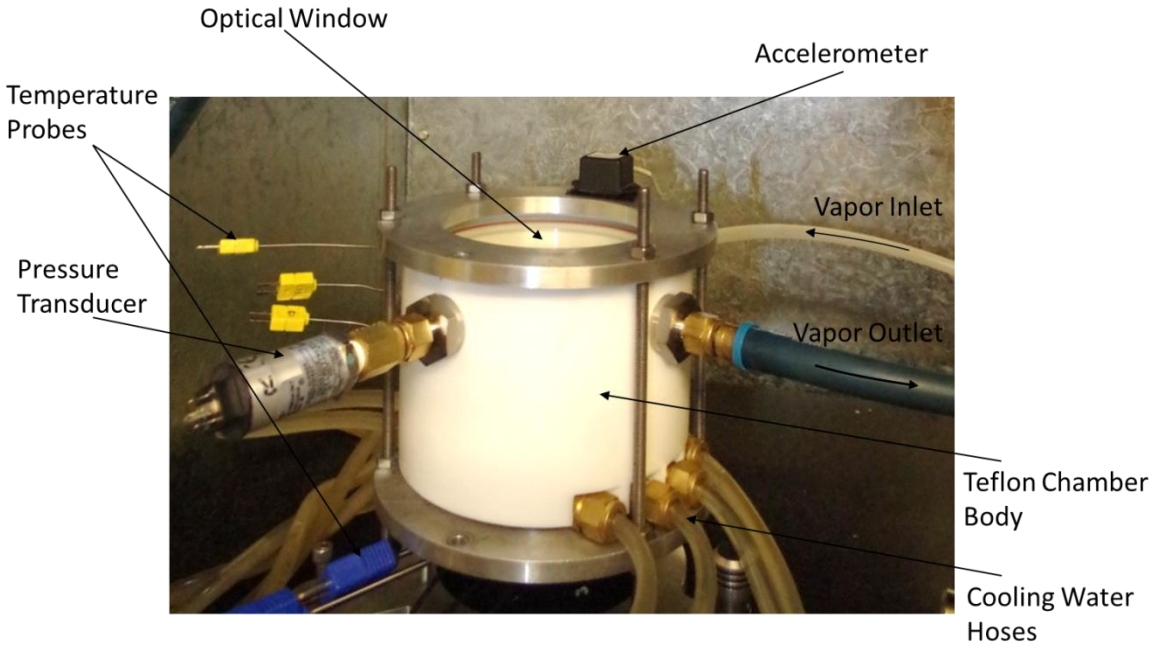

Figure 2.3. Test cell with main components highlighted.

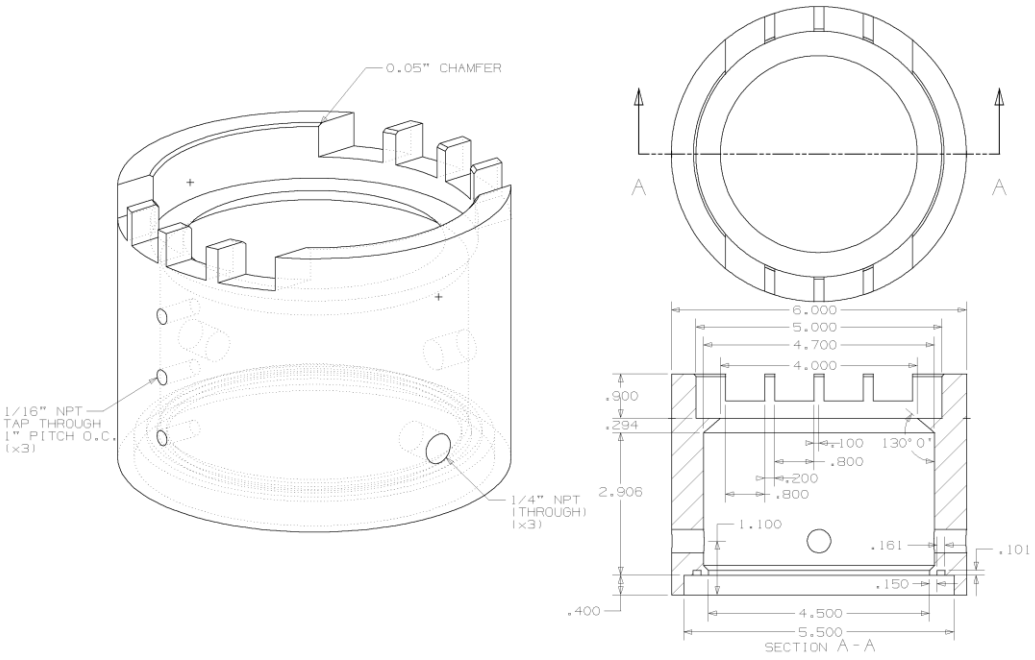

Figure 2.4 CAD representation of test cell configuration.

2.3 Diagnostics

2.3.1 Schlieren imaging

A double-pass schlieren system was used to image the convective structures that evolve during unsteady film evaporation. Two light sources were used for this imaging. The first source used consisted of a Newport/Oriel 75W arc lamp. This source, though extremely stable and bright, was not practical to operate in the reduced-gravity experiments due to its relatively high power consumption and physical size. An alternative light source was developed for the reduced-gravity system, which consisted of a 700 lm output LED, with a Thorlab array of lenses, pinholes and optical cages. This alternate source provided sufficient light, required only a fraction of the operating power of the arc lamp, and had a much smaller physical footprint. This source eventually replaced the arc lamp in lab experiments as well. The remainder of the schlieren system was unaffected by the change in light source. The source light was focused by an f/8, 8-inch (200 mm) diameter parabolic mirror which collimated the incoming light. The light column was then directed into a front surface mirror, reflecting the light onto the evaporating film and copper surface. In this double-pass schlieren configuration the light path, upon reflection from the polished metal surface, passed a second time through the film, as well as the front surface mirror and the parabolic mirror. The beam was then split with a beam-splitter between the light source and the parabolic mirror, and focused onto a knife edge, where approximately half of the light was blocked, giving rise to the classic schlieren effect. The resulting image was then captured and recorded by a Panasonic WV SP-302 camera operating at a standard video rate of 30 Hz. The camera had a 640×480 pixels, translating into an approximate spatial resolution of 0.2 mm per pixel. Before each experimental test, the camera clock was synched with the computer clock. The captured images showed the real time in the frame, so the images could be

correlated with the thickness and heat transfer data. It should be noted that the schlieren images revealed patterns due to surface deflection as well as refraction due to temperature gradients within the film. Therefore, there was a great need to minimize externally-imposed disturbances to the film surface, whether from mechanical excitation or aerodynamic blowing. The system and methods used to sustain an undisturbed film will be discussed in later sections.

2.3.2. Ultrasound Thickness Measurement

The ultrasound system was used to capture the dynamic film thickness at multiple locations. The ultrasound system worked by matching the acoustic echoes of a simulated ultrasound signal, for which all parameters were known (time of flight, film thickness, etc.) to the actual, recorded acoustic-return signal. This system was developed by Kimball and has been extensively discussed in previous publications [[30], [36]]. Therefore, only a brief description and sketch (Fig 2.5 and 2.6) will be presented here.

The short high voltage signal was generated by a Panametrics 5072PR pulse generator. A GE Panametrics MX8 multiplexer split and relayed the signal to each of the Panametrics M116 ultrasound transducers attached to the bottom of the copper plate. Three transducers were used for the majority of the experiments, with some experiments employing only two. It was advantageous to have three transducers since the heat flux phenomena at times was not able to be measured simultaneously by all of them. Also, three transducers yielded a more accurate film leveling than could be measured with the optical bubble level. The element size of the actual transmitter/receiver element was 3 mm in diameter and they operated at a center frequency of 20 MHz. The signal then traveled through the copper substrate and the evaporating film, with the echo at each interface received by the transducers. The waveform of the echo was recorded in the computer via a Panametrics 25MX Plus thickness gage and an Agilent Technologies DSO5054A

high-speed scope. Post-processing was required to extract the film thickness. The raw ultrasound data was processed by a combination of Matlab and FORTRAN codes, which matches a simulated signal based on the expected reflections to the captured ultrasound data. The time-of-flight of the simulated signal is known, and so is the speed of sound through the media (copper plate and liquid). With these inputs, the film thickness is readily calculated. The system had an overall precision of ± 1 um and an accuracy better than 10% [[36]].

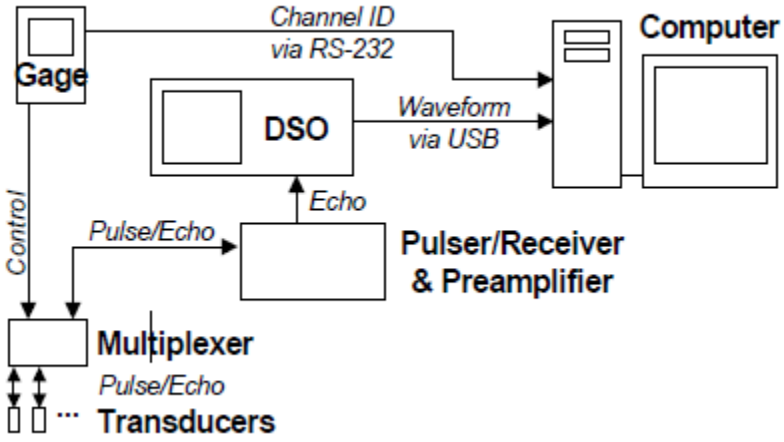

Figure 2.5. Diagram of the ultrasound thickness measuring hardware.

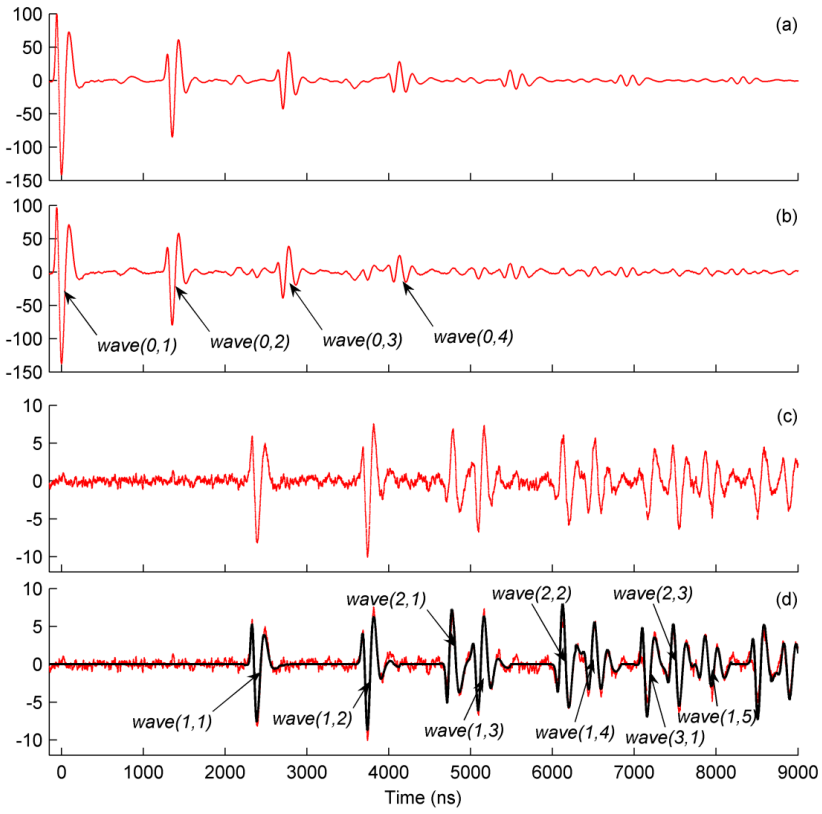

Figure 2.6. Main signals involved in the ultrasound post-processing. Echoes obtained from the copper substrate (a) are subtracted from the echoes with the film present (b), resulting in (c). A code then finds the best match between a simulated signal with a known film thickness (d, black trace) and the base signal (d, red trace).

2.3.3. Thermal Data Acquisition System

Thermal data were gathered through a combination of Omega® pressure transducers, thermocouples (TC) for measuring the vapor as well as the copper block temperatures and a National Instruments hardware and software data acquisition system. The following sections detail the entire thermodynamic data collection system.

2.3.3.1 National Instruments® and Omega® Hardware

The National Instruments data acquisition and control system consisted of three main hardware components: SCXI-1000 chassis and modules, PCI-6220 data acquisition card, and

USB-6351 external acquisition card. The SCXI chassis was capable of supporting four paired module and termination blocks. For the current experiments three such pairs were used. The first pair consisted of an NI SCXI-1102 and SCXI-1303, which conditioned and acquired all the thermocouple data. The second pair consisted of the NI SCXI-1121 and SCXI-1321, and was responsible for the conditioning and acquisition of the pressure data. The third pair, comprised of the NI SCXI 1124 and SCXI-1325, provided the excitation voltage to the pressure transducer and the Tescom pressure regulation system, as well as providing the signal to the Kepco amplifier which controlled the test cell inlet valve. The SCXI chassis was connected to the computer through an NI PCI-6220 digitizer card.

The USB-6351 external data acquisition card is analogous to the PCI-6220, with the main difference being that it is externally powered, and connects to the acquisition computer through a USB port. The USB-6351 was mainly used to carry out two tasks. One was to control on-off equipment, via the digital IO ports and a solid state relay box built in house. The other task was to record the accelerometer data during the mechanical vibrations test. It should be pointed out that the USB-6351 was the only acquisition system used for the aircraft experiments, which will be discussed in later sections.

Two Omega KQSS-18U-6 type K thermocouple probes were used to measure the temperature at the copper block surface. These probes were embedded on the underside of the copper block, and sit 3 mm from the surface. The maximum accuracy that can be achieved with the thermocouple probes was +-0.1 °C. The pressure inside the test chamber was measured with an Omega PX-302 pressure transducer with an estimated accuracy of ± 0.5 kPa. During normal operation no condensation was observed on the inside chamber side wall or on the inside of the optical port. This, combined with the fact that no irregularities in the pressure values measured

by the transducer were observed indicate that the pressure sensor was not affected by the presence of any condensed liquid during the experiments.

2.3.3.2 National Instruments Software (LabVIEW) *VI*

The LabVIEW *VI* (subsequently simply termed the "*VI*") code had several functions. The code recorded the thermodynamic, g-loading data from the aircraft experiments, raw ultrasound data, as well as controlling the test conditions through the above mentioned valves. The *VI* also controlled the push solenoid used in mechanical disturbance tests.

The ultrasound data were collected as the thickness gage relayed the channel change information to the *VI*, which in turn instructed the oscilloscope to record the next ultrasound pulse/echo. After the ultrasound waveform was downloaded from the scopes, the *VI* saved it to a binary data file, along with the timestamp of the recording.

The thermodynamic data was recorded through the SCXI chassis and PCI card. Data acquisition rates were selected to be between 10 and 100 Hz, depending on the speed required for *VI*, which resulted in channel rates between 1000 and 2000 samples per second. The final recorded value for all signals measured with the SCXI was the mean of the samples for each channel, averaged over the length of one iteration loop. The acquisition time stamp for each data point was also collected and saved to an ASCII data file created at the start of each test. Other data included in the ASCII file were the g-loads for each of the three spatial axes, inlet valve aperture states, and solenoid on/off information. Although these last data were not always relevant, they proved to be extremely useful when analyzing test conditions and corroborating the validity of thermodynamic data.

Another essential function of the *VI* was to control the experiment valves, and solenoid. The inlet valve was controlled by supplying a 0-10 V analog output, 0 corresponding to a fully

closed sate and 10 V to fully open. As mentioned above, this output was multiplied by a factor of 2, and its current increased by the Kepco amplifier. The controller could be user-directed (user selects a value between 0 and 100%) or automated as is the case with the pressure modulated cycles. In the latter case, a desired set pressure was pre-selected, which a PID controller embedded in the *VI* converted into a voltage output. The remainder of the Kepco operation was identical in both cases.

The *VI* also controlled the Tescom back-pressure regulator. In this case, the voltage output corresponded to a set point which the Tescom controller used to calculate and supply the necessary voltage. The 0 to 5 V output from the *VI* corresponds to a pressure range from 0 to 15 psi. As is the case with the inlet valve, the user can manually input the desired pressure value to be reached and/or maintained in the test chamber, or the *VI* calculates the voltage output to match a preselected superheat profile. This latter case was used primarily during the pressure modulated tests, which will also be referred to as "modulated tests" for brevity.

Several methods of achieving the desired superheat profiles within the evaporating film were employed. The method that yielded the best results, and the one used for all pressure modulated tests in this investigation, consisted on a having a sub-*VI* routine running a stopwatch for any desired time duration, and automatically restart it the cycle once a specified times limit was reached. The total duration of the stopwatch (ranging between 0.5 and 40 seconds) was set to be the period of the superheating cycles. With the aid of a few simple Boolean commands, it became very computationally light to establish on and off-times, hence resulting in any desired temporal superheat function, without hampering with the rest of the *VI* functionality. With only a few modifications, the same function was used to control the solenoid cycles during the mechanical disturbance tests. A less successful superheat control method consisted on creating

an exact waveform in the *VI* in order to convert the function into a valve command voltage. This method proved to slow down the overall operation of the *VI* and was not extensively employed.

2.4. Vibration Isolation

Preliminary tests revealed that the films were very susceptible to environmental vibrations. These disturbances greatly disrupted the schlieren images and the ultrasound thickness measurements. The source of these vibrations included the ventilation system, vacuum pump, water chiller, and any overall laboratory activity. In order to attenuate this noise, a vibration isolation system was assembled, which consisted of a granite slab approximately 300 lbs. (136 kg) in weight, situated on top of four inner tubes. The high mass and low stiffness of the slab and the inner tubes respectively reduce the natural frequency of the system, therefore greatly reducing the higher frequencies which can severely disrupt the stability of the films. It was reported that vibrations >100 Hz and <10 Hz were greatly reduced or eliminated [[30]].

2.5. General Experimental Procedure

Before starting each experiment, the test chamber was completely degassed for period of up to 24 hours to remove all fluid and vapor and extract any non-condensables, hence ensuring that only the liquid and its own vapor would be present inside the chamber during each experiment. This was significantly important to decreasing the likelihood of nucleation. After degassing was complete, the pressure regulator was set to a value a few kPa above the corresponding vapor pressure for DCM based on the temperature of the copper surface. The inlet valve was then opened, allowing warm vapor to flow into the test cell, which then condensed on the evaporating surface, thus forming the film to be studied in subsequent evaporation experiments.

For quasi-steady evaporating films, once the desired film thickness was reached, the inlet valve was closed, and the set pressure on the Tescom regulator was dropped to a value corresponding to the desired superheat level. The superheat level is calculated based on the difference between the measured temperature of the copper plate surface, and the calculated saturation temperature of DCM for the set chamber pressure. The superheat level was then maintained for the desired length of the test, which ranged from a few minutes for the shorter experiments, ultimately leading to film rupture in the case of longer tests (which typically took several minutes).

The impulsively evaporating films were initiated in exactly the same fashion as the quasi-steady tests. However, the data acquisition procedure was slightly different once the actual experiment commenced. In this case all data acquisition systems were started a few seconds (typically less than 5) prior to applying superheat. Once the superheat was applied, the experiment was allowed to progress until the film reached quasi-steady conditions.

A simple control routine that allowed for the gradual stopping of the evaporation process was established in the LabVIEW *VI*. At the end of each superheat cycle, the inlet valve was initially opened a relative small percentage of the total aperture (typically 40 %) to avoid disturbing the film hydro-dynamically through the introduction of fresh vapor into the test section. The aperture of the valve was then gradually increased to admit sufficient vapor into the test cell to raise the system pressure back to the null condition (meaning that the saturation temperature at the film surface is equal to that of the copper substrate) and effectively stop, or "quench" the evaporation. The command voltage for the valve opening was linked with the same counter used to time the pressure cycles, and the time elapsed from the moment the valve was

opened was multiplied by a small factor (0.3 in most cases). The output voltage to the inlet valve hence followed equation (2.1)

$$V = V_o + k(\Delta t)\,, \qquad \text{Eq. 2.1}$$

where V is the command output to the valve (though it passes and it is amplified by the Kepco first), V_o is the voltage required for the initial aperture, k is the multiplying constant, and Δt is the time elapsed from the beginning of the quenching cycle. Through this gradual way of admitting vapor into the test chamber, with minimal disturbance to the film was achieved.

Chapter 3. Experimental Results

3.1. Validation Experiments

Preliminary experiments were performed to validate the experimental set up by comparison with previous results [[30]] and to provide a baseline for the pressure-modulated film evaporation cases studied in this research. The results obtained from these preliminary experiments involving quasi-steady and transient evaporating films are very similar to those reported previously in terms of heat flux and convective structure evolution.

Comparison experiments for the case of quasi-steady evaporating films were conducted by holding a fixed system pressure via the Tescom EPR which corresponded to the desired superheat level. In this case data were not collected for the short duration of the transient evaporation start-up. Once it was confirmed the film had attained a quasi-steady evaporation condition by observing visually the transition to the quasi-steady convective structure, data acquisition commenced.

The dynamic film thickness was measured using the ultrasound measurement described previously. By knowing the rate of change in film thickness, δ_t, the heat flux at the film surface can be directly calculated using equation 3.1, without the need for any temperature measurement:

$$q'' = \delta_t \rho h_{fg} \,, \qquad \text{Eq. 3.1}$$

where ρ_l is the liquid density, h_{fg} is the latent heat of vaporization, and δ_t is thickness change rate. All of these values were taken to be constant over the small range of experimental conditions considered in the present work. The *Nu* number defined earlier can be reformulated so that it could be calculated from a combination of measured and known quantities, as seen in equation 3.2

$$Nu = \frac{\rho h_{fg} \delta_t \delta}{k \Delta T} = \frac{h\delta}{k}, \qquad \text{Eq. 3.2}$$

where δ is the film thickness, k is the thermal conductivity, ΔT is the superheat level, and h the heat transfer coefficient.

Typical results for the validation experiments are presented in Fig. 3.1 through 3.4. The trend in film thickness was similar to that reported previously [[30]] under quasi-steady conditions, including a nearly linear rate of change in film thickness with time, resulting in an approximately constant heat flux to the surface, with the exception of the very thin films seen at the end of each experiment. Thickness errors are ± 10%, heat flux errors are ±10and temperature errors are ±(0.1C + 0.1kPa×0.17C/kPa), the sum of the wall temperature and the saturation temperature errors. The type of plot seen in Fig 3.1 will be extensively used in the current work for several of the experiments conducted It is important to note that the quoted thickness and heat flux errors assume a flat liquid-vapor interface, which, as it will be explained in later sections, may not always be achieved.

The calculated *Nu*, *Ra* and *Ma* numbers were also consistent with those reported previously, as discussed next. The *Nu* number shown in Fig. 3.2 initially exhibits high variability with a mean value of approximately 3.0, which suggests limited convective activity at this stage in the quasi-steady evaporation process. The variability of the *Nu* number stemmed from a relatively smaller variability on the individuals ultrasound transducers. Recalling that *Nu* number was calculated based on the differential changes in thickness, small thickness fluctuations have a relatively higher impact on the calculated value. The *Nu* number continues to decrease until reaching a value close to unity, and then remains essentially constant for the remainder of the test. This transition in *Nu* number to a constant value near unity corresponds to the disappearance of the convective structure which occurred for films of thickness below approximately 1 mm.

Both the *Ra* and *Ma* numbers decreased monotonically throughout the experiment, due largely to the constant change in film thickness as a result of the evaporation. Both values are considerably higher than the expected critical values.

The above-critical values of the *Ra* number are consistent with the observed buoyancy-driven convection. Regarding thermocapillary convection, however, Kimball [[30]] explained that the traditional definition of the *Ma* number may not be relevant since evaporation leads to a comparatively uniform surface temperature, which would considerably minimize any differential surface tension effects. The test presented here was terminated at a film thickness of approximately 500 microns, at which point nucleate boiling was observed to commence. In the absence of nucleation, it would be expected that both the *Ra* and *Ma* numbers would have continued their reported, downward trend until reaching zero with the film rupture as Kimball reported. The dependences of the *Nu* on the *Ra* number shown in Fig. 3.3 leads to similar trends as those reported by Villaroel [[35]], which described a *Nu* number of approximately unity below the critical *Ra* number, and a sharp rise of *Nu* number above the critical *Ra* number.

The convective behavior seen in this quasi-steady comparison is also similar to those reported previously (as shown in Fig. 3.4). Kimball reported a transition from a polygonal, close-cell structure to long toroidal cells around concentric rings (Images A and B). The toroidal structures started to pinch off (Image C) and closed, forming small cells (Image D). The cells disappeared at a film thickness of approximately 1 mm, leaving a fully quiescent liquid layer (Image E). The wavelength followed a decreasing trend with decreasing thickness through the entire evaporation process. Schlieren images for the QS experiments, at the reported film thickness range, do not show the hexagonal convection pattern which have typically come to be associated with heated films. This association is often erroneous, since the hexagonal behavior

reported by Bénard is only one of many possible convective patterns heated films can exhibit. For example, Sagel [[37]] concluded that the hexagonal pattern is only the stable pattern if the change in kinematic viscosity with respect to temperature is sufficiently large. In the present work, however, the change in viscosity with temperature was only 0.8 % per °C, which is appropriately small [[37]]. In addition, establishing the regular, hexagonal convection pattern can require very long experimental times (on the order of hours [[23]]) and carefully controlled conditions [[27]]. Several studies have reported on the stochastic nature of pattern formation in heated films. For example, Meyer *et al.* reported that the boundary conditions at the side walls have a strong effect on the formation of chaotic vs. non-chaotic patterns in the films [[38]].

Following the QS experiments, comparison experiments were also performed for impulsively-superheated films (ISF) where the focus is on the film behavior immediately following the abrupt initiation of evaporation, before quasi-steady conditions are attained. The evaporating films were established as described above for quasi-steady evaporating films, however, in this case once the film reached the desired thickness after being formed through condensation, the test cell pressure was dropped (through the setting in the Tescom regulator) to a level corresponding to a near-null superheat (<0.1°C) above the measured wall temperature. This non-superheated condition was maintained for at least 30 seconds, allowing any remaining convective behavior to dissipate as confirmed by visual imaging.

For these experiments, temperature, pressure, thickness and video data acquisition were all initiated before the actual experiment commenced. Evaporation was induced by suddenly creating a uniform level of superheating within the film (typically around 2 °C), by rapidly (over a period of approximately 2 seconds) decreasing the chamber pressure, and holding the pressure

at that lower level for the duration of the experiment. This test condition will be referred to as the "impulsively superheated" case throughout this work.

Real-time schlieren video imaging allowed the visual determination of when the experiment reached quasi-steady conditions, at which point, the data acquisition was stopped, and the pressure raised again to the null superheat level. It should be noted that ultrasound sampling rates were increased to 5 to 7 Hz per channel in this case due to the more rapid nature of the phenomena involved in transient evaporation. Still, the sampling rates were higher than the time scales associated with the heat transfer phenomena of impulsively superheated evaporating films. A detailed discussion of the time scales associated with these unsteady evaporation processes is provided in the next section.

Among the most significant results previously obtained, and verified here, is the appearance of two, distinct peaks in the heat flux at the film surface for the case of impulsive superheating. The first heat flux maximum has been reported [[30]] to be essentially related to the initiation of conductive heat transfer through the film (3.5, and 3.6, B); the second, to a marked change in convective pattern and the associated wavelengths (3.5, 3.6, D). The current experiments also matched Kimball's case in the heat flux and convective behavior during the beginning to transition and full transition to QS evaporation (Fig 3.5 and 3.6, E and F respectively) The time elapsed between the superheat application and full transition to QS will be referred to as t_{quasi}, with a nominal value of 30 seconds. The approximate wavelengths of the convective structures observed in the current experiments were determined by scaling versus a known dimension, namely, the diameter of the TC's. Based on this, the wavelength at the onset of convection was approximately 3.5 mm (similar to [[30]]), resulting in an initial wavelength to fluid depth ratio of approximately unity.

Further examination of the aforementioned non-trivial behavior in heat flux and the physical reasons underlying them was one motivation for the current research. In addition to probing the physical phenomena behind the two heat flux peaks in more detail, the heat flux evolution in these impulsively superheated, evaporating films suggests that a net gain in the time averaged heat flux might be achieved. Exploring this possibility was another goal of this effort.

It should be noted that similar values of heat flux were reported for impulsively superheated films with different film thickness above a nominal value of 1 mm. This finding is consistent with the expectation that the transient phenomena start at the film surface, with no impact of heat transfer from the bottom wall [[30]]. This facilitated the current research since it eliminated the need to precisely match film thickness for all cases studied.

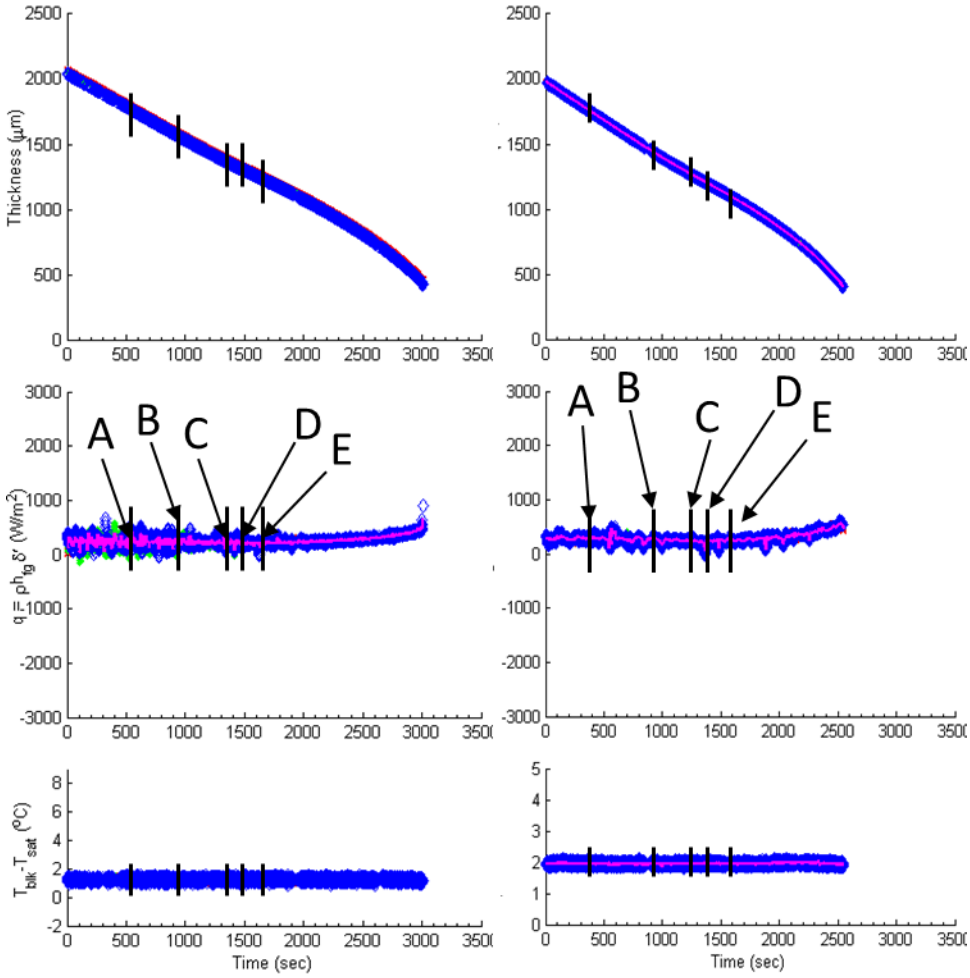

Figure 3.1. Thickness, heat flux and superheat for a DCM film evaporating under QS conditions. Left: (current results), superheat 1.2 °C. Right: (Kimball results), superheat 2 °C. In both cases the initial film thickness was 2.0

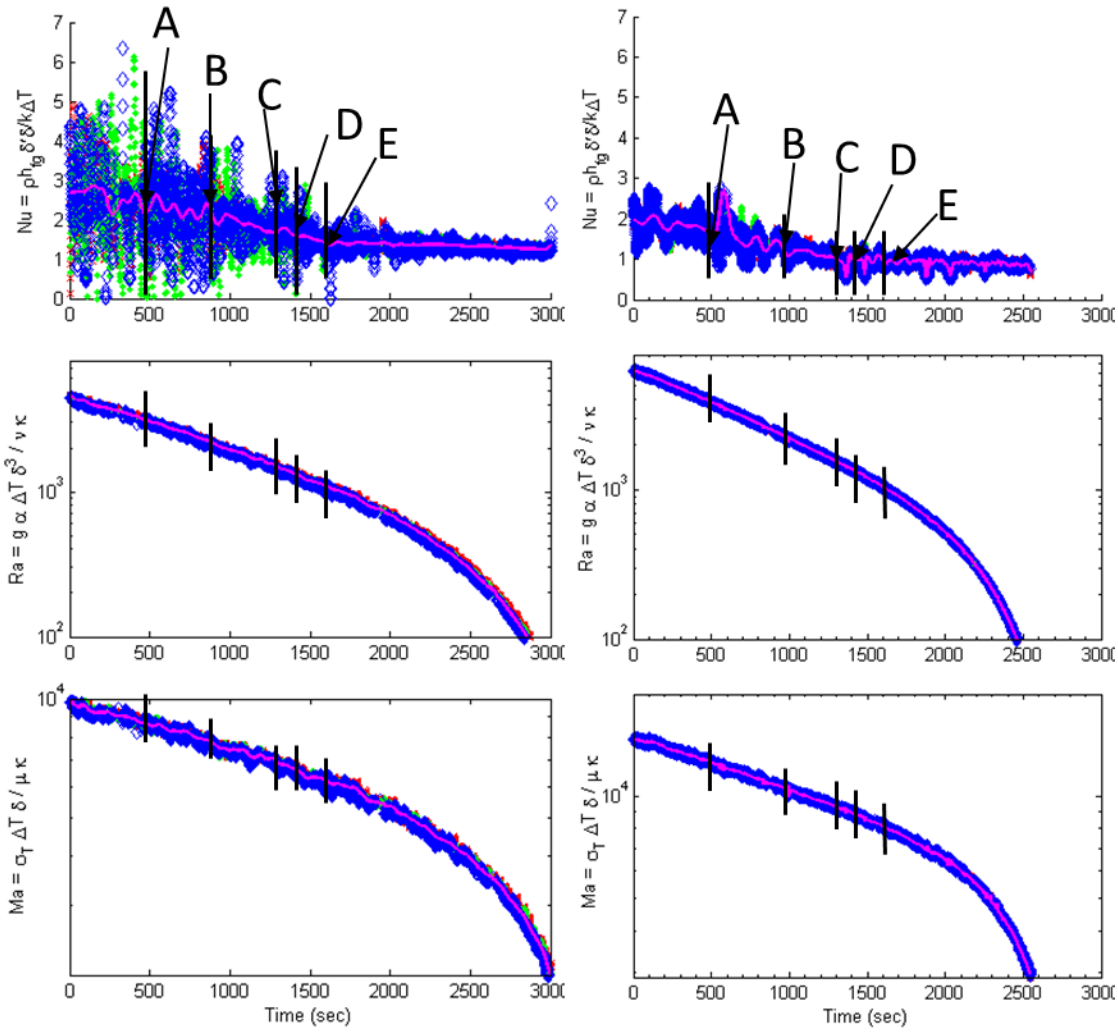

Figure 3.2. Variations in *Nu*, *Ra*, and *Ma* numbers corresponding to the film evaporating reported in Figure 3.1. Left: Current results. Right: Kimball.

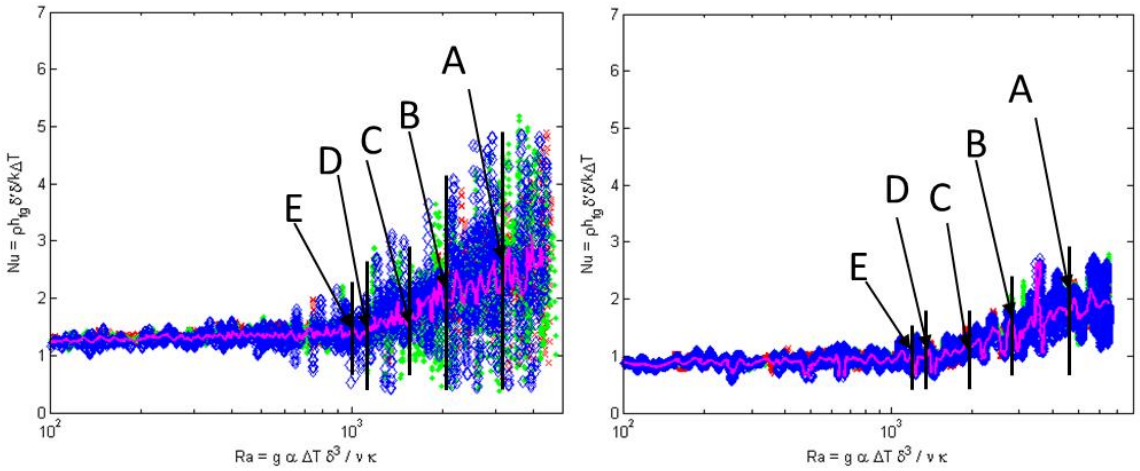

Figure 3.3. Trends in *Nu* vs. *Ra* number for the same quasi-steady evaporating film of Figures 3.1 and 3.2. Left: Current results. Right: Kimball.

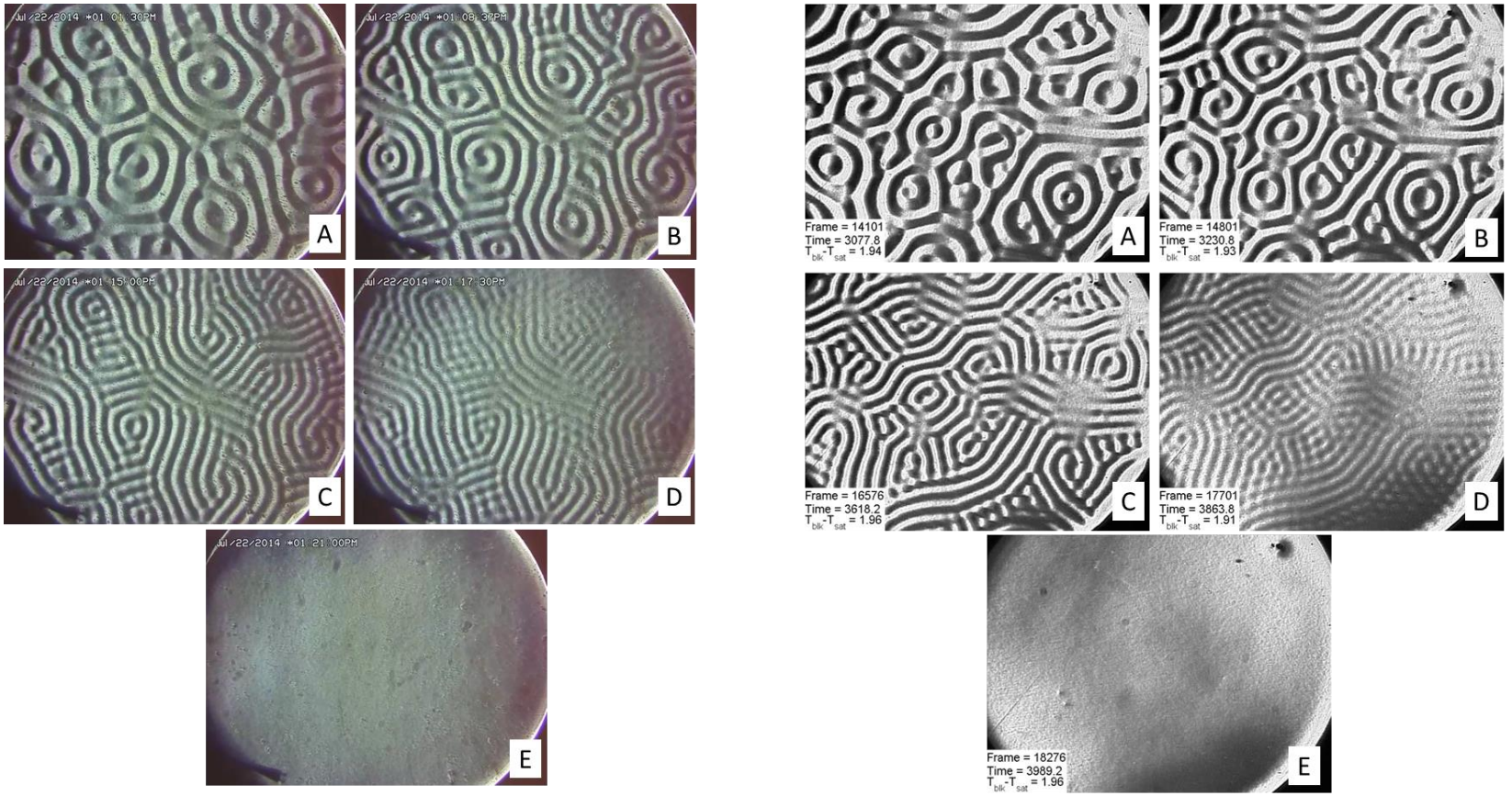

Figure 3.4. Schlieren images of the convective evolution of the QS evaporating film of Figures 3.1-3.3.The images identified in both sets of Figures correspond to the points labelled in Fig. 3.1 - 3.3. Left: Current results. Right: Kimball.

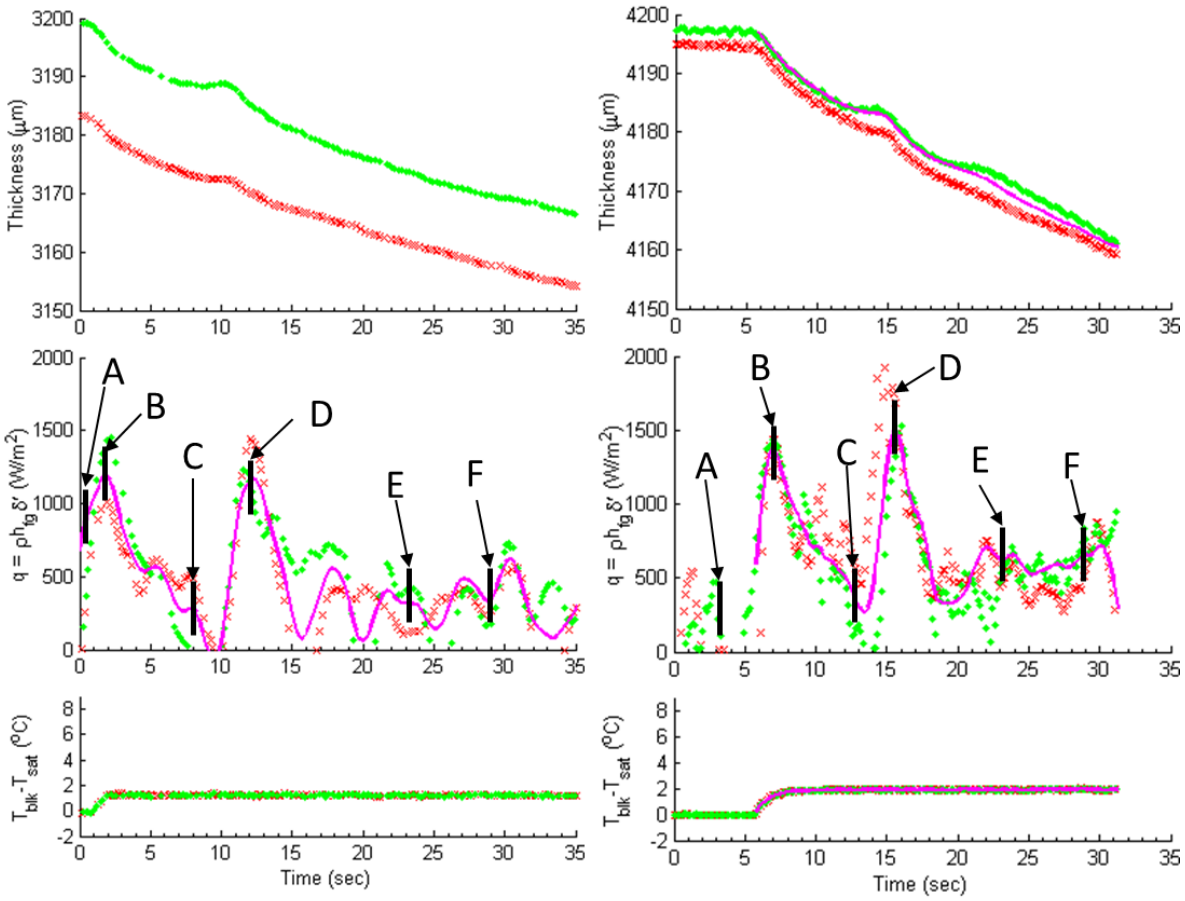

Figure 3.5. Trends in thickness, heat flux and superheat vs. time for an impulsively superheated (transient) evaporating film.Note that though both plots are similar, data collection for the current work (left) commenced 1 second before the application of superheat, where are Kimball's (right) commenced 6 seconds before superheat was initially applied.

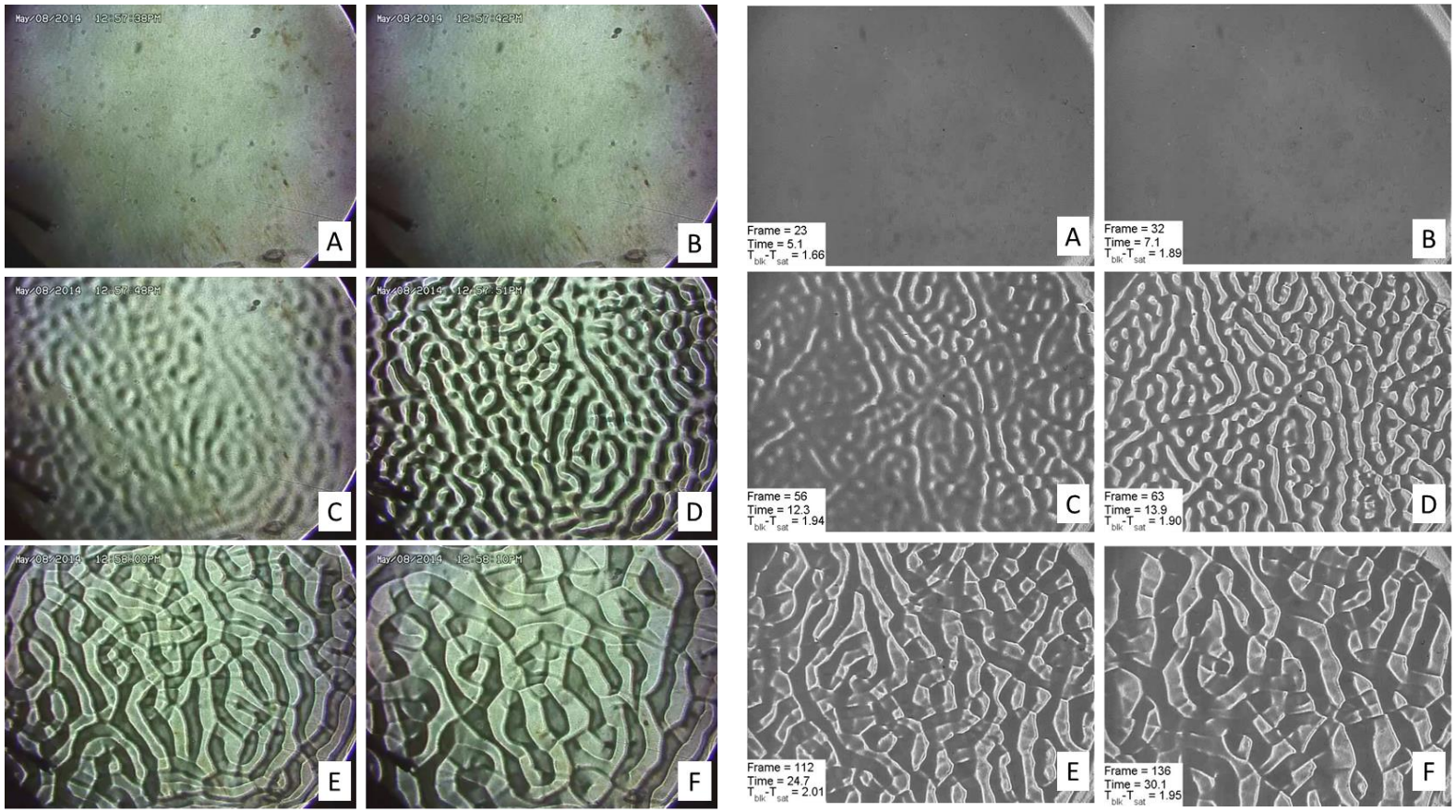

Figure 3.6. Evolution of convective structure in impulsively-superheated films (ISF). Left: Current experiment. Initial film thickness approximately 3.2 mm, subject to 1.2 °C of superheat. Right: Kimball. Initial film thickness approximately 4.2 mm subject to 2 °C of superheat. The images correspond to the points identified in Fig. 3.5

3.2 Heat Flux Trends and Timescales Discussion

The first peak in the heat flux evident in impulsively-superheated, evaporating films typically takes place in the order of one second after the superheat is applied. The time scale associated with this peak is designated t_1 in this work, which was simply the time elapsed between the application of superheat to the observed first peak in the heat flux. This rise in heat flux occurs before any convective activity is observed visually. The absence of convective activity suggests that this rise in heat flux is essentially due to conduction through the uppermost layer film, driven by the temperature difference between the bulk film and the saturation temperature at the film surface. This implies that the fluid very close to the free surface of the film undergoes a change in temperature very quickly, and much faster than the fluid deeper within the film and closer to the bottom surface. Therefore, it is expected the change in temperature in the film starts at the top liquid surface and propagates towards the bottom.

It was considered that the conduction stage lasted, at most, until the apparent onset of convection. This elapsed time represents an upper bound since it is possible that some convective activity was taking place before being apparent in the schlieren images. The onset of convection typically occurred 8 seconds after the application of superheat (this time, normalized by the conduction time, is $t/t_1 = 8$, and was approximately constant for all cases. It was noted by Kimball [[30]] that this apparent onset of convective activity was not the point of the observed second rise in heat flux, which typically did not occur until approximately 3 seconds after the apparent onset of convection, although this time was reported to be as high as 6 seconds, and as low as 1 second. Therefore, the time of the second rise in the heat flux was generally established to occur 11 seconds after the application of superheat, and has been designated t_2 in this work. This peak is attributed to convective effects, more specifically to a measurable sudden change in

the mean disturbance wavelength, which was consistent with present observation. The values of t_1 and t_2 will be widely used in this report as time scaling factors to compare the establishment and maturity level of conductive and convective effects, respectively. Note that both values are the time scales observed in the case of impulsively superheated films only, as in the case discussed in section 3.1.

In order to help model the heat transfer and evolution of the temperature profile within the film during the first seconds of during transient evaporation, and in particular, the transition to the convection-dominated regime, a simple conduction model was developed based on the 1-d unsteady heat transfer equation. It is possible to consider only heat transfer within the film since, as Kimball [[30]] noted, the bottom wall has essentially no impact on the transient evaporation process in these impulsively superheated films. In this case the primary source of heat for the vaporization is the sensible heat within the film. Kimball also determined that the heat transfer between the vapor and the liquid surface due to both conductive and convective effects is relatively small compared to the heat transfer at the film surface.

The evolution of the convective structures observed for the case of impulsively-superheated films suggests that the only a portion of the film depth is undergoing convection at the onset of convective activity. This "engaged" depth changes as evaporation progresses, until engaging the entire film profile. This vertical convective engagement will be referred to in this work as penetration depth. The penetration depth has been estimated previously by comparing the observed wavelengths of the structures between impulsively superheated and QS experiments, then using that information to infer the depth of the film engaged by the convective structures [[30]]. Kimball established that the critical *Ra* number at the onset of convection,

based on the estimated penetration depth, rather than film thickness, had a mean value of 2200, for *Fo* numbers below 0.1 (Fig 3.7).

Adapting the results to the case of a DCM film, subject to a superheat of 1.5 degrees, solving for the length scale in terms of the *Ra* number gives an estimated penetration depth of 1.51 mm for an elapsed time of 8 seconds, (t/t_1 = 8). The *Fo* numbers based on total film depth at the apparent onset of convection for some of the experiments conducted in this work were higher than 0.1, and as large as 0.18. However, this did not impact the estimated penetration depth appreciably since previously results [[30]] suggest that for this range of *Fo* numbers a penetration depth can be estimated, that suggests a *Ra* numbers are approximately 2000, which is consistent with the onset of natural convection. It should be noted that despite the relative low values of *Fo* numbers, there has a been an increased thermal profile evolution through the film, since the *Fo* numbers based on conduction only do not fully account for the convective phenomena. (Fig 3.7).

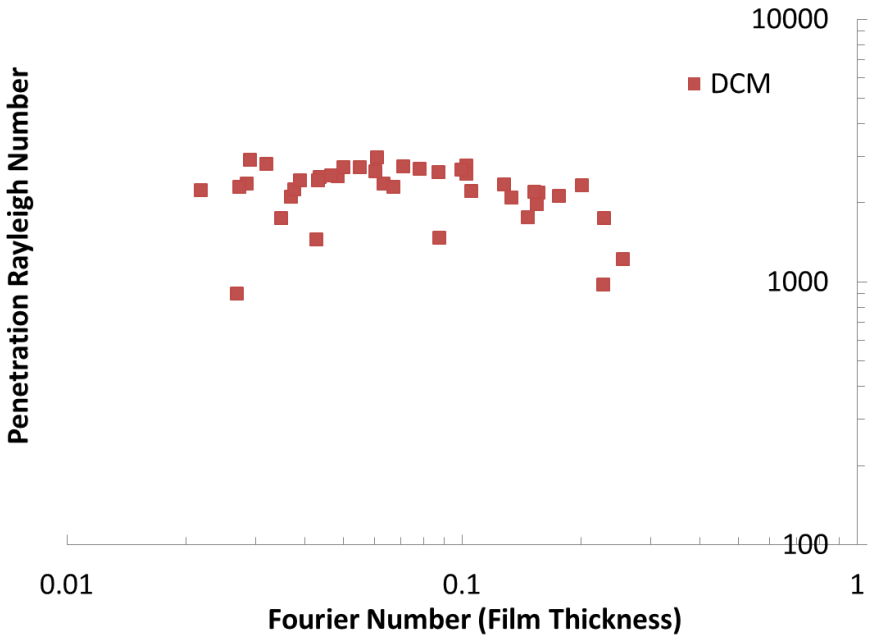

Figure 3.7. Variation in the *Ra* number based on the estimated convective stucture penetration depth with elapsed time, as characterized by the *Fo* number based on total film thickness.The penetration *Ra* number is approxiamtely constant for *Fo* numbers between 0.02 and 0.2.

Another relevant time scale for relevant to the evolution of convection within the evaporating film is the rotational period (t_{rot}) of a convective eddy with a length scale equal to the estimated penetration depth. This rotational period may be used as a time scale to indicate the level of development of the convective structure. Well-developed convective structures could be expected to result in a locally linear temperature profile within the film, consistent with the linear temperature profile that characterizes quasi-steady films. A characteristic velocity of the convective motion within the film was formulated by Ostrach [[11]] which, for Grashof numbers >1 is

$$U_{\text{conv}} = \sqrt{Gr}\left(\frac{\nu}{d}\right) = \sqrt{\beta g \Delta T d}\,, \qquad \text{Eq. 3.3}$$

where *Gr* is the Grashof number, defined as

$$Gr = \frac{g\beta\Delta T d^3}{\nu^2} \quad , \qquad \text{Eq. 3.4}$$

where ν the kinematic viscosity, β is the volumetric expansion coefficient, ΔT is the superheat, and *d* the eddy diameter (in this case, the estimated penetration depth). Recalling that the *Gr* number represents the ratio between buoyant and viscous forces, a *Gr* number considerably greater than unity (in the order of 4000) was obtained for the present case. This also indicates that buoyancy is the dominant driving force. *Ra* numbers associated with convection are sufficiently above the critical value (or near it), which is also consistent with a dominant buoyancy effect in these unsteady films. Calculating the characteristic velocity for a DCM film subject to 1.5 degrees of superheat (the case considered previously), and a nominal penetration depth (eddy size) of 1.5 mm gives a value of U_{conv} = 5.5 mm/s. That results in an estimated eddy-overturning frequency of 3.7 Hz. This corresponds to t_{rot} = 0.27 seconds (1/3.7 Hz), a time considerably shorter than the characteristic time for the both the conduction-only phase (t_1), and the convective-transition phase (t_2). The Reynolds number associated with this convective velocity is approximately 23. Few studies have been conducted on the flow field and overturning velocity of within a convecting film. One of those studies was done by Dubois *et al.* [[41]], in which the authors employed a laser anemometry technique to obtain the vertical and horizontal velocity components of a convecting roll in silicon oil heated from below. The largest velocity reported by the authors was 400 μm/s, which is one order of magnitude lower than the velocity obtained in the present work. However, that work did not allow for a free fluid surface, and it was done under quasi-steady conditions. These two differences likely contributed to the difference in the reported velocity values.

Another fluid velocity study was conducted by Garon and Goldstein [[39]]. The authors investigated pools of heated water heated from below, and their velocity findings are of the same order of magnitude than the ones calculated in the present work. However, more studies would still have to be conducted to precisely and definitively determine the fluid velocity, in particular under evaporating and transient conditions.

The characteristic velocity given in Eq. 3.3 is consistent with that obtained by normalization of Navier-Stokes equation (3.5) by comparing the order of magnitudes of the buoyant and convective terms, assuming that both the pressure gradient along the vertical direction cancels the effect of the body force, and the viscous effects are negligible. Therefore, the buoyancy term was the driving force for the convective acceleration. Thermocapillary effects at the film surface were neglected for this calculation.

$$\underbrace{u\frac{\partial u}{\partial y}}_{\text{Inertial Term}} = \underbrace{-\frac{1}{\rho}\frac{\partial P}{\partial y}}_{\text{Pressure Gradient}} + \underbrace{\nu\frac{\partial^2 u}{\partial y^2}}_{\text{Viscosity}} + \underbrace{g(1+\beta\Delta T)}_{\text{Body Force}}. \qquad \text{Eq. 3.5}$$

3.3 Transient Evaporating Films with Modulated Superheat Cycles

Subsequent to the examination of the baseline case where film evaporation and superheating was impulsively initiated, experiments were conducted where the superheat level was cyclically varied by modulating the system pressure. These pressure-modulated experiments were designed with the two main goals. The first was to further understand the phenomena involved in transient film evaporation. The second was to investigate the possibility of increasing the time-averaged rate of heat rejection by exploiting the maxima in heat transfer observed in the

case of impulsive evaporation mentioned in previous sections. The main parameters to consider for the modulated-superheat experiments are the on-time (t_{on}), which refers to the length of time the superheat is actually applied to the film, and the off-time (t_{off}), the time duration for which the film superheat was eliminated and the evaporation effectively stopped. Pressure-modulated cycle times comparable to both the conduction-only time, t_1, and the convection-transition time, t_2, were considered as discussed below.

Two main types of experiments were conducted in this portion of the investigation. The first experiments conducted were considered "slow," meaning that the time scales associated with t_{on} were comparable with the expected convective-transition time, t_2. Experiments with these on-time scales were conducted for both $t_{off}/t_2 \approx 1$ and $t_{off}/t_2 < 1$ were conducted. In all cases discussed here the transitions in system pressure were sufficiently slow to avoid any significant mechanical or hydrodynamic excitation of the evaporation film to allow both visual and ultrasound diagnostics. The second type of tests was considered "fast" with $t_{on} \approx t_{off} \approx t_1$. In that case, the hydrodynamic disturbances on the liquid/vapor interface induced by the rapid admission of vapor into the chamber during the superheat-stopping stage perturbed the film to such an extent that dynamic ultrasound measurements and visual imaging were no longer effective. However, it was still possible to determine the film thickness both prior to and subsequent to each evaporation cycle, thus enabling calculation of the total heat rejected over each cycle.

3.4 Experimental Procedure

The pressure-modulated tests were set up identically to the quasi-steady and impulsively superheated experiments described previously. In practice a quasi-steady test of relatively short duration (approximately < 10 minutes) was always run before starting the modulated tests, in

order to have a baseline for comparison of the evaporation rates under pressure-modulated conditions at a similar film thickness and superheat level. Comparing pressure-modulated results to the quasi-steady test conducted with the same batch of working fluid, and with the same regulator offsets, thus helped to ensure consistency in the data. For example, recalling that superheat was a calculated value based on the difference between the temperature of the vapor based on the measured pressure, and the measured temperature of the copper surface, the actual value of applied superheat was not known until the data was processed. Superheat levels were found to vary from 1.2 to 1.5 °C. It was also common to perform a single cycle, impulsively superheated test, in order to further ensure that the nominal operating conditions were attained.

The test chamber conditions were re-set to a near-zero superheat level, which was maintained until the pressure-modulated experiment was ready to commence. Prior to each test series the settings for continuous cycles were selected within the LabVIEW VI. These settings included t_{on}, t_{off}, and the inlet valve settings (including length and percentage of total valve-open aperture to be executed and PID parameters if such controller was used). At this point, the LabVIEW routine was executed and data collection was initiated, including video if needed. Once data collection was underway the initial superheat was applied. The superheat level was maintained via the Tescom regulator exclusively, with the inlet valve being closed during this time. Once the end of the on-time was reached, the Tescom was automatically set to provide a system pressure resulting in near-zero superheat, and the inlet valve was opened according to the preset inputs, allowing warm vapor from the vapor generator to flow into the test cell, raising the pressure inside the chamber. This sudden stopping of superheating during the cyclical, modulated experiments will be referred to as “quenching” in this discussion. Several variations in inlet-valve settings were employed to accomplish this, as discussed in following sections,

along with the impact those settings had on the experimental results. Once t_{off} was reached, a new on-time sequence (t_{on}) automatically commenced. This cycle sequence continued until stopped by the user, at which point the cell conditions were set again to near-zero superheat level, hence having the film ready for a new test. The number of cycles run ranged from 2 to 30, depending on cycle length, and the phenomena being studied during the given experiment. All other diagnostic systems functioned in much the same way for these tests as well, though some limitations, especially for the ultrasound, were exposed in some of the tests.

3.5 Evaporating Films under Pressure-modulated Conditions (Slow Quenching)

The main focus of these experiments was to further understand the evolution of the convective structures and evaporation rate changes resulting from periodic changes in the system pressure. In order to achieve this goal the vapor-inlet valve was controlled to admit vapor into the test cell sufficiently slowly to avoid mechanically disturbing the films through aerodynamic effects at the fluid-vapor interface. By eliminating the hydrodynamic disturbance during the quenching process, a true instantaneous heat flux measurement could be obtained, as well as schlieren images of the convective structures, throughout the duration of each experiment.

3.5.1. Evaporating Films with Convective On/Off Time Scales

The first type of cycles investigated consisted of on-times $t_{on}/t_2 \approx 1$. In this work, such time scale ratios are also referred to as convective, or "long." The same nomenclature is applied to t_{off} scales. Long off-time durations were chosen as a reasonable starting point to in order to "reset" film conditions back to the initial values at the end of each superheat cycle. In order to consider variations in film behavior between cycles, comparisons will be made between the initial cycle and a subsequent cycle. For most cases tried, transient effects, such as change in

convective structure and heat transfer, became more accentuated as cycles progressed, hence, the last cycle was the obvious choice for comparing to the initial cycle. The cumulative differences in behavior as a function of cycle (not just between first and last) were also studied and will be discussed in later sections.

The time-dependent film thickness, the calculated interfacial heat flux, and the superheat level with time for a modulated superheat experiment with t_{on} = 15 seconds and t_{off} = 10 seconds between superheat cycles are shown in Fig. 3.8. The corresponding, normalized times scales were t_{on}/t_2 = 1.3 and t_{off}/t_2 = 0.9, indicating that the time scales associated with the current experiments were in fact convective. The red, green and blue curves shown in the figure represent data from a different ultrasound transducer. The points labeled in the heat flux plot in Fig. (3.8 b) correspond to the schlieren images shown in Figure 3.9. The initial film thickness was approximately 2.8 mm, and the applied superheat was 1.2 °C. The first superheat cycle behaved as expected for a typical impulsively superheated test described in previous sections, with virtually identical convective behavior, and the double-peak behavior in the heat flux already mentioned (seen here in the interval between approximately 5 and 20 seconds in Fig. 3.8). Image A in Figure 3.9 shows the convective structure at the apparent onset of convection, which is similar to the typical structure reported for impulsively superheated films. The second heat flux spike also occurred at the time of the change in convective structure seen in image B. The film superheating was then stopped after 15 seconds by admitting vapor into the test cell following the method described above. The scatter in the ultrasound results shown in Fig. 3.9 suggests that some minor hydrodynamical disturbances to the film were still induced during each pressure-modulated cycle, however such disturbances did impact the overall quality of the ultrasound data (or the schlieren images, which will be further discussed below). By admitting

the relatively warmer vapor from the vapor generator into the cooler vapor in the chamber brought about by the pressure reduction, some re-condensation on the liquid film was unavoidable. This condensation lies behind the rapid increase in the film thickness during the first few seconds of the quenching portion of each cycle apparent in Figure 3.8. During this phase in the cycle, the warm vapor condenses relatively rapidly on the liquid surface. Still being under saturated conditions, the temperature in the film near the liquid surface would be in close thermal equilibrium with the vapor above it. As this relatively-warmer region of the film grows in thickness the re-condensation slows since the warm liquid layer would add considerably to the heat flux between the surface at which the condensation occurs and the relatively cooler fluid near the solid surface. This would explain why the condensation appears to proceed at two distinctly different rates: the first one being relatively fast and short (comparable with t_1) and a second one much slower, as seen in the thickness data shown in Fig. 3.8.

The combined effect of short t_{off} and the limited amount of vapor admitted into the chamber in this particular experiment to stop the evaporation was evidently insufficient to completely eliminate all convective behavior during the off period. This is evident in images 3.9 C and D, which marked the nominal beginning and the end of the quenching portion of the cycle, respectively. Even after 10 seconds of quenching had lapsed (point D), the schlieren image suggested isolated and relatively weak convective-roll structures. It should be noted that both the re-condensation time and the amount of vapor included in the chamber to stop the evaporation were limited in order to maximize the total heat rejected through the film by minimizing the amount of heat re-input to the film due to any re-condensation.

As the superheat was re-applied, the initial convective pattern (point E) was seen to diverge from the typical impulsively superheated behavior (or the first cycle) at the onset of

convection. Convective structures in this case appeared to exhibit considerably longer wavelengths, and were less sharp. The convective structure during the second heat flux peak (point F) also looked different from the standard impulsively superheated case with similar characteristics to the ones just mentioned. However, after approximately 10 seconds (point G), which would correspond to the beginning of transition to quasi-steady behavior on a typical impulsive superheat experiment, (based on the discussion in Section 3.1.), the convective cells became comparable to those observed in the typical impulsively superheated films discussed in section 3.1 (Fig 3.10). This indicates a decrease in the time it took to reach QS behavior of approximately 10-15 seconds compared to ISF, also suggesting that isothermal conditions during the quenching stage were not reached.

The evolution in film thickness and heat flux for all on cycles for this series of experiments are shown in Fig. 3.11. It can be noted that the first cycle (cycle 1) in fact yielded the highest evaporation rate (as indicated by the decrease in film thickness), of approximately 45% higher than the last cycle tested here. Cycles 2 through 6 were very similar regarding the total amount of liquid evaporated over each cycle, however, their detailed trends in film thickness and heat flux appeared to vary somewhat from cycle to cycle. In particular, there appeared to be an overall decreasing trend of the value of both t_1 and t_2 with the progression of each cycle. This behavior is clearly seen in Figure (3.11 b), where it can be seen that t_1 decreases from cycle-to-cycle until essentially disappearing, and t_2 decreases to a final value of 7 seconds, down from an initial cycle value of 11 seconds.

The lingering convective structures that appear to remain present during the off periods mentioned earlier are most likely due to very weak, but supercritical, *RB* convection. The motions could also be attributed to subcritical instabilities, which several authors have

experimentally reported [[40]]. However, this is not likely the driving phenomenon in the present case, and instead, a more reasonable explanation is the weak supercritical motion due to insufficient quenching of the evaporation, and a small remaining superheat. Regardless, the lingering motion is a clear indication of a film which is not in isothermal conditions.

The current combination of on/off time scales did not lead to a gain in the net heat rejected when compared to a quasi-steady test of the same superheat level (Fig 3.12). The gain seen in the first two progressively decreases, and by the last (6^{th}) cycle, the loss in the net heat rejected was of approximately 12% of the quasi-steady value. A quantitative progression of the changes in evaporation rate vs. the QS case is presented in Table 3.1. For each individual on-cycle, the evaporation rate was considerably faster than that of the QS case under the same superheat level. The fastest and slowest evaporation rates achieved were 269% and 189% of the QS rate respectively. However, due to the re-condensation that inevitably occurred during the quenching stages, the total evaporation rate, meaning, the total film evaporated when referenced to the initial film thickness, led to the net loss previously mentioned (7% decrease by the last cycle).

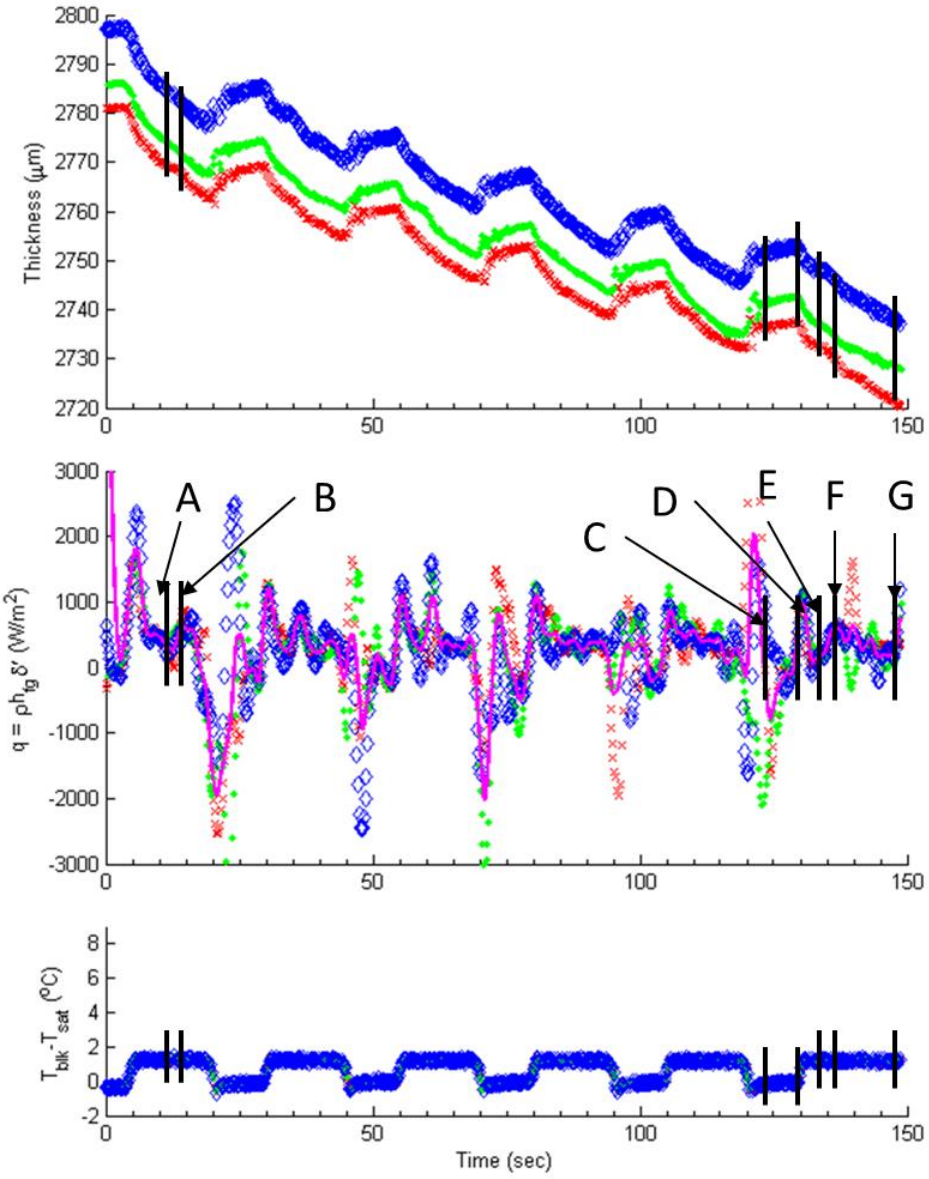

Figure 3.8. Evolution of thickness (top), heat flux (middle) and superheat (bottom) vs. time for a film evaporating under modulated conditions t_{on} = 15 seconds and t_{off} = 10 seconds.

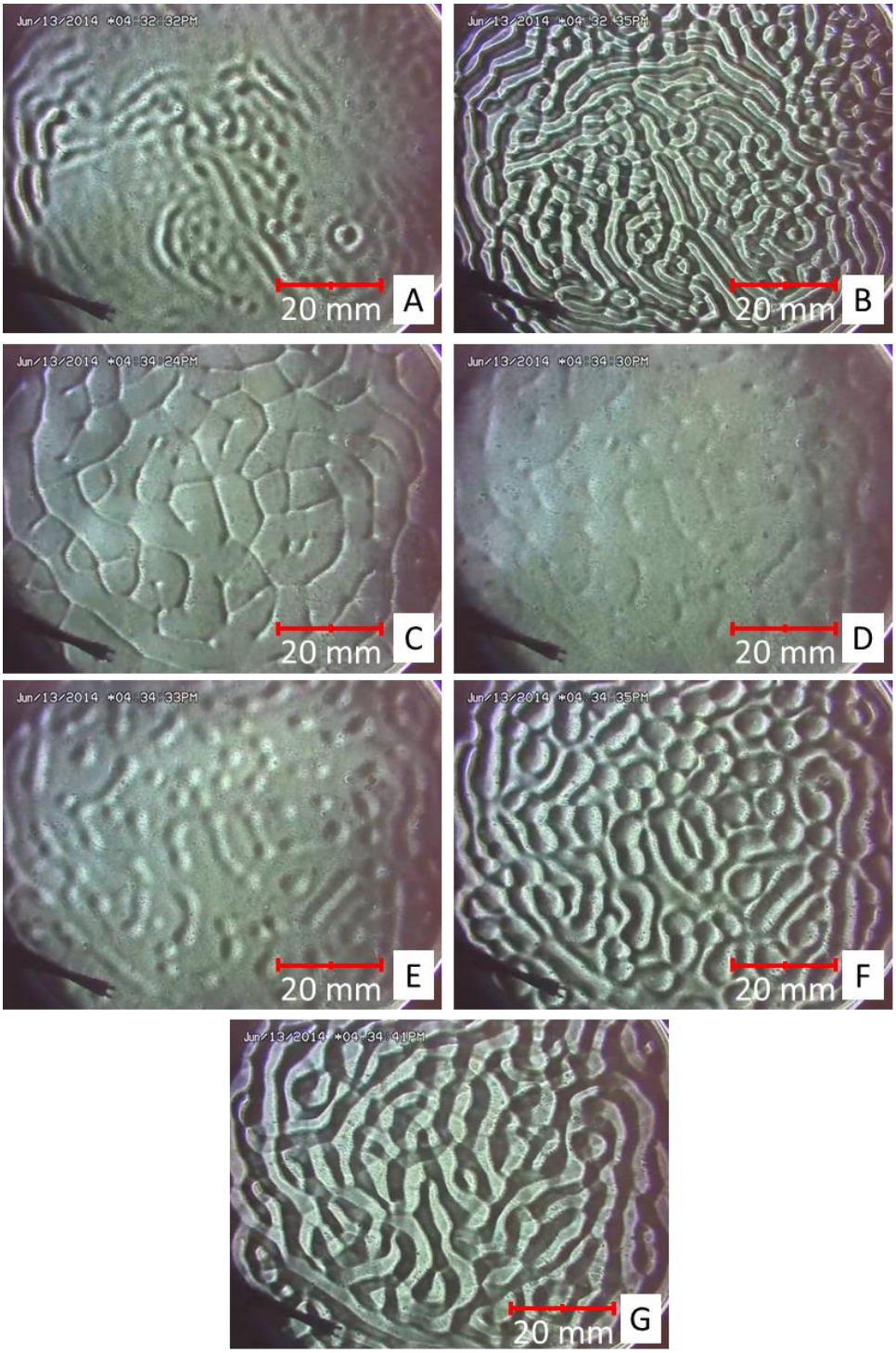

Figure 3.9. Schlieren images of the convective structure evolution of a film evaporating under modulated conditions t_{on} = 15 seconds and t_{off} = 10 seconds. The figure labels correlate to Figure (3.8)

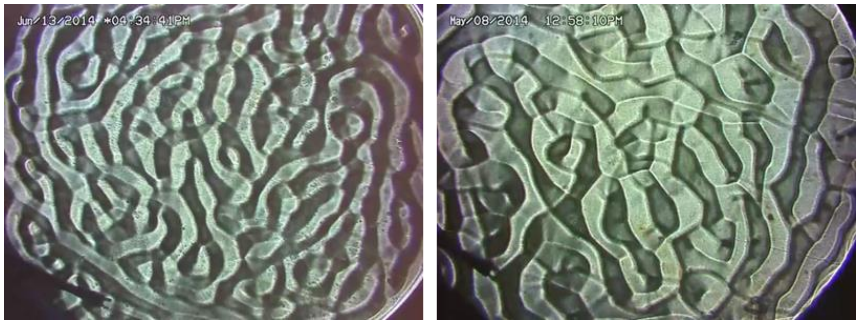

Figure 3.10. Comparison of the end state convective structure for the current experiment (left) with the transition to QS structure for an ISF (right). The shorter wavelength in the current experiment after 15 seconds had elapsed in the last cycle suggests that the quenching stage had some effect in the thermal re-setting of the film.

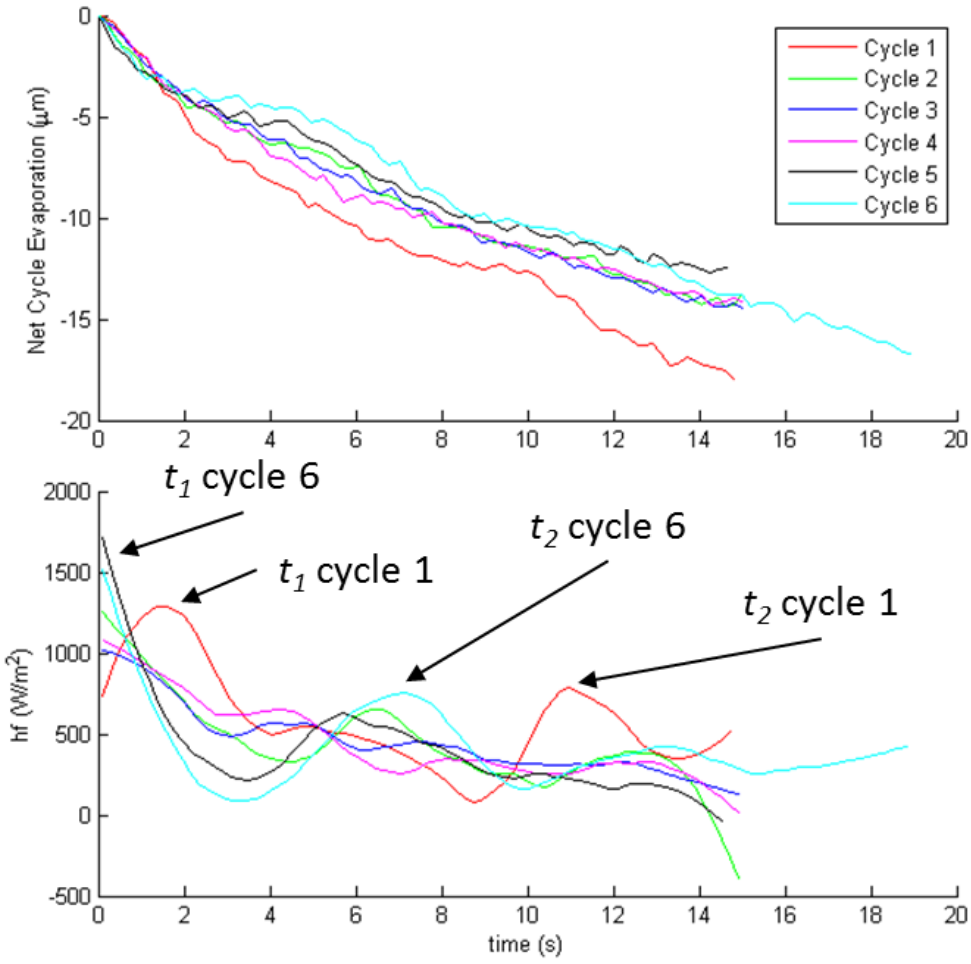

Figure 3.11. Time evolution of thickness (above) and heat flux (below) during the on-stages only, for the film evaporating under pressure modulated conditions described in the present section (t_{on} = 15 seconds and t_{off} = 10 seconds). All seven superheat cycles from the current experiments are shown in the plots.

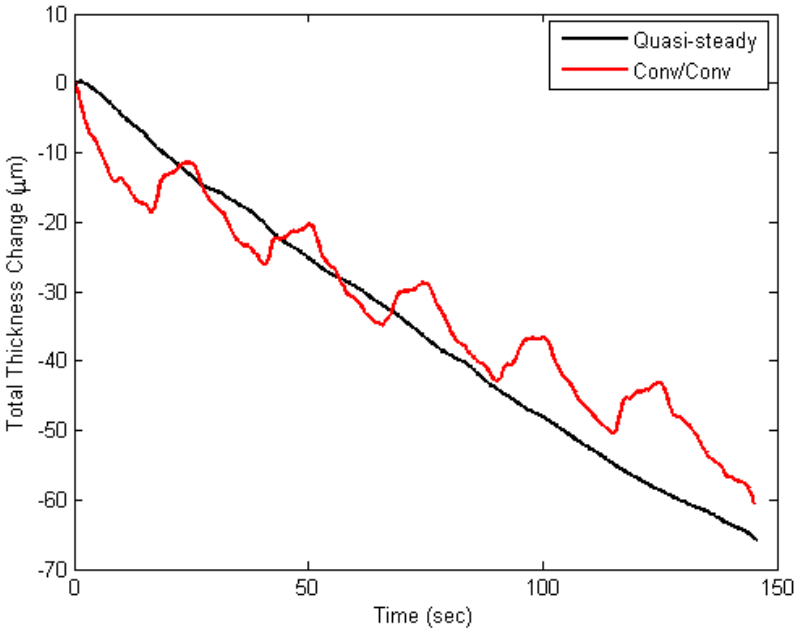

Figure 3.12. Evaporation rate comparison between the pressure-modulated experiment of the current section, and a batch-specific quasi-steady experiment.After 6 cycles, there was a drop in the total heat rejected of approximately 12% of the quasi-steady rate.

Cycle No.	Net Thickness Change (μm)	t_1 (first cycle only) (s)	t_2 (first cycle only) (s)	Cycle Evaporation Rate (μm/sec)	Cycle Evaporation Rate w.r.t QS (%)	Total Evaporation Rate (μm/sec)	Total Change w.r.t QS (%)
1	18.33	1.31	10.68	1.21	269	1.09	141.1
2	26.03			0.92	204	0.64	42.6
3	34.75			0.96	213	0.53	17.3
4	42.94			0.94	209	0.47	4
5	50.44			0.85	189	0.44	-2.7
6	60.6			0.88	196	0.42	-7

Table 3.1. Quantitative progression of evaporation rate and comparison to QS with cycle number for the current experiment.

3.5.2. Cyclical Thermal Model

In order to help explain the variations in convective and heat flux behavior observed during the cyclic experiments, a simple, one-dimensional, non-stationary thermal model was developed taking into consideration the previously-discussed time scales for conduction and

convection. This model is intended to illustrate the changes in thermal conditions from one cycle to the next, and in particular, to highlight the differences between the first pressure-modulated cycle and the subsequent ones. For the experiment just described in section 3.5.1, (small disturbances, slow quenching, and cycle times comparable to the convective time scales, t_2), the model proceeds as follows.

The first stage in the model deals with the peak at t_1 corresponding to the initial, conductive phase. As mentioned before when discussing the thermal conduction consideration earlier, a *Fo* number of unity for this elapsed time indicates that only approximately the top 300 microns in the fluid layer experiences a thermal change, indicating than only fluid from this layer actually undergoes superheating and a temperature increase. A sketch representing this stage of the thermal evolution within the film due to conduction only is shown below in Figure 13.

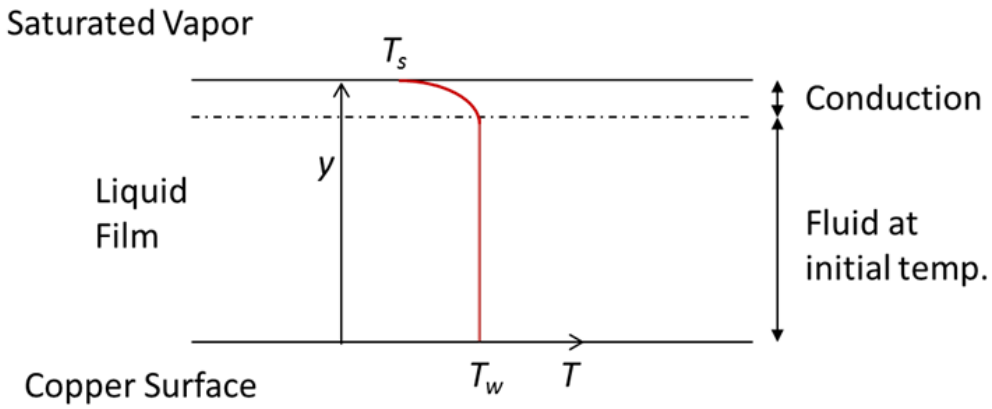

Figure 3.13. Schematic representation of the vertical temperature distribution through a film subject to a superheat from above, during the initial, purely-conductive phase.

This next phase of the model considers the second rise in the heat flux occurs approximately 11 seconds after the application of superheat (which it is by default the t_2 value defined earlier) and 3 seconds after the onset of convection. The expected temperature profile of

through the film is shown in Figure 3.14. This spike always occurs simultaneously with an increase in the wavelength of the convective structure [[30]]. The value obtained previously for the eddy rotation period suggests that approximately 12 eddy rotations occur in the time interval between the onset of convection and t_2, suggesting that the portion of the fluid layer in which the convection takes place has reached a locally quasi steady state condition, where the mean temperature profile can be expected to be linear.

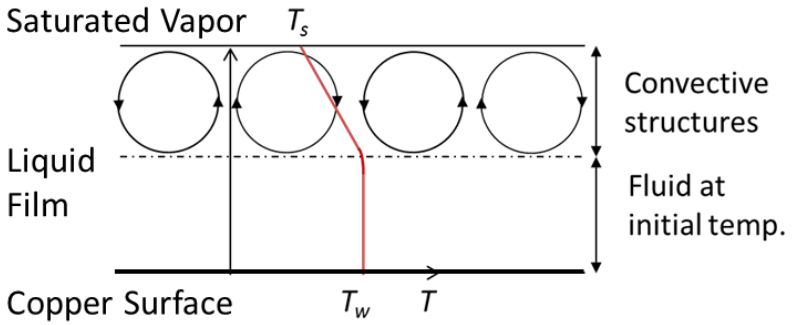

Figure 3.14. Schematic representation of the expected time-averaged temperature distribution and estimated convective cell penetration depth in a film subject to a superheat from above, at the time of t_2.

During the third stage of the model, the re-condensation stage, the incoming warm fluid rapidly condenses on the surface of liquid layer. Neglecting the minimal change in layer thickness associate with this phase (7 to 10 microns typically) that occurs, and initial convective effects, the top layer of the liquid film reaches thermal equilibrium quickly, following a similar time evolution to the conductive evaporation of the first stage of this thermal model. Hence the times scale of the rapid condensation is expected to be similar to t_1. Although there is little change in the film thickness, the heat absorbed during condensation is considerable and can be comparable to that rejected during evaporation, regardless of being constrained to a thin layer at the top of the liquid film. The very bottom layer of the liquid remains at the initial temperature

since neither convective nor conductive effects presumably have had enough time to penetrate the entire film, as indicated in Figure 3.15. The evolution of the mean temperature in this mid-layer, between the film surface and the solid substrate, is however is more complex due to heat transfer to both the lower, warmer layer of fluid as well as the top layer now heated by the re-condensation. The fluid in this layer has a lower temperature than fluid at the other two layers, therefore, it has the highest density for this phase of the process. This presumably results in this layer being at a state of unstable equilibrium with respect to the bottom layer, while being at stable equilibrium with the top layer. Taking for the purposes of modeling all convection to be completely and rapidly stopped during this stage (which is not always the case as will be seen in later sections), the middle layer undergoes heat diffusion by conduction through two layers simultaneously. Assuming that the flow consists of a rotating eddy, with no velocity change along the axial direction, the equations of fluid motion in cylindrical coordinates can be used to represent the fluid motion. The unsteady angular velocity equation shown next,

$$\frac{\partial u_\theta}{\partial t} + \left(u_r \frac{\partial}{\partial r} + \frac{u_\theta}{r}\frac{\partial}{\partial \theta}\right)u_\theta + \frac{u_r u_\theta}{r} = -\frac{1}{\rho r}\frac{\partial p}{\partial \theta} + \nu\left(\nabla^2 u_\theta + \frac{2}{r^2}\frac{\partial u_r}{\partial \theta} - \frac{u_\theta}{r^2}\right) \qquad \text{Eq. 3.6}$$

where u_θ is the angular eddy velocity, u_r is the radial eddy velocity, and r is the radius of the eddy, can be solved for the characteristic time τ it takes an eddy to stop rotating due to viscous forces. The resulting expression is $\tau = r^2/\nu$, and assuming an eddy with r = 1 mm, τ is in order of 3 seconds. This suggests that after the lapse of 3 seconds, when the eddy rotation has essentially stopped, the main phenomena driving the thermal equilibration is diffusion. Due to the low thermal conductivity of DCM, reaching a full isothermal film would take a relatively long time (in the order of minutes). This suggests that the next cycle is typically initiated before a sufficiently long time has elapsed to reach isothermal conditions in the film.

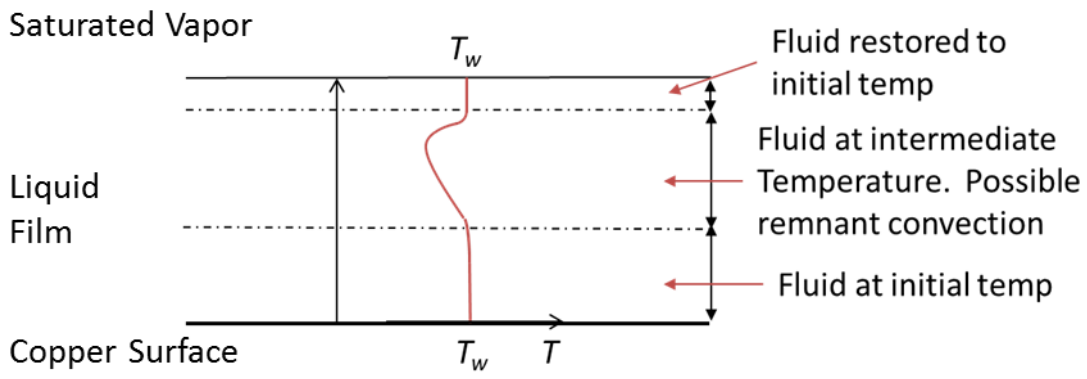

Figure 3.15. Schematic representation of the vertical temperature distribution in a film during the condensing stage.

The final phase of this simple model corresponds to the restarting of evaporation as part of the next cycle. Once evaporation is restarted, the evolution of both the heat flux and the convective structure can be expected to differ from those seen in the first cycle, given the changed thermal environment at the start of the subsequent cycle, as discussed above (Fig. 3.13 and 3.14). After a given number of cycles (the actual number of cycles would depend on t_{on}, t_{off}, the superheat level, etc.) the film would exhibit similar convective structure as that of a quasi-steady evaporating film (Fig. 3.16). This is due to the penetration depth which slowly progresses downwards through the film until eventually involving it completely. It should also be noted that the differences in the transient films temperature profiles between the first cycle and later ones would be expected to result in decreasing trends of both t_1 and t_2, which is in consistent with trends observed experimentally.

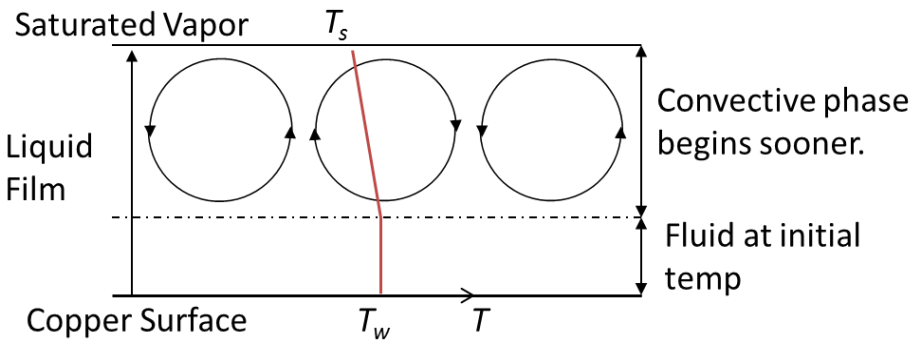

Figure 3.16. Schematic representation of the vertical temperature distribution and estimated convective cell location in a film subject to a superheat from above, starting from some non-equilibrium condition.

3.5.3. Evaporating Films with Convective On-Time and Conductive Off-Time Scales

The evaporating film discussed in section 3.5.1 (convective-convective type) provided insight into the overall behavior of films evaporating under pressure-modulated conditions, while also shedding more light into the transient evaporation phenomena. However, it became apparent that the long re-condensing intervals required to suppress evaporation during each would not lead to a gain in the net heat rejected due, in part, to the significant quantity of heat re-deposited into the film due to the condensation. For this reason, experiments were also conducted with a t_{off}/t_1 value closer to unity, meaning a conductive time scale, as discussed in this section. This on-off combination allowed for the continuation of studies on the structure evolution and heat transfer phenomena, while also possibly enabling a net gain in the total heat rejected over each cycle. The cycle parameters used in this series of experiments were t_{on} = 15 seconds (t_{on}/t_2 = 1.36), which falls in the convective domain, and t_{off} = 2 seconds (t_{off}/t_1 = 2), which corresponds to a conductive off-time interval.

The heat flux and superheat evolution for evaporating films under the aforementioned conditions are shown in Fig. 3.17. A superheat of 1.2 °C was applied at approximately 3.5

seconds after data collection began. Points A and B in Fig. 3.18 show the typical behavior at the onset of convection and the change in convective structure associated with a rise in heat flux, respectively. Up to that point, the test progressed like a typical impulsively superheated experiment in terms of convective and heat flux evolution. The superheating was stopped after 15 seconds had elapsed (t/t_2 = 1.36) by raising the pressure in the test cell as discussed previously. The inlet valve controls were applied following the slow quenching method in order to minimize hydrodynamic disturbances to the film. After a re-condensation interval of 2 seconds, a new superheat cycle was initiated. A total of 7 superheat cycles were applied, which was considered to be sufficiently long to reach the similar convective and heat transfer behavior seen in the last 3 cycles. Point C in Fig. 3.17 and 3.18 corresponds to an apparent minimum in the convective activity. Lingering convective structures are clearly visible, which suggests that the films not yet in full thermal equilibrium at this condition. As superheat was again applied, convective activity started to increase and the re-emerging convective structures seen in Fig. 3.18 (D) appeared to be in similar locations as the lingering structures seen at point Fig. 3.18 (C). In this case, the convection patterns during the beginning of transition to quasi-steady evaporating film behavior Fig. 3.18 (E) looked considerably different from both the typical transient tests and tests with convective t_{off} scales. In this case, long and short wavelength structures coexisted, rather than the relatively-uniform convective wavelength recorded in previous tests. This behavior lasted for approximately 15 sec (Fig. 3.18, F) after the superheat was applied in that particular cycle.

This behavior could be explained, in part, by invoking the model developed in the previous section, as follows. A short condensing stage ($t_{off}/t_1 \approx 1$) would be insufficient to achieve isothermal conditions in the film so that the new superheat cycle would have different

initial conditions from the quiescent state of the impulsively heated films, with the temperature profile through the film being similar to that shown in Figure 3.15.

The time evolution of film evaporation and the associated heat flux, for all portions of the experiment where superheat was applied only, are shown in Figure 3.20. The plot does not include the brief, re-condensation intervals since there was sufficient noise during these stages to obscure the relevant phenomena being studied during the on-cycles. The most notable feature is that the rate of evaporation for cycle 1 was greater than that of any subsequent cycle. The net evaporation decreased progressively with each cycle, with the last cycle exhibiting the slowest evaporation rate of the set, at approximately 50% of the net evaporation of cycle 1. It should also be noted that no cycle after the initial one showed a marked rise in the heat flux associated with a transition in the convective structure. This can also be explained, at least in part, by the thermal-model considerations discussed above. Since convective structures were evidently not completely suppressed during the condensing stage, the middle layer of the film would presumably still exhibit a temperature profile with features somewhat similar to that of a quasi-steady state evaporating film. In this case any further, slight change in the penetration depth, or the nature of the convective structure over the next cycle, would only engage a small, additional amount of liquid from a deeper layer close to the initial temperature, and therefore not increase convective heat transfer significantly. The initial heat flux peak due to conductive phenomena also decreased continuously, both in magnitude and time, as cycles progressed, as suggested by the phenomena just cited.

The entire test can be then approximated as a transient test where each cycle got progressively closer to the quasi-steady condition, since condensing effects were very minimal in terms of duration and thermal effects on the film. This is indicated in Fig. 3.21, which shows the

thickness change evolution for the present modulated test and a quasi-steady test under a constant superheat equal to the one applied during the on-cycles. Although there is an initial gain in the evaporation rate by the end of the first cycle of approximately 139 % over the QS case, this gain decreased considerably to approximately 15% by the end the last (7^{th}) cycle. The quantitative comparison of the data shown in Fig. 3.21 is summarized in Table 3.2. The data show a similar behavior to the Convective/Convective cycle of section 3.5.1. Each individual on-cycle yielded a considerably faster evaporation rate when compared to QS, but the net evaporation rate was diminished due to the re-condensation during quenching. However, since the present experiment consisted of short conductive time-scales quenching periods, a modest net evaporation rate gain was reached.

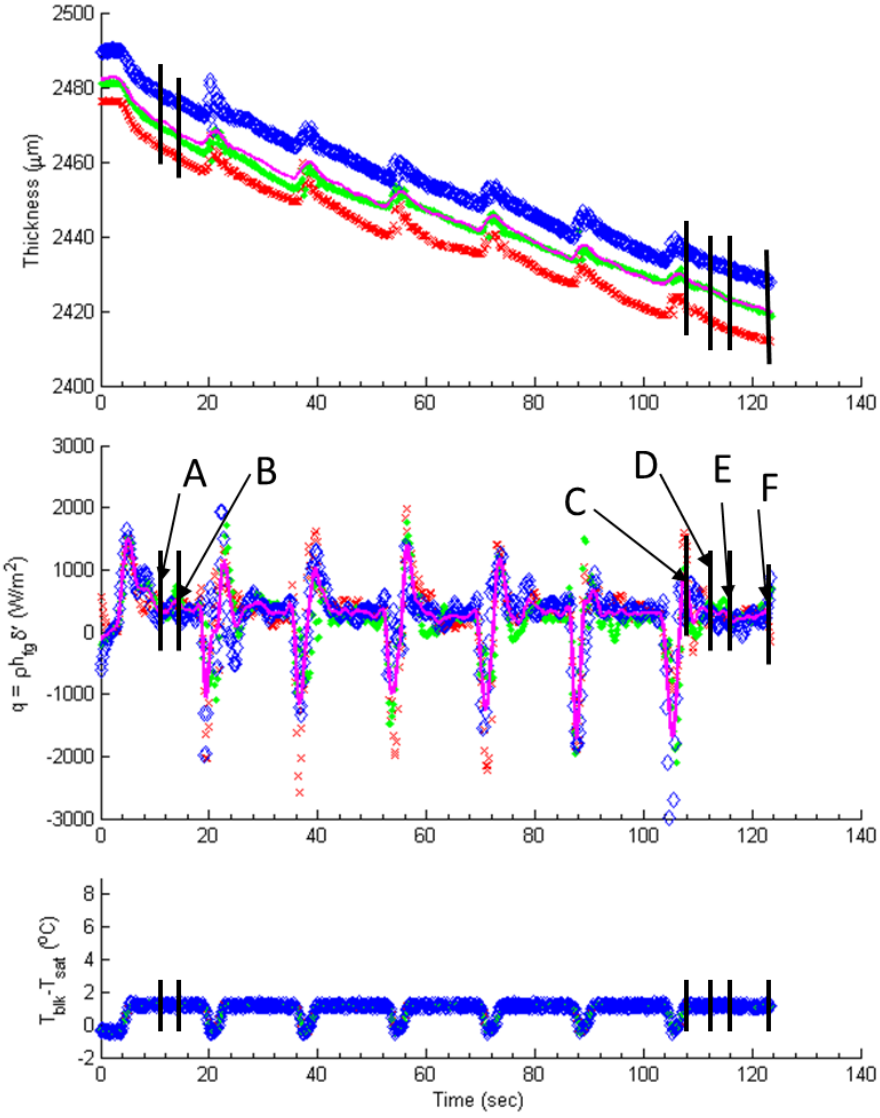

Figure 3.17. Trends in thickness (top), heat flux (middle) and superheat (bottom) vs. time for a film evaporating under modulated conditions (t_{on} = 15 seconds and t_{off} = 2 seconds).

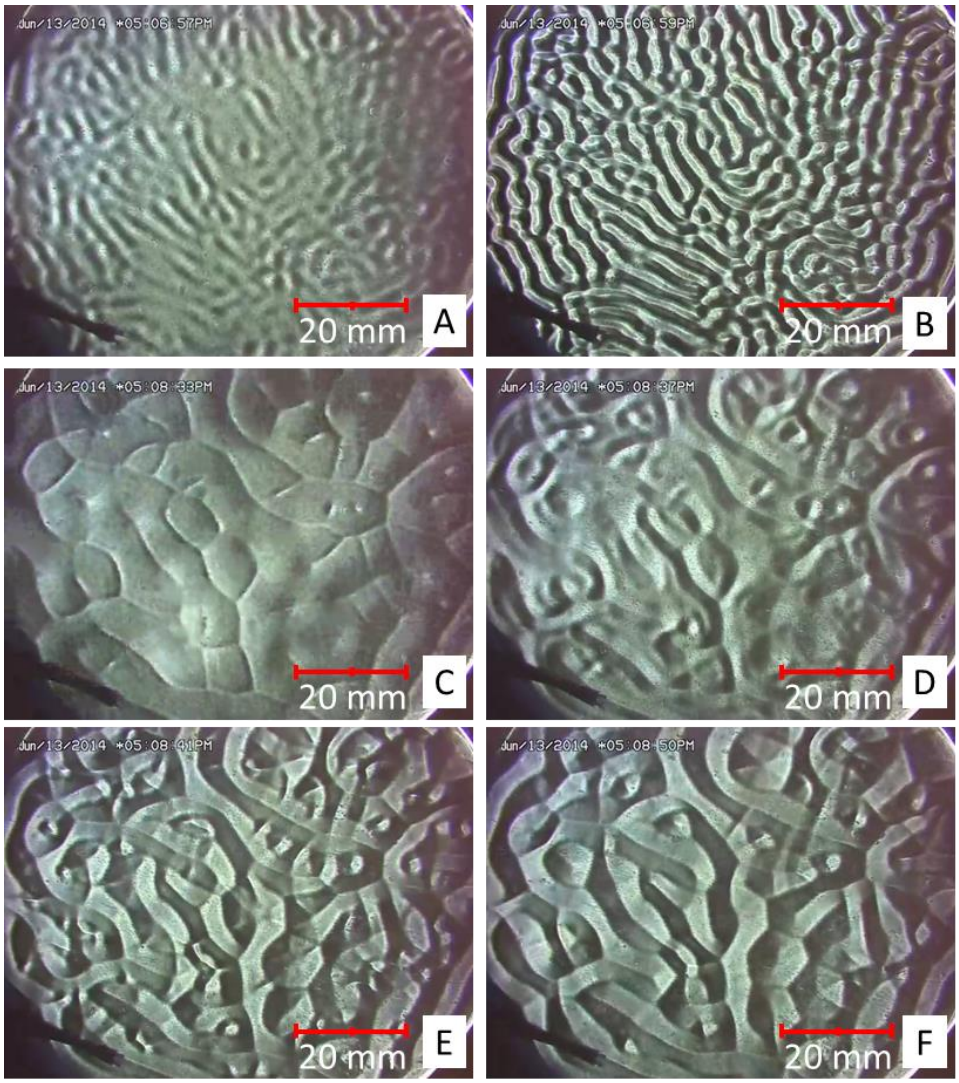

Figure 3.18. Schlieren images of the convective structure evolution of an evaporating film under modulated conditions t_{on} = 15 seconds and t_{off} = 2 seconds. Figure labels correlate to Figure 3.17.

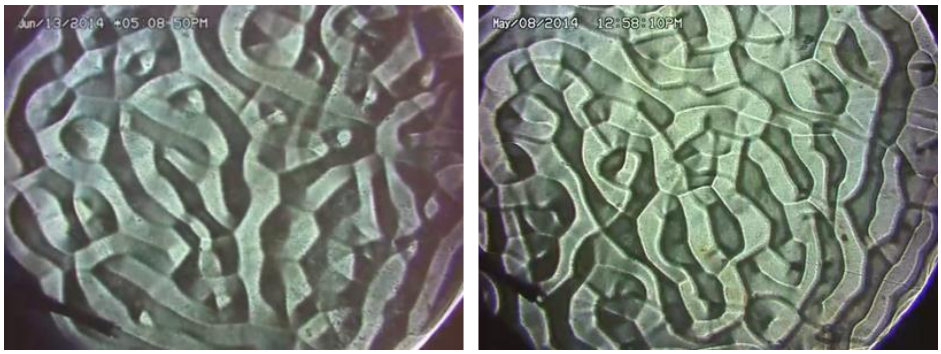

Figure 3.19. Comparison of end state convective structure for the current experiment (left) with the transition to QS structure for an ISF (right).Note that similar long wavelength structure is seen in both, but the current experiment shows several short wavelength cells.

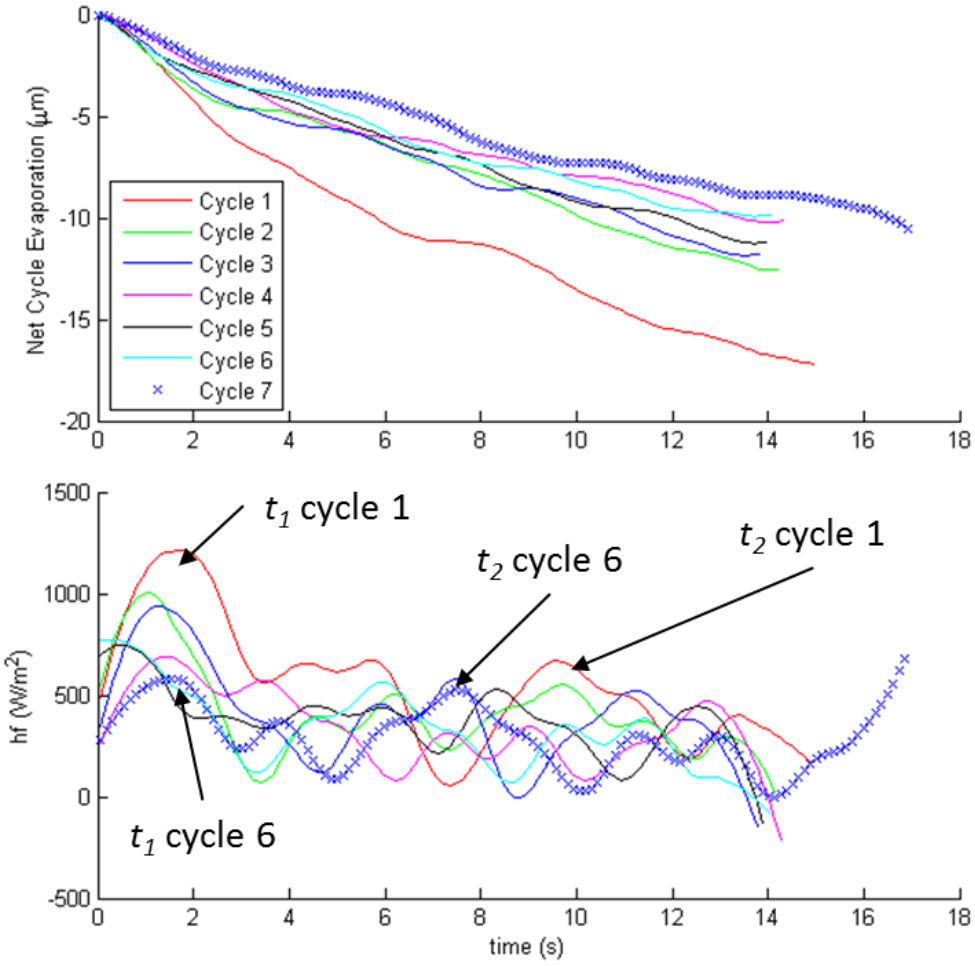

Figure 3.20. Time evolution of thickness (above) and heat flux (below) during on-stages only, for the film evaporating under pressure modulated conditions described in the present section (t_{on} = 15 seconds and t_{off} = 2 seconds).

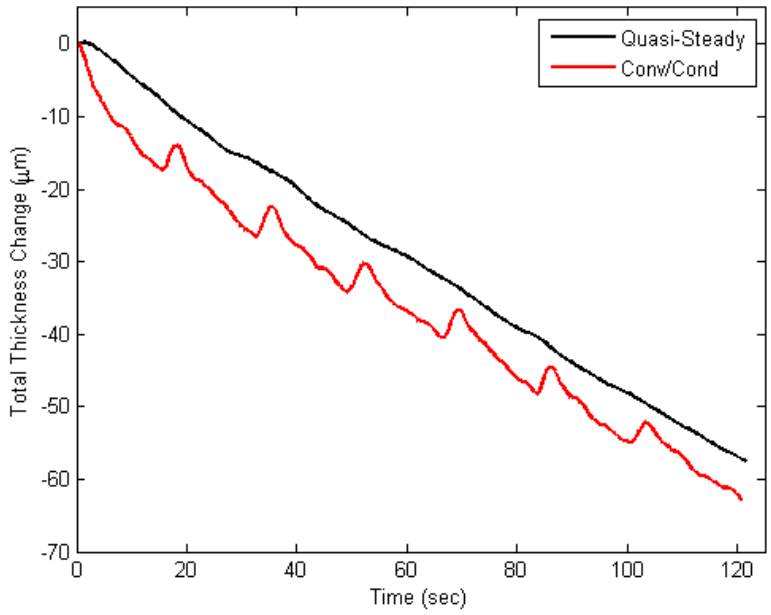

Figure 3.21. Evaporation rate comparison between the pressure-modulated experiment of the current section, and a batch-specific quasi-steady experiment. odest gain in the net heat rejected of approximately 8% of the QS value is observed.

Cycle No.	Net Thickness Change (μm)	t_1 (first cycle only) (s)	t_2 (first cycle only) (s)	Cycle Evaporation Rate (μm/sec)	Cycle Evaporation Rate w.r.t QS (%)	Evaporation Rate from initial thickness (μm/sec)	Change w.r.t QS (%)
1	17.23	0.75	9.933	1.15	256	1.08	139.3
2	26.58			0.88	196	0.81	80.7
3	34.09			0.85	188	0.69	53
4	40.42			0.71	158	0.60	34
5	47.87			0.80	178	0.57	26
6	54.87			0.70	156	0.54	20
7	62.78			0.62	137	0.52	15

Table 3.2. Quantitative progression of evaporation rate and comparison to QS with cycle number for the current experiment.

3.5.4. Evaporating Films with Conductive On/Off-Time Scales

Previous tests helped to provide some understanding of the transient evaporation behavior, as well as the impact of the timescales associated with pressure-modulated cycles on the overall evolution of these experiments. However, even with the cycle off-time decreased from the convective to the conductive range, the experiments led to a relatively small net increase of the heat rejected. In this next series of experiments, t_{on} was also decreased to a conductive time scale in order to exploit the conductive heat flux peak associated with t_1 only, without having to undergo periods of low heat flux level before reaching the heat flux at t_2. These experiments involved 3-second long superheat cycles (t_{on}/t_1 = 3), and quenching stages lasting 2 seconds (t_{off}/t_1= 2), both of which fall within the conductive time scale domain. It should be noted that though this experiment has both t_{on} and t_{off} in the conductive range, the experiment is still limited by the relative slow control method which commanded the rise in pressure during the re-condensing stages.

The thickness, heat flux, and superheat vs. time obtained for the experiments under these conductive-time scale conditions are shown in Fig. 3.22. The initial on-cycle was evidently consistent with the first seconds of the impulsively superheated films experiments, as seen in the figure, where the heat flux plot clearly exhibits the previously discussed spike in heat flux associated with t_1 the conductive time scale. At the end of the second on cycle, no convective structure had yet appeared, (Fig 3.23, A) which is also consistent with impulsive superheat results since the onset of convection typically occurred after approximately 8 seconds from the application of superheat. The onset of convection experienced only a modest to negligible delay (Fig.3.22, point B), occurring 9 seconds after the application of the initial superheat, in spite of

the presence of two evaporation-quenching intervals. Although $t_{on}/_{off}/t_1 \approx 1$ for this film, convective structures still emerged, given sufficient cycles. This would suggest that superheat quenching had a negligible effect, perhaps due to some combination of the short quenching duration, or the slow raise in system pressure, and a temperature profile developed through the film from cycle to cycle. The convective structure shown in Fig. 3.23, C appeared to be similar to the pattern associated with the transition in convective structure responsible for the t_2 heat flux rise. However, there was no measured rise in heat flux for the condition corresponding to point C, suggesting that the conduction effects were dominant and the large heat flux fluctuations were essentially due to the rapid evaporation and conduction cycles. This can be seen in Fig. 3.22 (middle), where the heat flux evolution, both, while evaporating and condensing, is seen to be consistent with that of conduction-only behavior. The structure shown in Fig. 3.23, point D corresponds to the minimum in the convective behavior during the condensing stage, at the beginning of cycle 9 (approximately 51 seconds after data collection began). The convective cells appeared to have remained considerably active, and were only partially diminished. There was evidently a very rapid convective evolution from point D to E, (Fig. 3.23) with significant convective changes observed after the lapse of only two seconds. This, once again, suggests a strong convective activity was still present during the condensing stage in this case. The last on-cycle was allowed to run longer than the 3 seconds of all previous superheat segments to allow the film to settle and obtain accurate measurements of the final film thickness. This also allowed for the convective structure to evolve beyond the early transient stages of 3 seconds of superheat. Convection patterns in points F and G were very similar to the transition to quasi steady behavior reported in the later stages of films undergoing evaporation due to an impulsive superheat. This "rapid" development of the quasi-steady behavior strongly suggests that a temperature profile

developed vertically through the film, as a result of the weak effects (both due to short duration and vapor added) quenching had on the evaporation process. It should be noted again that convective effects are occurring, but are not being observed due to the fast heat flux changes induced by rapid (conductive) evaporation and condensation stages.

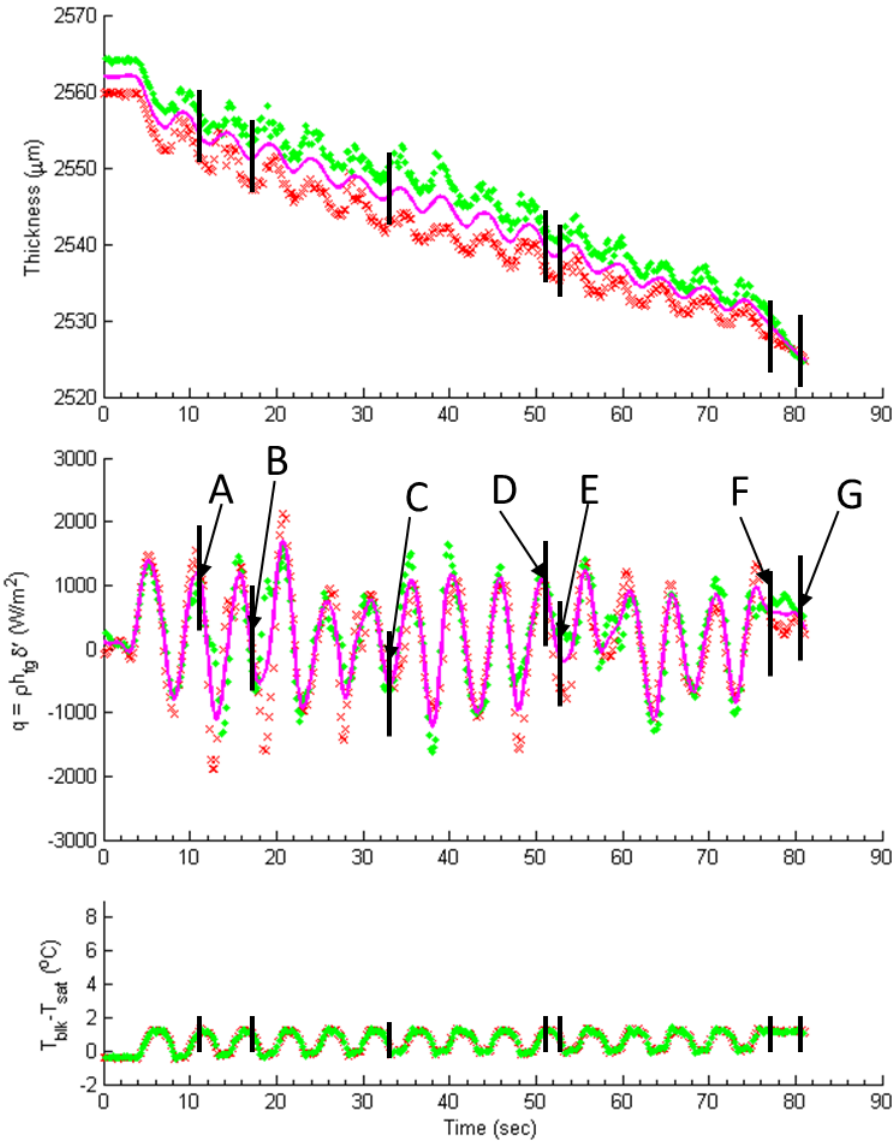

Figure 3.22. Time evolution of thickness (top), heat flux (middle) and superheat (bottom) vs. time for a film evaporating under modulated conditions t_{on} = 3 seconds and t_{off} = 2 seconds.

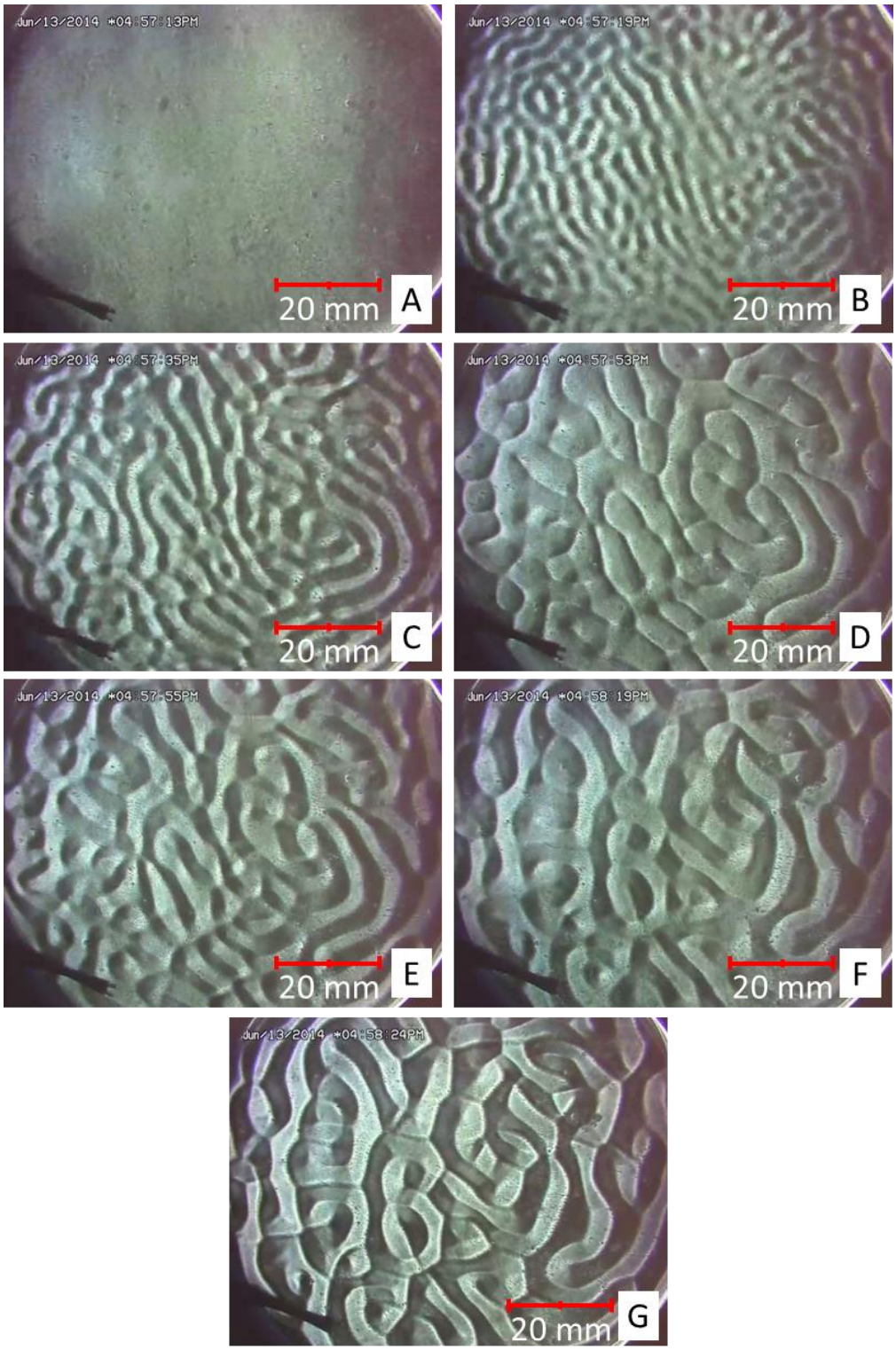

Figure 3.23. Schlieren images of the convective structure evolution of a film evaporating under modulated conditions t_{on} = 15 seconds and t_{off} = 10 seconds. Figure labels correlate to Figure (3.22). Note the high similarity between F and G and the fully developed quasi-steady convection patterns, which strongly suggest a quasi-steady temperature profile developed through the film due to the negligible effect of quenching.

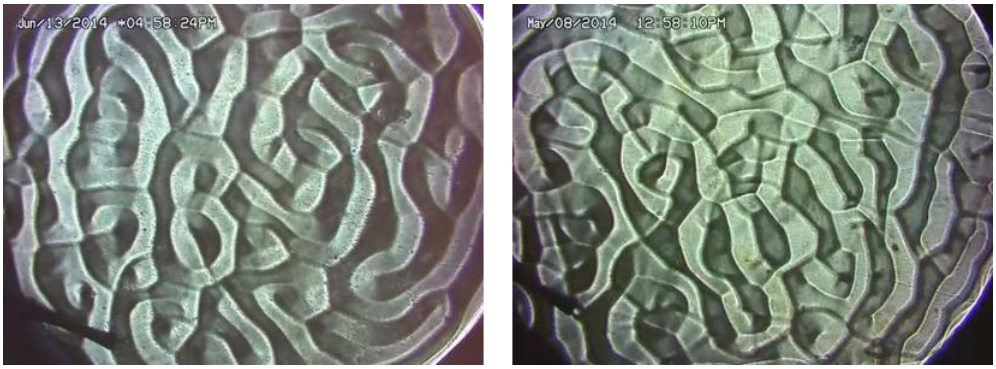

Figure 3.24. Comparison of the end state convective structure for the current experiment (left) with the transition to QS structure for an ISF (right).

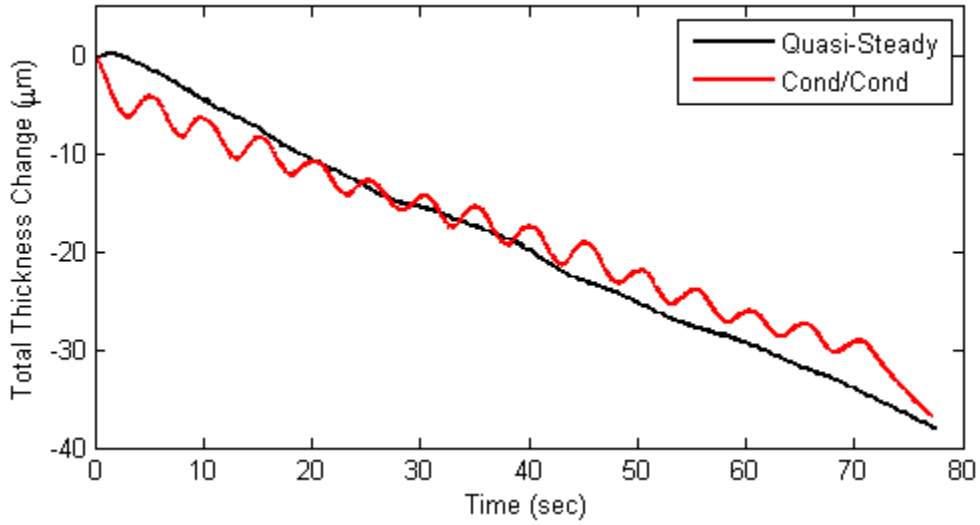

Figure 3.25. Evaporation rate comparison between the pressure-modulated experiment of the current section, and a batch-specific quasi-steady experiment. A negligible drop in the evaporation rate vs. quasi-steady conditions can be noted.

3.6 Modulated Superheat Films in the Presence of Hydrodynamic Disturbances (PID-controlled)

The results from previous tests suggests that the superheat-stopping method employed, more specifically, the control routine used to operate the inlet valve, did not provide for a quenching interval sufficient in length to achieve complete thermal equilibrium within the film during the off-time. By slowly quenching the evaporation, it was possible to obtain visual and

heat flux data for films throughout the entire evaporation process. However, the previous experiment evidently resulted in some combination of complex convective-conductive phenomena in the films during the condensing stages. Additionally, slow-superheat-stopping methods were not likely to lead to a significant gain in the net heat rejected by the films due to the very long "off-times" required (estimated to be in the order of minutes), to re-attain a quiescent film in thermal equilibrium with the substrate and vapor. These considerations motivated employing a more rapid means to increase the system pressure and more quickly quench the evaporation process at the film surface.

To accomplish this, in this series of experiments a PID routine to actuate the inlet valve was implemented in the VI. With this method, the inlet valve was set to match the cell pressure corresponding to null superheat. In theory, the PID controller would open/close the valve proportionally in order to reach the set pressure value. In practice, it was observed that pressure changes were so sensitive to valve opening that the PID essentially functioned in a binary mode as a fast on-off controller, reaching the set pressure in a scale of approximately tenths of seconds. It should also be noted that during the quenching periods, the Tescom controller was set to a value 0.5 kPa higher than the desired cell pressure corresponding to a null superheat. It was observed during experiments that both the Tescom and inlet valve were open simultaneously for a considerable portion of the quenching stage. By allowing sufficient vapor to enter the test cell, the vapor temperature was sustained during the entire quenching cycle, thus resulting in a more effective and faster superheat nulling than the one achieved through the slow quenching method discussed previously.

It should be noted that only cases $t_{off}/t_2 \approx 1$ were studied using the PID method described in this section. This was because the difference in the evaporation behavior observed between the

present control routine and the rest was negligible for $t_{off}/t_1 \approx 1$, and it was only for $t_{off}/t_2 \approx 1$ time scales that the PID-controller method presented here lead to different behavior in terms of heat flux and the evolution of the convective structures. The slow-condensing experiments discussed previously (Section 3.5) showed that as the cycles progress, the heat flux peak associated with t_1 diminishes greatly, significantly reducing the net heat rejected by the films over one cycle, thus decreasing the total averaged rate of heat rejection. Therefore, another added potential benefit of the current quenching method is a full reset of the thermal conditions of the film. This would in turn be expected to ensure that the heat flux spike associated t_1 would still occur, therefore positively impacting the net heat rejected.

Given the potential disturbance to the film associated with the PID-quenching technique it is important consider the impact of disturbing the film surface on the ultrasound thickness-measurement technique. The ultrasound system only accurately captures the distance between the copper surface and the liquid-vapor interface for the case of an undisturbed film, with a flat surface. For films with substantial interfacial waves, or any other disturbances which affect the flatness of the surface, the ultrasound data cease to accurately indicate the film thickness. This inaccurate measurement of film thickness also precludes the dynamic determination of the heat transfer rate at the evaporating film surface, given that the heat flux is calculated by differentiating the thickness change. Therefore, even modest fluctuations in film thickness result in relatively large and erroneous heat flux values. Although it is not possible to accurately determine the dynamic film thickness during the entire duration of the experiments due to the significant disturbance to the films during the quenching stages, it is possible to accurately measure the dynamic film thickness during the "on" portion of the experiments. These

measurements can then lead to the total mass loss, and therefore, a total heat rejected over the cycle.

3.6.1 Evaporating Films with Convective On/Off Time Scales, PID-controlled

The time-traces in film thickness and superheat level for a film subject to 5 superheat cycles under the PID-controlled conditions described above are shown in Fig. 3.26. The value of t_{on} in this case was 14 seconds (t_{on}/t_2 = 1.27) and t_{off} was 15 seconds (t_{off}/t_2 = 1.36. It should be noted that the last cycle was allowed to run for longer than 14 seconds in order to allow any possible remaining mechanical disturbances to dissipate, thus obtaining an accurate film thickness reading.). As seen in the Fig (3.26), all superheat cycles are virtually identical to one another. This suggests that the film achieved a uniform temperature during the condensing intervals. Therefore, every on-cycle was essentially equivalent to starting a new transient test in this case.

Another important element to note is that, by allowing vapor to circulate above the liquid film during the off-time, more re-condensation occurred (as previously discussed), than for the more gradual, non-PID controlled quenching experiment discussed previously in Section 3.5. This increased condensation was an undesired side effect of the PID control method and resulted in lower total net heat transfer rates. The trade-off is that rapid quenching through the PID control method results in the attainment of equilibrium conditions in the film, but results in the re-condensation of considerably more fluid. The slow quenching method discussed previously, by contrast, does not re-condense as much fluid, but also does not yield isothermal conditions within the film.

The absence of convective activity in the imaging data shown Fig. 3.27 (A and C) suggests the film has reached thermal equilibrium, which is in an agreement with the phenomena

captured by the ultrasound measurements. Comparison of Image A in the figure (stagnant film before superheat is applied) and Image B (onset of convective structure), for the first on cycle, with Image C (stagnant film at the beginning of the second cycle) and Image D (onset of convection for the second cycle), suggest essentially the same convective behavior was reached, and most likely, a similar penetration depth. Likewise, Images E and F show respectively the structure at the instant of the convective heat flux peak (t_2) and beginning of transition to quasi-steady structure during the last superheat cycle. Both of these images are consistent with the impulsive superheat film evaporation behavior previously reported by Kimball [[30]]. The fact that a t_2 convective structure is observed during the last cycle at a time equal (or as in this case, greater than the nominal t_2) strongly indicates that the film was completely thermally reset to the initial isothermal conditions, as suggested by the apparently lack of convective activity in Image *C.* Contrasting the last convective structure recorded for the film presently discussed with the structure from an ISF after a similar time of applied superheat (Fig 3.28) shows that, although the wavelength scale is slightly different (likely due to film thickness differences), the convective behavior are somewhat comparable in both cases. This also reinforces the point that each on-cycle was effectively the same as starting a new ISF experiment. The observed heat flux and convective behavior within the film using this type of control method contrasts with that seen in the experiments discussed in section 3.5, where lingering convection existed at the beginning of each on cycle, and the structure at the onset of convection was vastly different.

The net thickness of film evaporated during each superheat cycle for the current test is shown in Fig. 3.29. It can be seen that the first cycle yielded the lowest amount of evaporation, although subsequent tests only showed a gain in the total mass of film evaporated of approximately 10%. This gain evidently came from an increase in the heat flux peak associated

with conduction as shown in Fig. 3.29, B. It should also be noted that none of the cycles, except the last one which was subjected to superheat for approximately 19 seconds rather than the 15 seconds of all previous cases, exhibited the convective heat flux peak seen previously. This is not entirely unexpected since t_2 values for initial cycles were found to exhibit some variations with the shortest time being 7.8 seconds and the longest being approximately13 seconds. The reasons for these variations in the convective time are unclear at present. The peak heat flux occurred after 16 seconds of the application of superheat for that particular cycle, indicating the previous ones were not subjected to superheat for a sufficiently long time enough to capture t_2. The fact that the maximum convective heat flux occurred in the last cycle, and at an increased time from the ISF value, suggests that the film was successfully reset to initial conditions during each off cycle.

Comparing the current experiment with a quasi-steady test of equal, but constant superheat, shows that there was a considerable drop in the net heat rejected in the modulated experiment vs. the QS case (Fig. 3.30) . This was due to both, the relatively long condensing intervals, and the quenching method, which deposited more fluid back into the film than previous quenching routines. The data shown in Fig. 3.30 are summarized in Table 3.3 which quantitatively shows the large loss in evaporation rate with respect to QS conditions, despite of cycle-specific evaporation rates which were considerably faster than the mean QS evaporation rate. This net loss in evaporation rate albeit high rates during each on-cycle once again underscores the penalty induced by the re-condensation during the quenching stages.

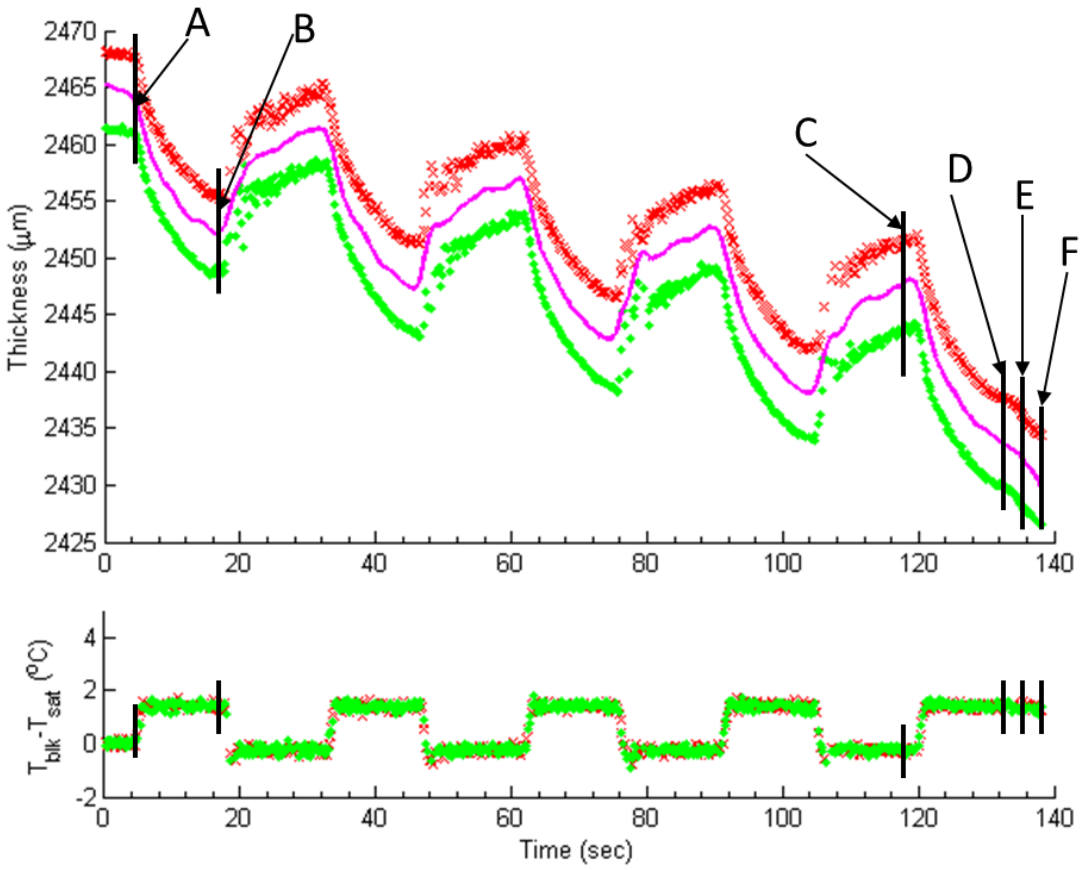

Figure 3.26. Evolution of thickness (top), and superheat (bottom) vs. time for a film evaporating under modulated conditions t_{on} = 14 seconds and t_{off} = 15 seconds.

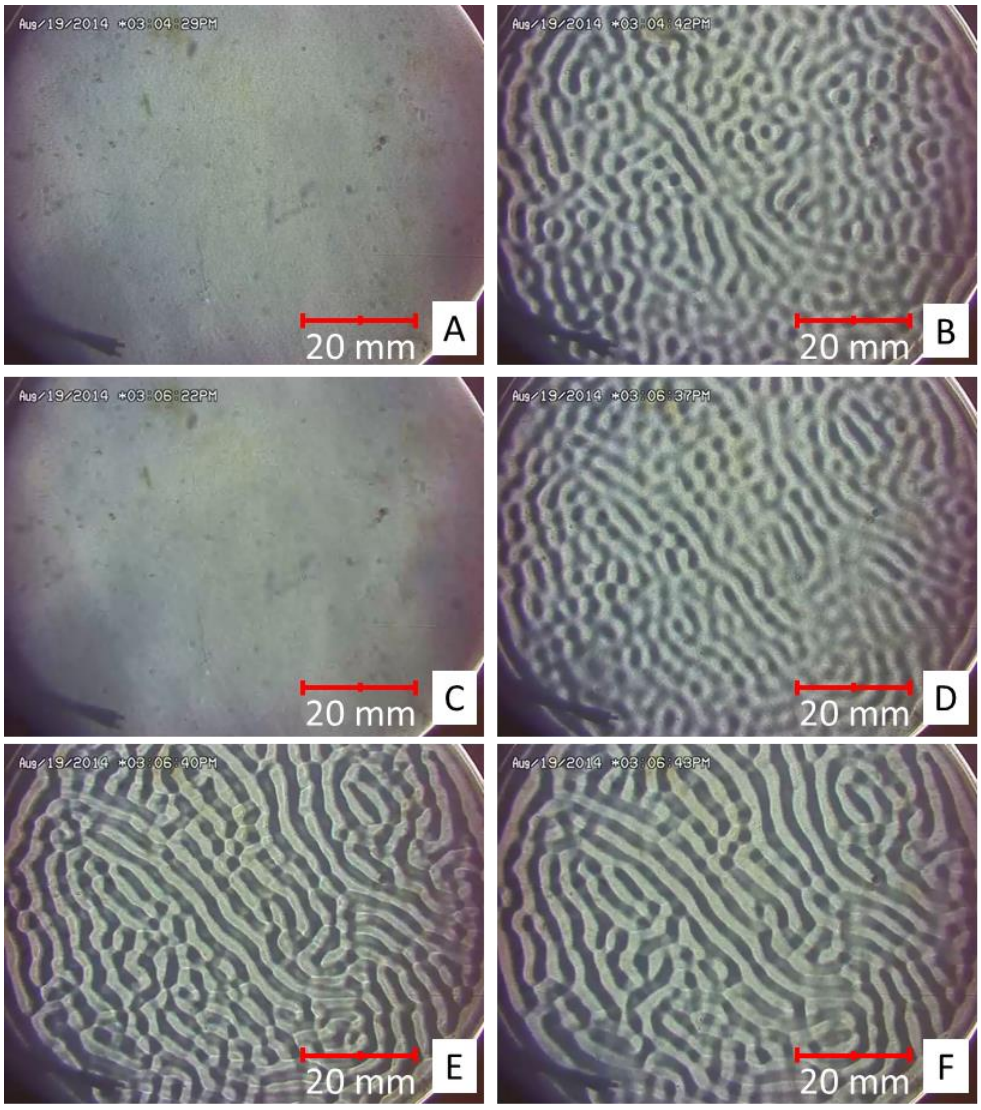

Figure 3.27. Schlieren images of the convective structure evolution of a film evaporating under modulated conditions t_{on} = 14 seconds and t_{off} = 15 seconds. The figure labels correlate to Figure (3.26).

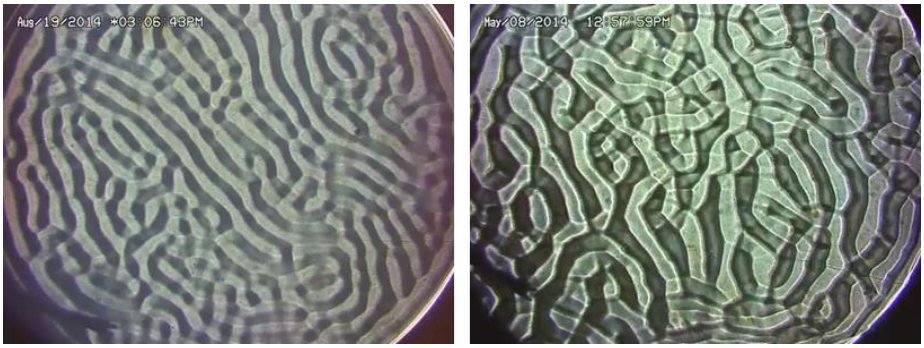

Figure 3.28. Comparison of the end-state convective structure for the current experiment (left) with the beginning to transition to QS structure for an ISF (right). Note that after 15 seconds on for the last cycle, the structure still had not reached QS-like convective structures, which is consistent with ISF.

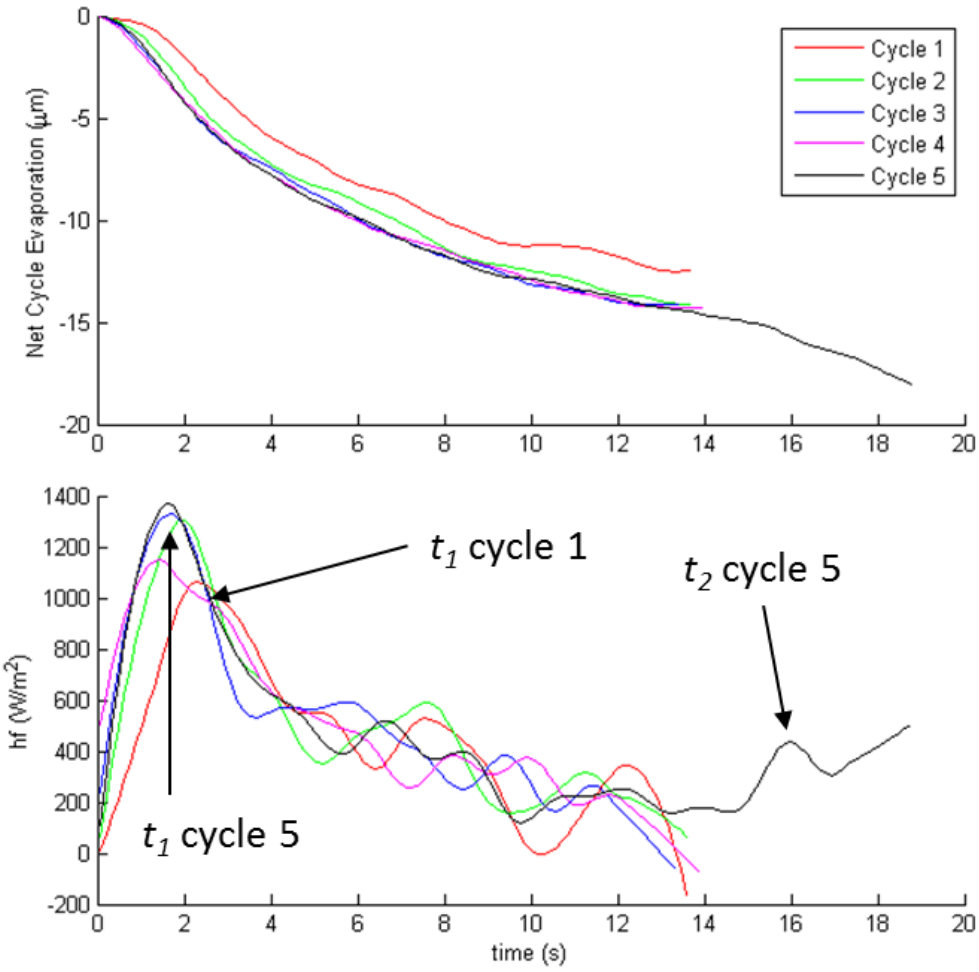

Figure 3.29. Time evolution of thickness (top) and heat flux (bottom) during the on-stages only for the film evaporating under pressure modulated conditions presently discussed (t_{on} = 14 seconds and t_{off} = 15 seconds).

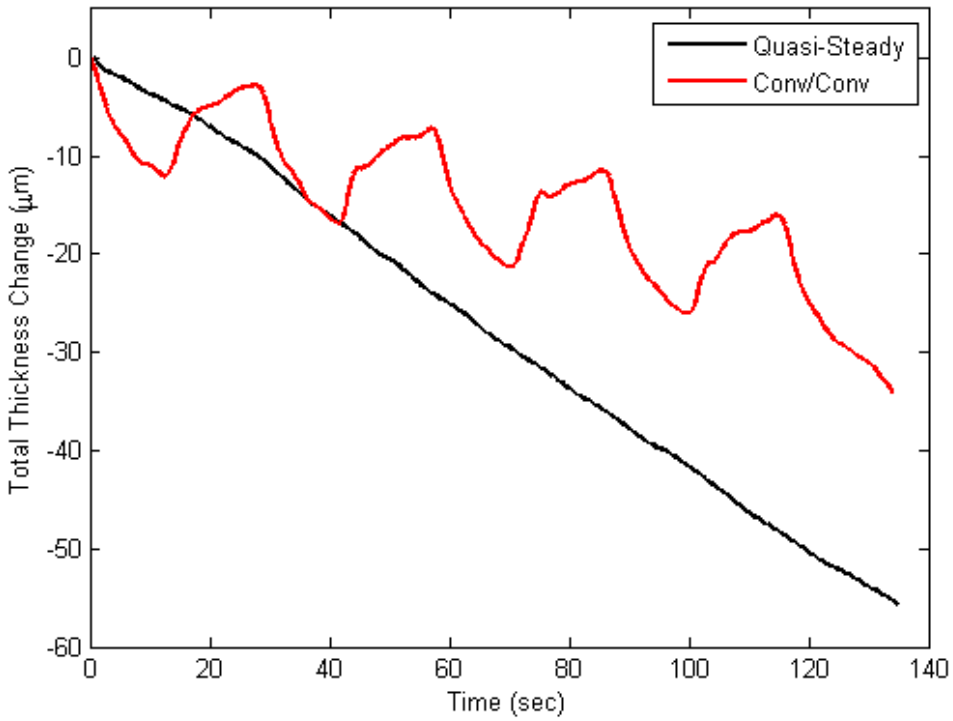

Figure 3.30. Evaporation rate comparison between the pressure-modulated experiment of the current section and a batch-specific quasi-steady experiment.

Cycle No.	Net thickness Change	t_1 (first cycle only) (s)	Cycle Evaporation Rate (μm/sec)	Cycle Evaporation Rate w.r.t QS (%)	Evaporation Rate from initial thickness (μm/sec)	Change w.r.t QS (%)
1	12.749	0.75	0.91	239	0.94	149.54
2	41.629		1.03	271	0.38	1.90
3	70.879		1.05	276	0.28	-25.19
4	100.119		1.02	268	0.24	-36.45
5	129.219		0.96	252	0.23	-38.45

Table 3.3. Quantitative progression of evaporation rate and comparison to QS with cycle number for the current experiment.

3.7 Modulated Superheat Films in the Presence of Hydrodynamic Disturbances (non-PID controlled)

The methods employed previously to raise the cell pressure and null the superheat during the quenching portion of each cycle allowed for the study of the convective behavior throughout the entire duration (or at least a considerable portion) of the experiments. This was achieved because the films were either minimally disturbed during the quenching process by hydrodynamic disturbances caused by the admission of vapor into the test cell, or the disturbances were not too large so as to completely disrupt the schlieren imaging data. However, none of the previous tests yielded a significant net gain in the heat rejected when compared with the quasi-steady baseline configuration. Factors adversely impacting the net heat transferred in previous experiments stemmed from the relatively slow nature of the process requited to stop the film superheating and the resulting re-condensation during such quenching intervals. In other words, the films would ideally need to be reset and thermally stabilized with minimal time loss, in order for the evaporation process to resume more quickly and achieve a net gain in the total amount of heat rejected. Therefore a new control method was implemented which favored speed of achieving a null-superheat condition over the hydrodynamic stability of the films during the quenching g process. The routine consisted of opening the inlet valve at the end of the superheat cycle to a relative high percentage (typically 70 to 90% of maximum aperture), for a typical duration of 1 second. This ensured a sufficient influx of vapor into the cell to rapidly raise the system pressure and null the superheat, while also minimizing the amount of re-condensation onto the film. This technique will be referred to as “rapid quenching” in this discussion. Schlieren images of the convective behavior during the re-condensation could still be captured for films with convective t_{off} time scales towards the end of the condensing cycle, but in general,

the schlieren images were adversely affected for most cases studied using the present quenching process.

3.7.1 Evaporating Films with Convective On/Off Time Scales (Rapid Quenching)

As was the case with the slowly-quenched tests presented previously, cycles with both convective t_{on} and t_{off} time scales were employed as a starting point. These time scales would only disturb schlieren images slightly, more specifically during the first few seconds of the condensing stages as vapor is admitted into the test cell. The film thickness-heat flux measurement however was also affected by the hydrodynamic disturbance imparted to the film due to the rapid addition of vapor in this case. Therefore, rather than calculating the heat flux for the entire experiment, heat flux data were only extracted for the on-cycles where reliable ultrasound measurements could be obtained

The thickness and superheat vs. time for a representative a representative rapid-quenching test are shown in Figure 3.31. For this test, the total cycle period was 30 seconds, split evenly between the t_{on} and t_{off}, resulting in normalized values of $t_{on/off}/t_2 = 1.36$. The inlet valve conditions were such that, when superheat had to be suppressed at the end of each on-time, the valve opened 90% of its max aperture, for duration of 1 sec. The change in film thickness, heat flux, and convective evolution were very similar to the slow test reported in section 3.5. ($t_{on/off}/t_2 \approx 1$) for the case of minimal mechanical disturbances. This suggests that for a combination of convective on and off-time scales, the inlet valve control routine based on the constant opening method does not represent a significant difference over the slow-proportional method in terms of heat transfer and convective structure development.

The typical behavior at the onset of convection and t_2, in terms of both, thickness evolution and convective behavior (Fig. 3.31, 3.32, points A, B) were observed in the current

experiment. However, as cycles progressed, these behaviors differed more considerably from the ISF, and continued to evolve from cycle to cycle, until reaching and end-state behavior, as shown in Fig. 3.32, points C through E. The approximate beginning and end of the quenching stage for that last cycle (number 11) are labeled in Fig 3.31 and 3.32 by points C and D. The convective behavior for the quenching stage in Fig 3.32, C and D, shows that convection was almost completely stopped (particularly evident in point D). This suggests that the quenching method was largely successful in reaching an isothermal state within the film.

The convective pattern before and after the structure transition associated with t_2 is shown in (Fig 3.32, Images E and F). It is evident from image E that the structure appeared considerably different from that seen in the ISF case at a time 2 seconds before t_2. In the present case, the structure had a longer wavelength, with features that appeared more diffuse that those of the ISF. This could be due to the partial level of quenching, which decreases the driving convective instability allowing more thermal diffusion to take place. The convective pattern at point F is consistent to the transition in structure typically associated with the heat flux peak at t_2. This is also consistent with the rise in heat flux for cycle 11 is seen in Figure 3.34 (bottom), 6 seconds after the application of superheat for cycle 6. This value of the convection-transition time is almost half of the nominal t_2 value of 11 seconds for the ISF, which suggests that, although convection is almost eliminated during the quenching cycles, the film did not achieve full isothermal conditions during the off stage.

The current t_{on}-t_{off} combination did not lead to an increase in the total heat rejected over the length of the experiment, and in fact, resulted in a net decrease, despite of the changes made to the quenching method. At the end of the second cycle, the evaporation rate of the current experiment was approximately equal to that of the quasi-steady case. After 11 cycles, there was a

large drop in the total evaporation to approximately 34% of the quasi-steady value (Fig 3.35). This decrease is attributed to the relatively long convective time scale of condensing cycles, during which the film is not rejecting heat. A summary of the changes in the total heat rejected versus a QS experiment of equal, but constant superheat is shown in Table 3.4.

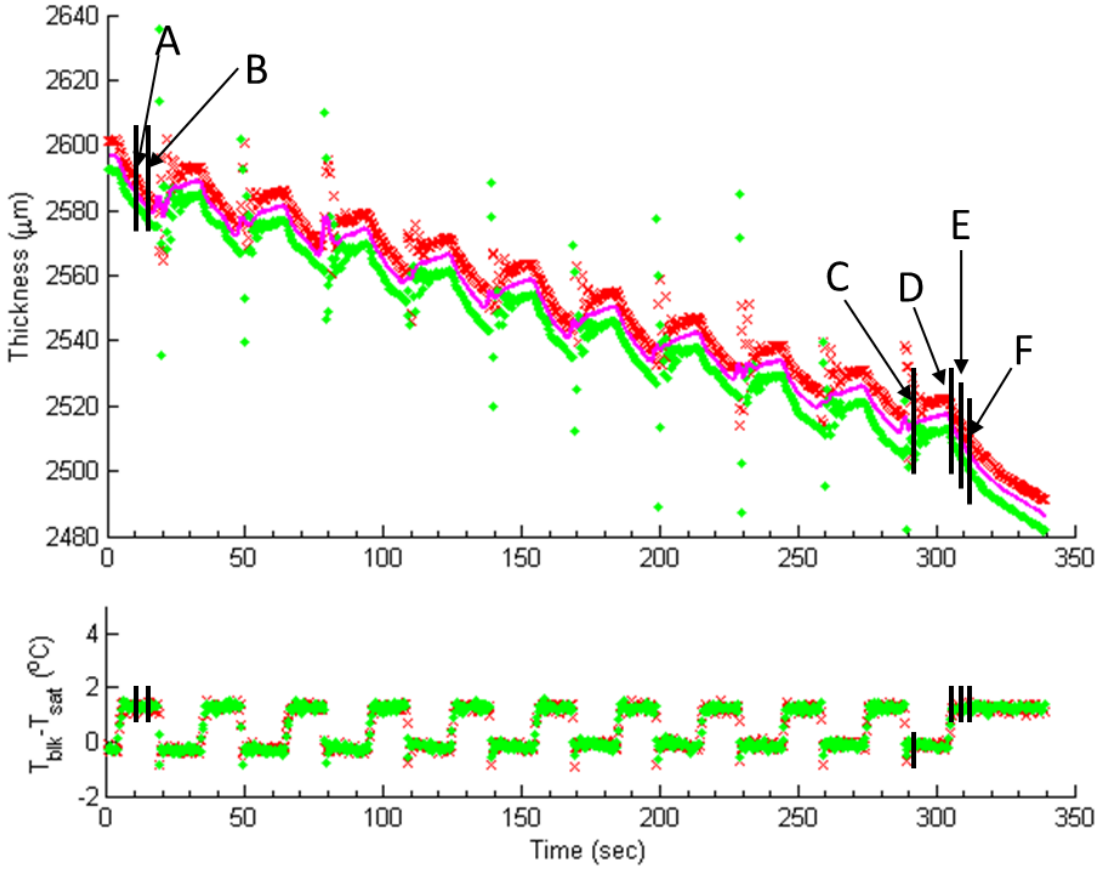

Figure 3.31. Evolution of thickness (top), and superheat (bottom) vs. time for a film evaporating under modulated conditions t_{on} = 15 seconds and t_{off} = 15 second.

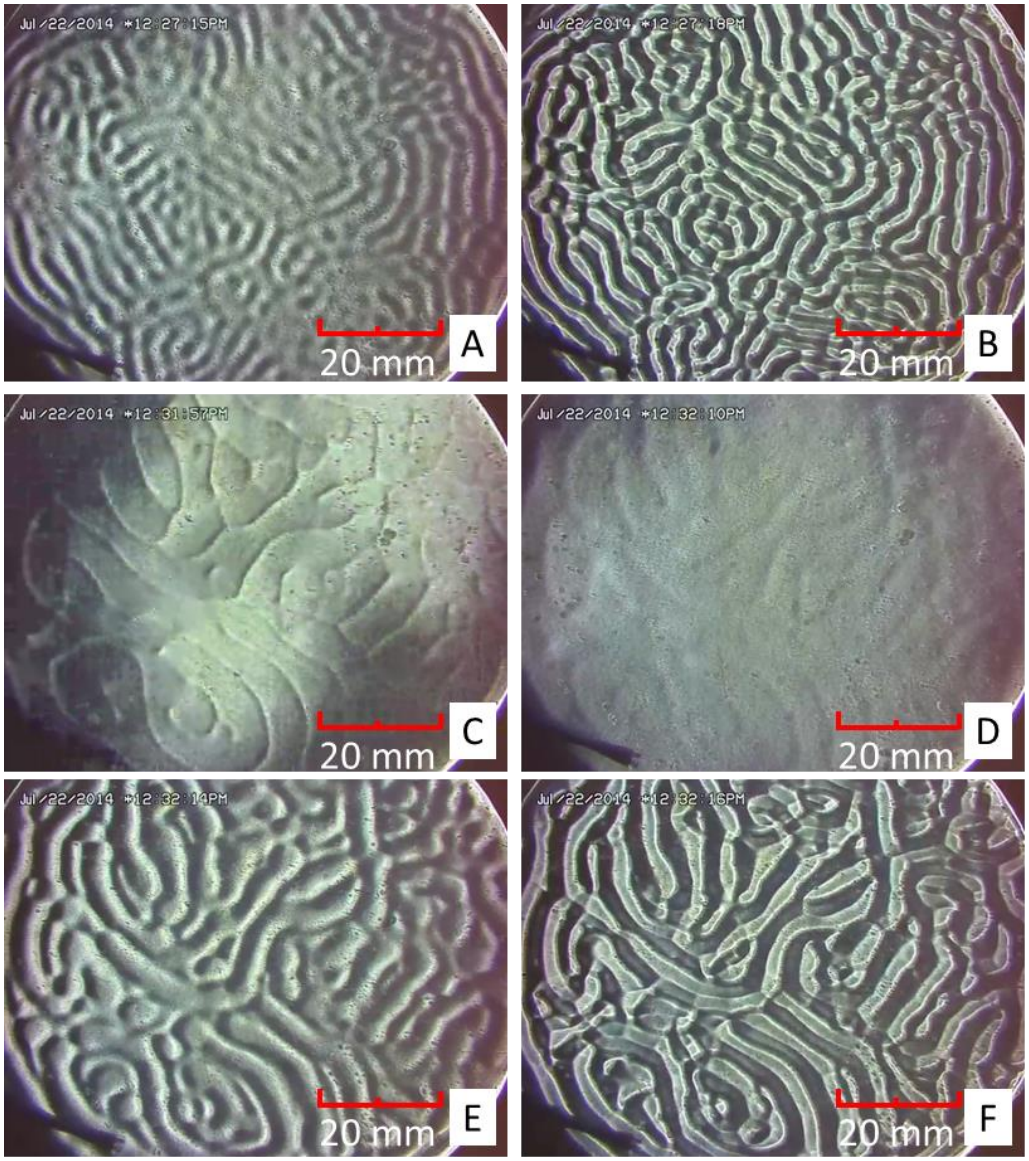

Figure 3.32. Schlieren images of the convective structure evolution of a film evaporating under modulated conditions t_{on} = 15 seconds and t_{off} = 15 seconds. The figure labels correlate to Figure 3.31.

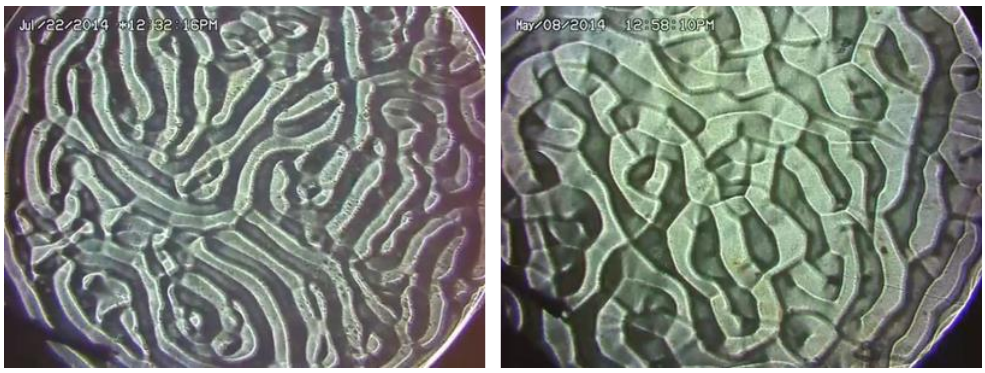

Figure 3.33. Comparison of the end-state convective structure for the current experiment (left) with the transition to QS structure for an ISF (right).

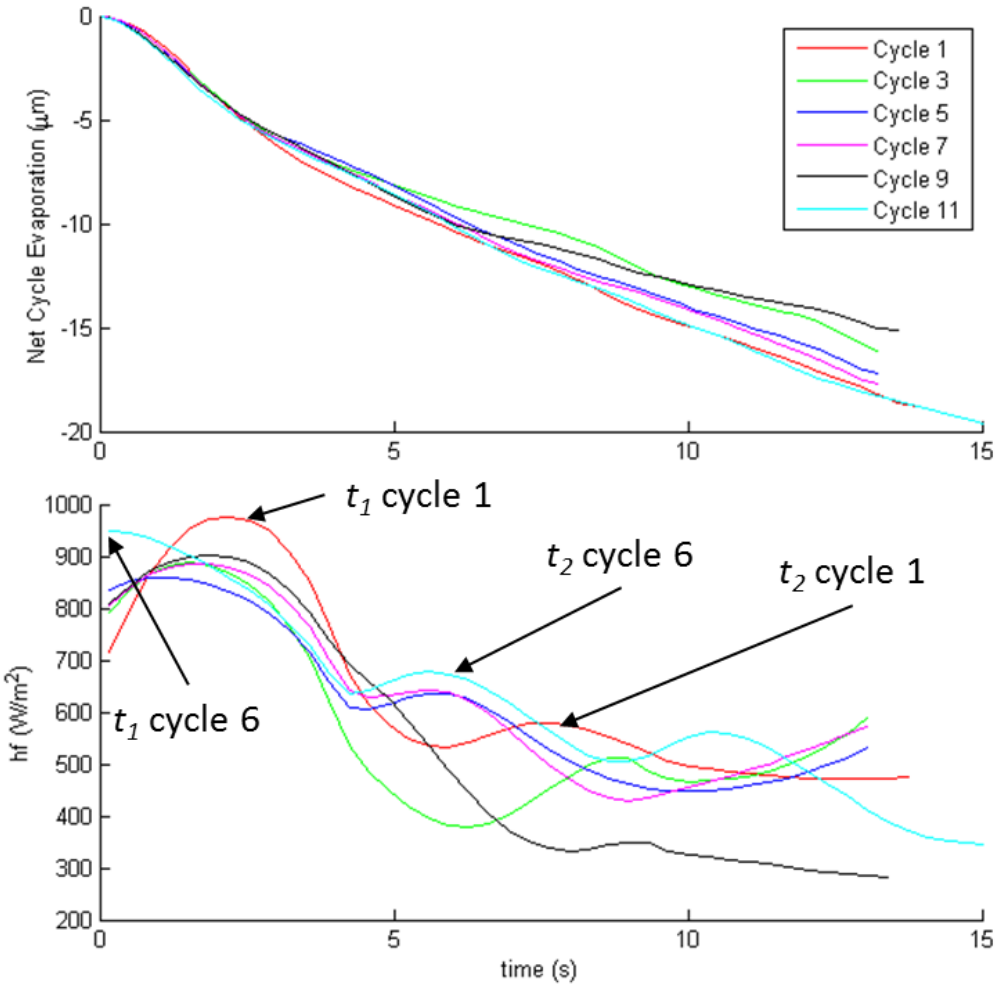

Figure 3.34. Time evolution of thickness (above) and heat flux (below) during the on-stages only, for the film evaporating under pressure modulated conditions described in the present section (t_{on} = 15 seconds and t_{off} = 15 seconds).

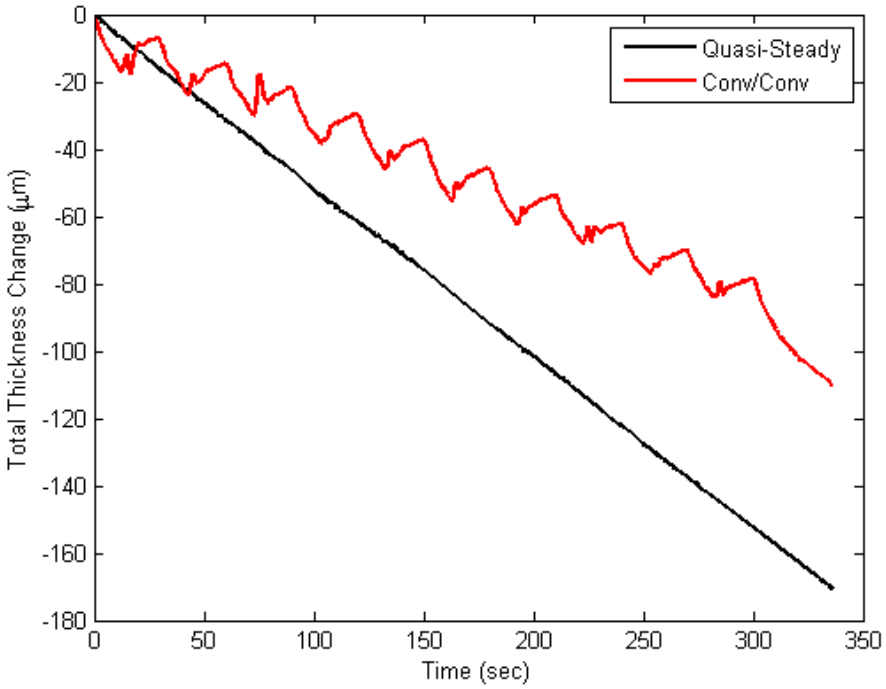

Figure 3.35. Evaporation rate comparison between the pressure-modulated experiment of the current section, and a batch-specific quasi-steady experiment.

Cycle No.	Net Thickness Change (μm)	t_1 (first cycle only) (s)	t_2 (first cycle only) (s)	Cycle Evaporation Rate (μm/sec)	Evaporation Rate from initial thickness (μm/sec)	Change w.r.t QS (%)
1	15.372	1.50	10.87	1.35	1.17	177.38
2	44.632			1.22	0.63	48.61
4	104.662			1.30	0.40	-4.94
8	224.662			1.34	0.33	-21.97
12	345.062			1.11	0.32	-25.17
20	584.762			1.31	0.29	-30.73

Table 3.4. Quantitative progression of evaporation rate and comparison to QS with cycle number for the current experiment.

3.7.2 Evaporating Films with Convective On-Time and Conductive Off-Time Scales (Rapid Quenching)

Even under rapid-quenching conditions, tests with t_{off}/t_1 >>1 did not yield the gain in the net heat rejected expected by exploiting the heat flux maxima documented previously for

transient evaporating phases. Therefore, with the faster quenching method presented in this section compared to the slower, proportionally-controlled method discussed in earlier sections (3.5 and 3.6), it was decided to decrease t_{off} to the level of conductive time scales. This was done in order to minimize the time films spent in the off, or evaporation-quenched state, and maximizing the total amount of time spent under superheated conditions. For the experiment discussed here, t_{on} = 15 seconds and t_{off} = 0.5 seconds, resulting in t_{on}/t_2 = 1.36, and t_{off}/t_1 = 0.5. Recalling the similar experiments conducted in previous sections, t_{off}/t_1 had a value of 2, thus the current value is four times shorter.

The thicknesses and superheat levels for a film of approximately 3 mm of initial thickness, subject to a mean superheat of approximately 1.2 °C are presented in Fig. 3.36. It should be noted again that for this particular type of test, given the substantial hydrodynamic disturbances imparted to the film during the quenching portions of each cycle, accurate ultrasound measurements could only be performed at the end of each cycle, when the hydrodynamic disturbances due to vapor flow had sufficient time to dissipate, leaving an undisturbed liquid-vapor interface. The evolution of the first cycle in terms of thickness change (Fig 3.36) and convective structure (Fig. 3.37) are consistent with those of the ISF This is particularly evident in Images A and B of Figure 3.37, which show similar convective patterns at the onset of convection and at the time of t_2 to the ones observed in ISF experiments. However, the rapid nature of the superheat quenching method employed in this series of experiments made ultrasound measurements unreliable during the start of the superheat cycles for this experiment since the film was still undergoing oscillations induced by the rapid admission of vapor at the beginning of each superheat cycle. By the end of each superheat interval, the film had settled, making the last point of each on cycle a usable reference to compare with the initial film

thickness. This allowed for the direct, quantitative comparison of the net heat rejected with the quasi-steady tests.

It was not possible to image the onset of convection for any of the cycles subsequent to the initial cycle due to the above-mentioned disturbances. Therefore, the representative schlieren images shown in Fig. 3.37, at points C through F, represent the earliest images for which the film was sufficiently stabilized to allow for visualization of the structure for cycles 3, 6, 9 and 11 respectively. The convective cells shown in Image C are more closely similar to the ones reported at the beginning of the transition to quasi-steady evaporation for ISF In contrast, the images shown in Fig. 3.37 D, E and F, exhibit structures more closely related to QS evaporating films. Invoking once again the combined thermal model developed in previous sections, this suggests that the middle layer has achieved a quasi-steady state in terms of temperature and penetration depth by the 6^{th} cycle. Thus, all temperature changes within the film were likely occurring only at the top layer during the current experiment.

A comparison between the convective structure at point F (approximately 3 seconds after the application of superheat of the last cycle) and that of the transition to QS for an ISF (Fig. 3.38) shows that convection cells in both cases are very similar. The fact that the last cycle of the current experiment reached that stage after approximately 3 seconds strongly suggests that there was a near-QS temperature profile developed through the film, which was minimally affected by the quenching stages.

A comparison between the results of the current experiment and a representative QS case is shown in Fig. 3.39. After 11 cycles, the experiment yielded a measurable gain in the total heat rejected. However, most of that gain spurred from the gains made during the first cycle since the overall slope of the pressure modulated experiment after cycle 1 was very similar to that of the

QS case. In other words, most of the gains in heat rejected were the result of the initial cycle, and the rest of the experiment behaved in a similar fashion to the QS case.

An experiment with identical t_{on} and t_{off} to the one just discussed, but with 31 cycles instead of 10 was also conducted. The film thickness and superheat evolution for this experiment is shown in Fig. 3.40 and are nearly identical to those of the previous test with 10 cycles. Comparing the experiment with 31 cycles with a QS test of equal, but constant superheat (Fig. 3.41), it is clear once again that the entire experiment could be treated as an ISF case evolving into a QS case, with the re-condensing intervals having modest to negligible effects. No schlieren images were captured for this test. The comparison of Fig. 3.41 is quantitatively summarized in Table 3.5. The gain in total heat rejected after the lapse of 31 cycles was modest, amounting to only 7 %.

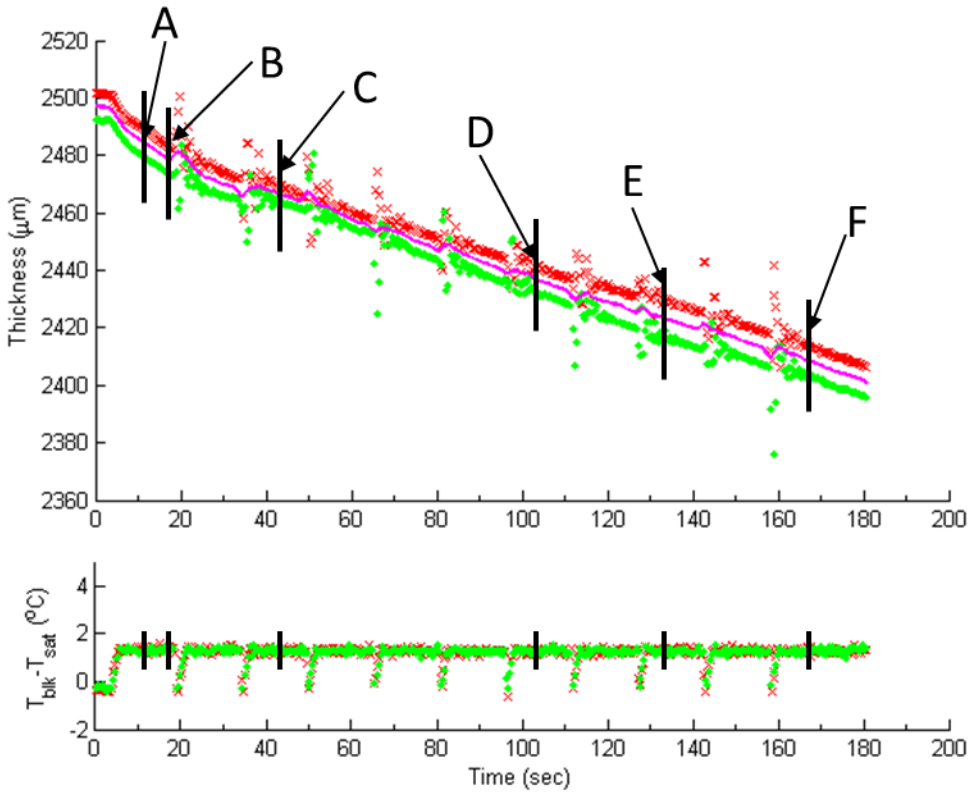

Figure 3.36. Time evolutions of thickness (top) and superheat (bottom) for a film evaporating under pressure modulated conditions, with constant-opening quenching controls and t_{on} = 15 and t_{off} = 0.5 seconds.

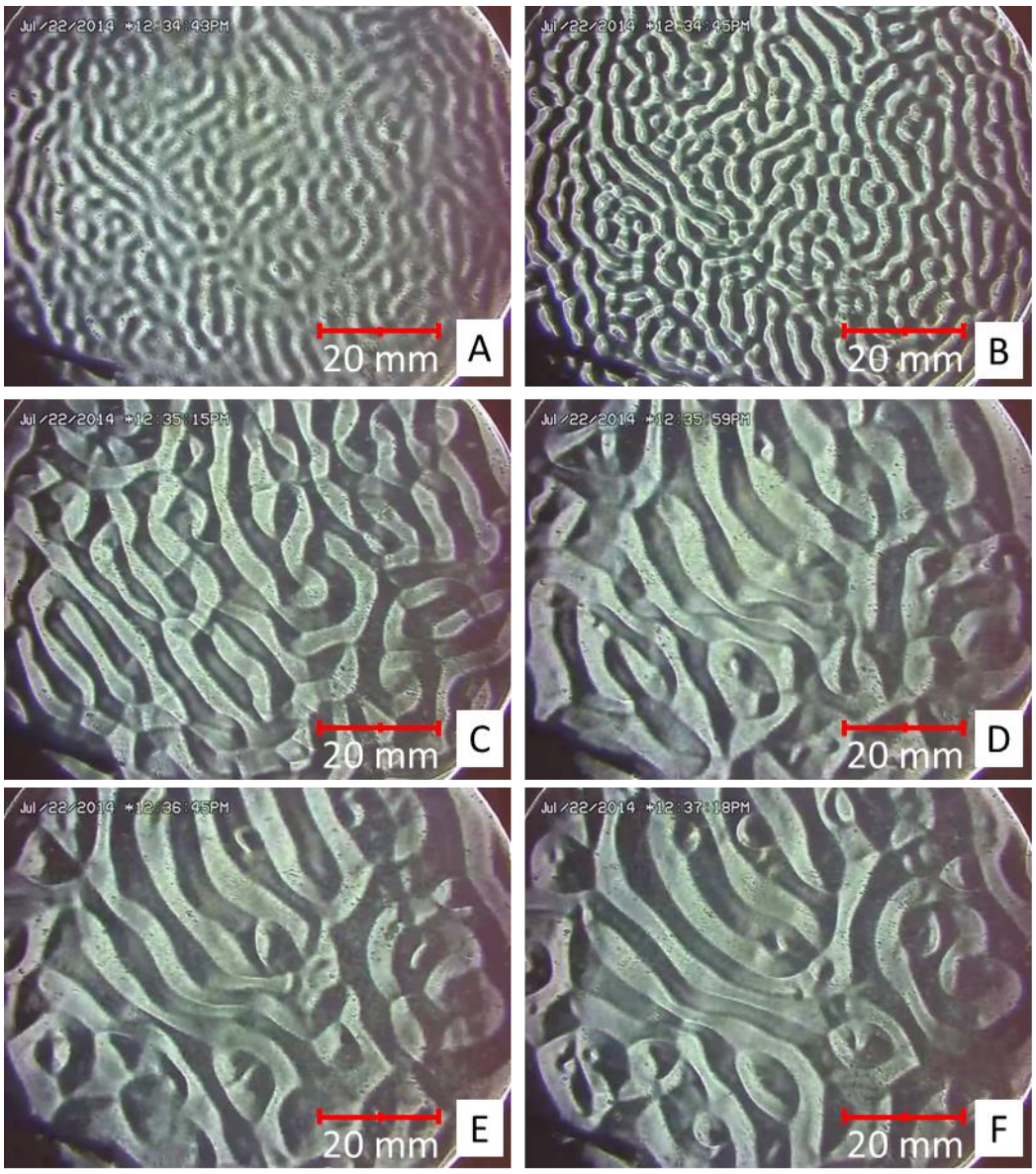

Figure 3.37. Schlieren images of the convective structure evolution of a film evaporating under modulated conditions t_{on} = 15 seconds and t_{off} = 0.5 seconds. Figure labels correlate to Figure 3.36.

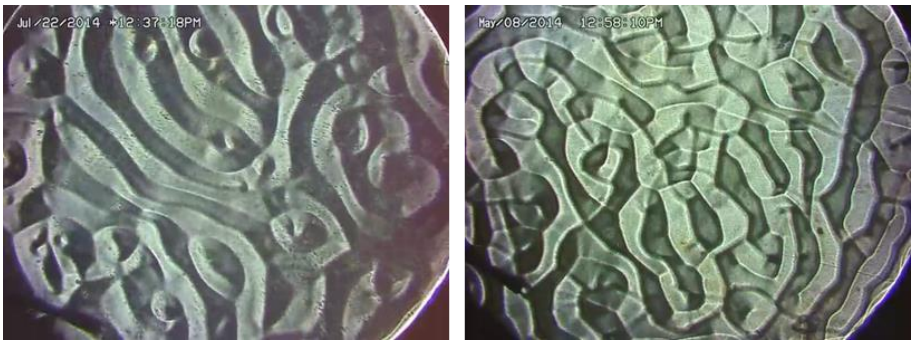

Figure 3.38. Comparison of the end state convective structure for the current experiment (left) with the transition to QS structure for an ISF (right). Note that the current experiment contained long wavelength structure similar to the QS, but there are several short wavelength cells visible.

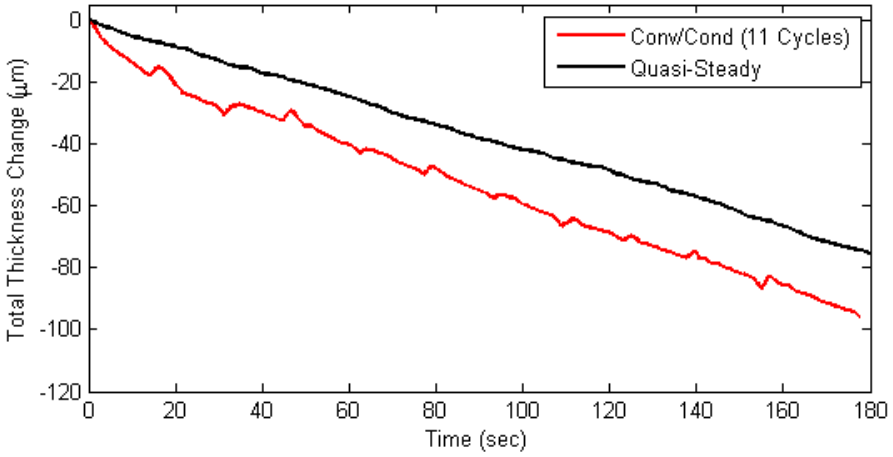

Figure 3.39. Evaporation rate comparison between the pressure-modulated experiment of the current section, and a batch-specific quasi-steady experiment. A modest gain in the net heat rejected of approximately 6% of the quasi-steady value after 11 cycles was reached.

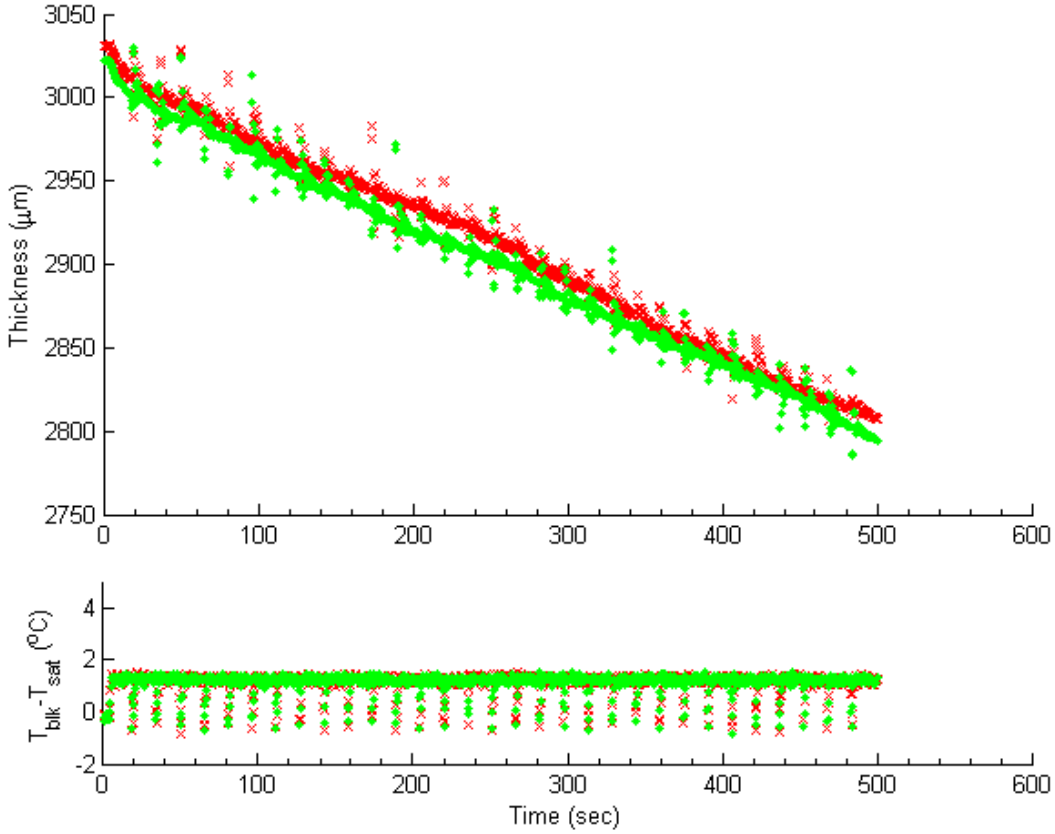

Figure 3.40. Time evolution of thickness (top) and superheat (bottom) for a film evaporating under pressure-modulated conditions, with constant-opening quenching controls, and t_{on} = 15 and t_{off} = 0.5 seconds.

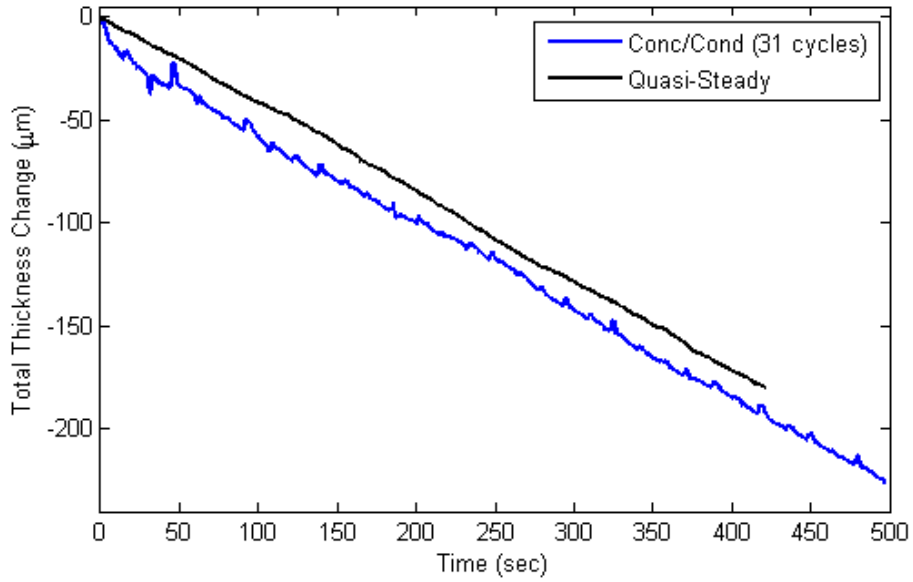

Figure 3.41. Evaporation rate comparison between the pressure-modulated experiment of the current section, and a batch-specific quasi-steady experiment. A modest gain in the net heat rejected of approximately 6% of the quasi-steady value after 31 cycles can be noted.

Cycle Number	Net Thickness Change (μm)	t_1 (first cycle only) (s)	t_2 (first cycle only) (s)	Evaporation Rate from initial thickness (μm/sec)	Change w.r.t QS (%)
1	14.634	0.75	10.90	1.30	207.56
2	29.634			1.01	139.81
4	60.764			0.66	55.94
8	122.694			0.59	39.01
12	184.494			0.51	20.69
16	246.394			0.47	11.52
20	308.694			0.47	12.04
24	371.294			0.47	12.29
28	432.494			0.47	10.64
31	478.994			0.45	7.32

Table 3.5. Quantitative progression of evaporation rate and comparison to QS with cycle number for the current experiment.

3.7.3 Evaporating Films with Conductive On/Off Time Scales (Rapid Quenching)

The result of the experiments described previously suggest that pressure-modulated cycles need to evolve relatively quickly (namely, operate on conductive time scales) in order to

potentially achieve a net gain in the heat rejected over multiple cycles. With the knowledge of the convective structure evolution, based on schlieren imaging, and heat transfer behavior obtained from experiments in which ultrasound and schlieren images were available, it is now possible to turn to tests with $t_{on/off}/t_1 \approx 1$. The rapid nature of these experiments resulted in substantial disturbances to the film that rendered the schlieren imaging unusable, and only allowed for thickness measurements at the start end of each test cycle. These two points however suffice for the calculation of a total evaporation which was used when comparing between the total heat rejected between this type of experiments and the QS case.

The time evolution of the thickness and superheat for an experiment with t_{on} = 3 seconds and t_{off} = 0.2 seconds is shown in Fig. 3.42. Both time scales fall within the conductive regime since t_{on}/t_1 = 3 and t_{off}/t_1 = 0.2. With such time scales, the film never had time to stabilize in between cycles following the hydrodynamic disturbance created by the vapor as it was rapidly admitted into the chamber. The length of the last superheat cycle was increased to about 15 seconds, which allowed the film enough time for the ripples induced by the incoming vapor to dissipate, hence resulting in a true ultrasound thickness measurement. This last datum provided the final thickness value just referenced, so the total thickness change was obtained. A direct comparison between the current experiment and a QS evaporating film is also shown in Fig 3.42. After an elapsed time of approximately 3 minutes, the current method had yielded measurable gain over the QS case. The quantitative comparison between these types of test and the QS case is shown in Table 3.6. It should be noted that since only the first and last points were usable for these tests, different experiments had to be conducted in order to get the thickness change at the last cycle, rather than, as in previous cases, obtaining the thickness values at the end of each cycle from the same experimental run.

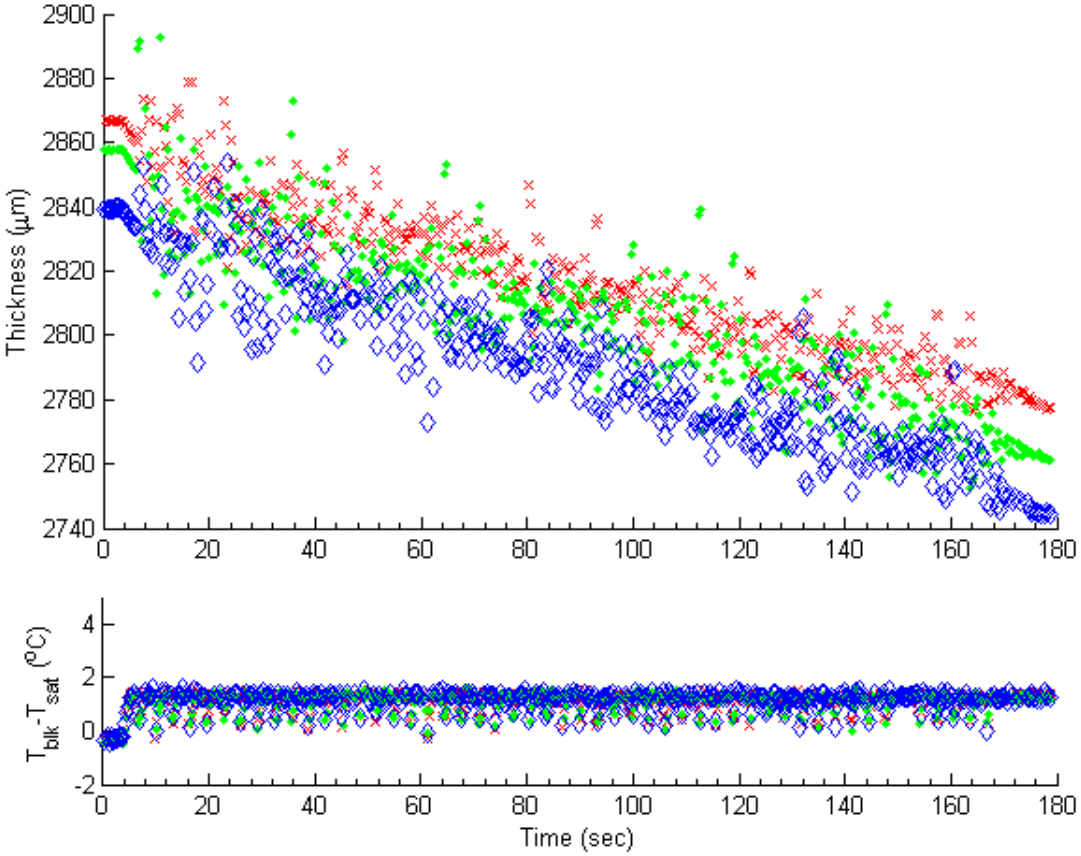

Figure 3.42. Time evolution of thickness (a) and superheat (b) vs. time for a film evaporating under pressure-modulated conditions, with constant-opening quenching controls, and t_{on} = 3 and t_{off} = 0.2 seconds. 50 cycles are shown.

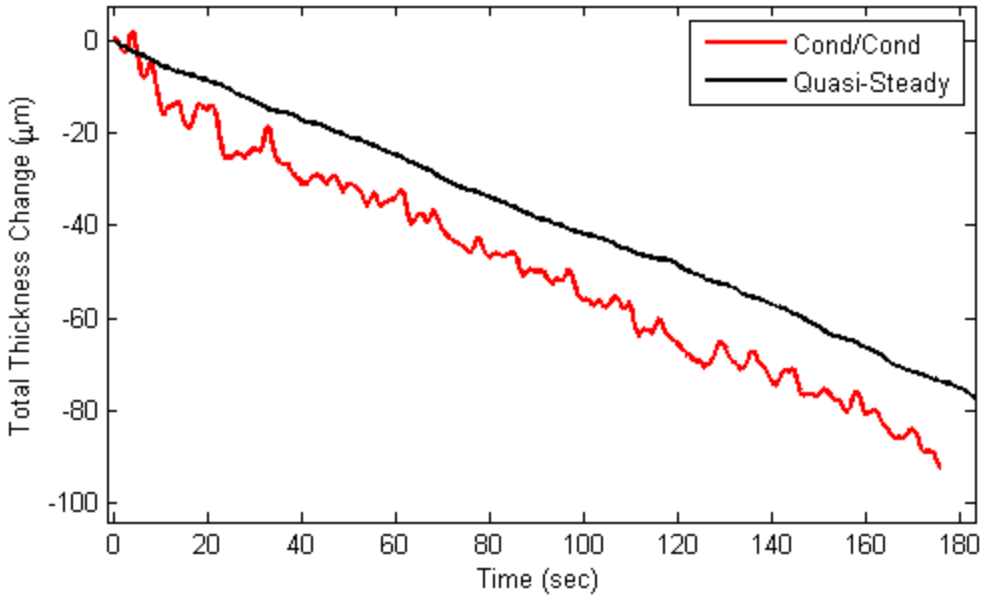

Figure 3.43. Evaporation rate comparison between the pressure-modulated experiment of the current section, and a batch-specific quasi-steady experiment. Both methods yielded nearly identical evaporation rates.

Experiment identifier	Number of Cycles	Net Thickness Change (μm)	t_1 (first cycle only) (s)	Evaporation Rate from initial thickness (μm/sec)	Change w.r.t QS (%)
6-11-14_11	1	2.539	1.20	2.76	568.49
6-11-14_12	2	5.722	1.03	2.27	449.80
6-11-14_13	4	12.374	1.30	1.61	289.95
6-11-14_14	8	25.316	1.30	1.03	149.47
6-11-14_15	12	38.256	0.85	0.86	108.30
7-22-14_05	18	64.142	1.11	0.70	63.12
7-22-14_06	30	99.362	1.13	0.56	31.04
7-22-14_04	50	169.148	0.75	0.50	15.46

Table 3.6. Quantitative progression of evaporation rate and comparison to QS with cycle number for the current experiment.

3.8 Quasi-Steady Evaporating Films with Mechanical Disturbance

A concern rose that the hydrodynamical and mechanical disturbances may have been partially responsible for the observed increases in the evaporation rate for the cases involving

rapid quenching discussed above (Section 3.7.). To assess this effect, a few experiments were conducted in which quasi-steady evaporating films, were mechanically disturbed while trying to match the scale of the interfacial disturbance patterns observed during the vapor admission in the rapid quenching experiments. The results from these tests suggest that mechanical disturbances do not contribute significantly to film evaporation or heat flux.

The test cell and associated hardware for these tests were essentially identical to the previous tests discussed in this work. Mechanical disturbances were introduced to the system using a push/pull solenoid actuator situated below the granite slab. The impact of the solenoid plunger generated a wave of sufficient amplitude so as to mechanically disturb the film as seen by visual imaging. A simplified sketch of this configuration is shown in Figure 3.44. The acceleration levels were captured with a tri-axial accelerometer attached directly to the test chamber. This accelerometer was the same one used during the microgravity experiments (see Section 4), so minimal re-assembling was required.

The actuation command for the solenoid was achieved in a similar fashion as that employed for the inlet valve in the LabVIEW *VI*. The routine required minimal modification, and provided the capability of specifying the frequency and on-time of the disturbance. The natural sloshing frequency for the film was calculated via equations (3.6 and 3.7) [[42]]. Mechanical excitation at this frequency was then performed to maximize the interfacial instabilities at the liquid vapor boundary, hence also maximizing the surface area of the interface. Eq. 3.6 considers very simple geometries (i.e. a cylinder), which differs slightly from the present configuration which contains an angled wall around the perimeter). In practice, the actual sloshing frequency can deviate considerably from the theoretical case, with several authors having introduced correction factors to be account of more complex effects than the simplified theoretical equation

presented in Eq. 3.6. The sloshing frequencies are also strongly dependent on fluid properties such as surface tension and density so very small deviations in these input values can significantly impact the adjusted resonant frequency value. The theoretically-predicted sloshing frequency is also a very strong function of the film thickness, however the thickness does not change significantly during these tests, and its starting value is known, allowing a viable estimate of the disturbance frequency. To ensure that the necessary parameter space was addressed, several mechanical disturbance tests were conducted over a broad range of excitation frequencies in which the value of the disturbance frequency was increased in steps of 0.1 pulses/second, from 0.5 to 1.8 pulses/seconds. This range of frequency was performed in order to ensure that the film was perturbed at its resonant frequency, either with the direct impact frequency from the solenoid excitation, or with higher order harmonics. As seen from the recorded spectra of the mechanical response of the system to the excitation (an example of this is shown in Fig. 3.45).

The test-cell configuration for all mechanical disturbance tests were identical to that employed all previously-discussed experiments, and the first steps during the initiation of the evaporation exactly followed those employed in the QS experiments up to about 60 seconds from the beginning of the data collection. At this point, the automated disturbance sequence was activated in the VI software. The disturbance was typically on for 15 cycles, after which it was stopped, and the quasi steady film evaporation was allowed to continue for approximately another 60 seconds. Thus it was possible, using the measured film thickness at the start and end of the series of 15 cycles, to determine the overall evaporation rate with and without the mechanical disturbance, which could be compared within the same experiment. The thickness evolution of a mechanically disturbed film undergoing QS evaporation before, during, and after the excitation is shown in Fig. 3.46. As it can be seen, no change occurred during, nor after the

excitation period, which would suggest that interfacial instabilities do not result in an increase of the evaporation rate.

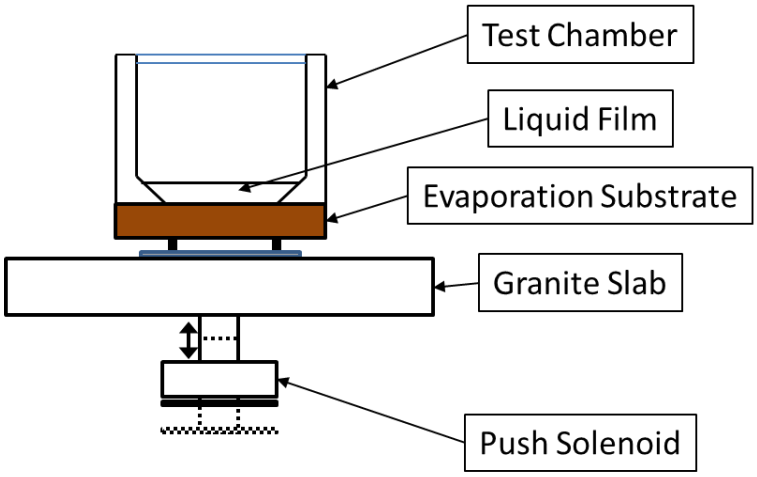

Figure 3.44. Simple sketch of the system employed for mechanical disturbance tests.

$$\omega_{1,1} = \sqrt{\left(\frac{g}{R}\epsilon_{1,1} + \frac{\sigma}{\rho R^3}\epsilon_{1,1}^3\right) tanh\left(\frac{h}{R}\epsilon_{1,1}\right)}\ , \tag{3.7}$$

and

$$f_n = \frac{\omega_{1,1}}{2\pi}\ . \tag{3.8}$$

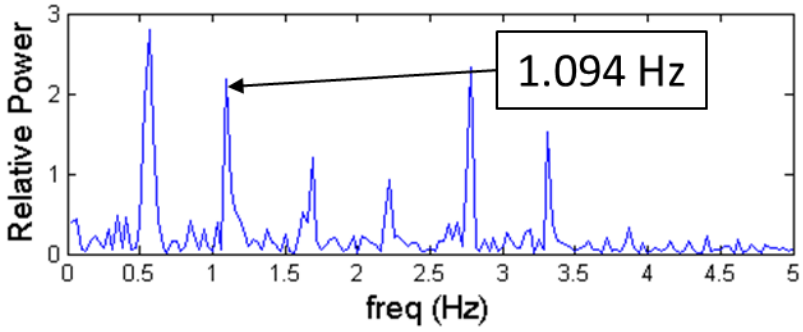

Figure 3.45. Recorded Excitation Frequency spectrum for a typical mechanical disturbance test. In this case the excitation frequency was 1.094 Hz.

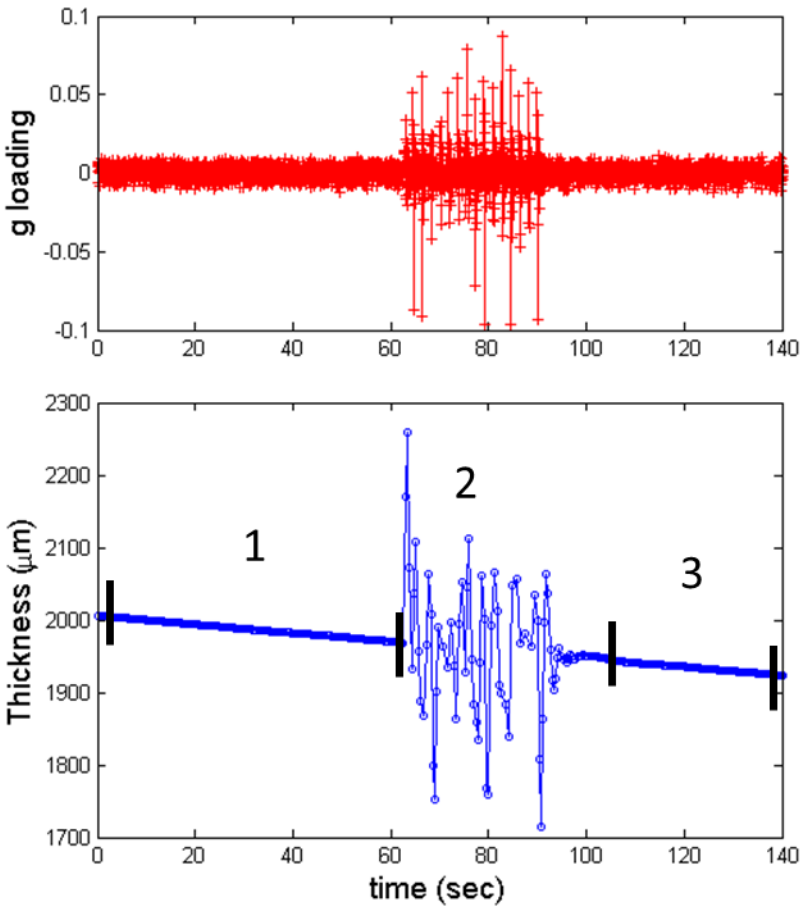

Figure 3.46. G loading (a) and thickness (b) vs. time for a film mechanically disturbed while undergoing evaporation.

3.9. Total Heat Rejection Discussion for Pressure-modulated, Evaporating Films

It was seen in previous sections the highest gain achieved in the total heat rejected with respect to QS experiments was approximately 15%. It is relevant to investigate how the heat rejected gains or losses evolve with cycles between the different combinations of t_{on} and t_{off}. Comparing fast quenching experiments of the three main t_{on}/t_{off} types (Convective/Convective, Convective/Conductive, and Conductive/Conductive) in the same graph with the mean slope for QS experiments reported for a superheat of 1.2 °C (Fig 3.47) shows that the Convective/Convective combination leads to a large loss while the other two time scale

combinations lead to a modest gain in the total heat rejected. Plotting the actual change in heat rejected versus QS (Fig. 3.48) shows that the evolution of all three up to approximately 40 seconds is very similar, with all yielding a gain in the order of 50% over QS. After 100 seconds, Convective/Convective cycles had yielded a small loss, which continued to decrease until reaching a steady state of approximately 32%. Both Convective/Conductive and Conductive/Conductive continued a nearly identical trend with the last recorded datum of the Conductive/Conductive having a net gain close to 15%. Presumably the Conductive/Conductive type of cycle would have continued the same trend as the Convective/Conductive, which after 480 seconds still maintained a modest gain of approximately 5 % over QS. The initial similitude in the trend of all cycle types, and particularly, the marked overlap of Convective/Conductive and Conductive/Conductive tests suggests that for similar t_{off} has a negligible effect in the overall thermal profile of the film. In other words, only the total t_{on} value matter regardless of the amount of t_{off} the films were subjected to. The data on Figure 3.48 suggest that the best results, meaning, the highest heat rejected during evaporation, might be achieved by running the Conductive/Conductive case for a duration of 100 seconds, immediately followed by quenching, and the restarting the evaporation. However, it was discussed in later sections how re-condensation negatively affects the total heat rejected, therefore, there would be practical limitations to the applicability of pressure modulated cycles.

In order to validate the previous conclusion, the film evaporation for all cycle types was plotted versus on-time (Fig. 3.49), rather than total time as previous plots. This type of graph could be analogous to evaporation efficiency. It can also be considered the evaporation rate if no re-condensation could be achieved during quenching, meaning, the theoretical limit of the maximum gain that can be achieved vs. QS conditions. In the plot it becomes clear that the on-

time evolution is very similar for all three cases for times up to approximately 150 seconds. However, after that, the Convective/Convective type of test exhibits a small gain in the film evaporation vs. on-time. This would suggest that condensing stage reset does have a small impact in the thermal reset of the film, hence yielded higher heat flux peaks values than the ones reached in the Convective/Conductive tests. The overall conclusion of the technical application of the pressure modulated cycles would be that the relatively large initial increase in the total heat rejected would make the cyclical evaporation more efficient over cooling relying on QS phase change, for devices which only need to be cooled for a relatively short period of time. For longer time operation, these results suggest that a sustained increase in the rate of heat flux would be possible only if the heat input associated with re-condensation could be somehow avoided.

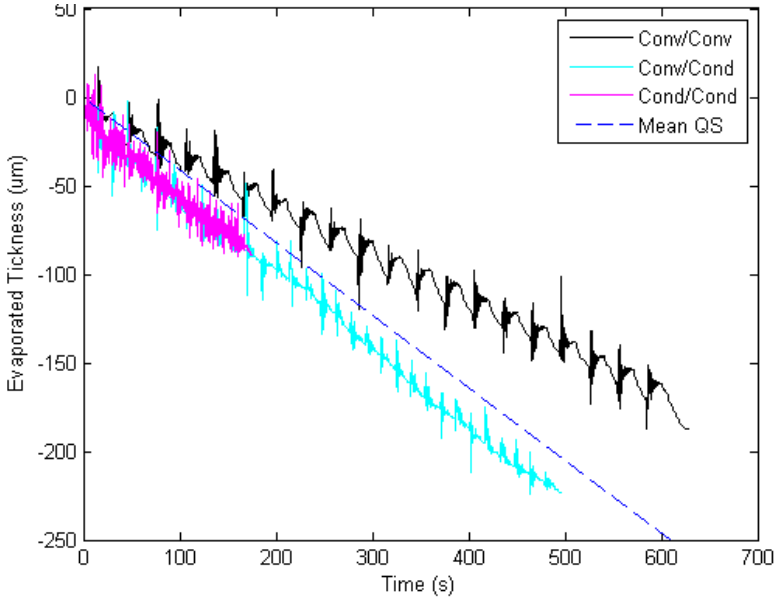

Figure 3.47. Thickness evolution of the main types of pressure modulated tests conducted (Convective/Convective, Convective/Conductive, and Conductive/ Conductive) in order to achive a gain in the total heat rejected w.r.t. QS.

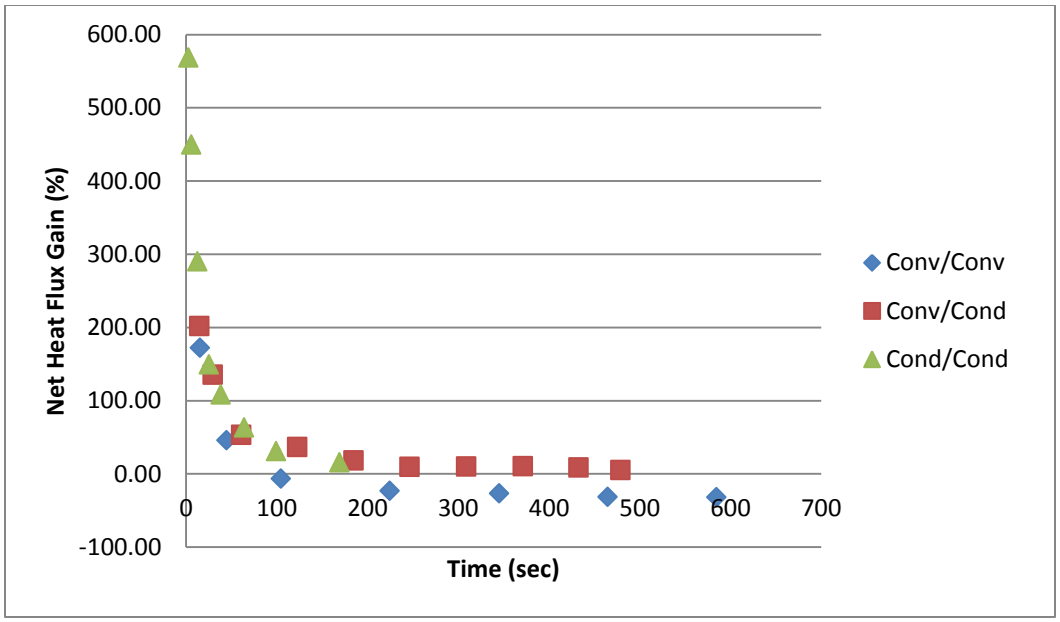

Figure 3.48. Comparison of net heat flux change for the main type of time scale combinations w.r.t. QS. The ordinate value of zero represents the QS condition.

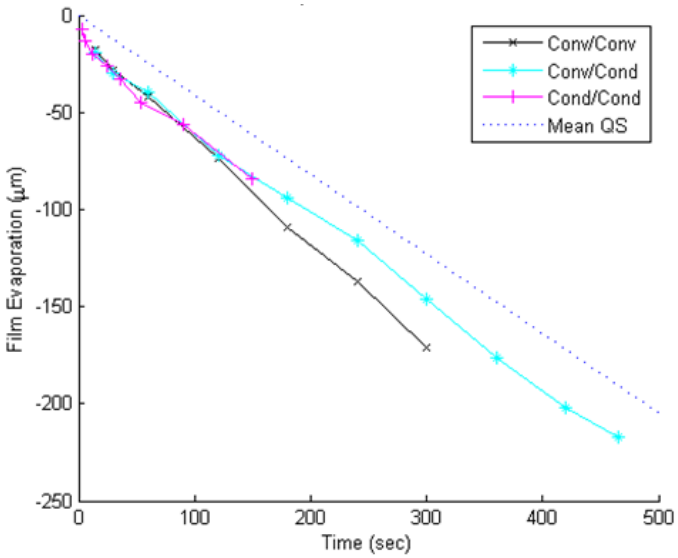

Figure 3.49. Comparison of film evaporation vs. on-time for the three main cycle types and the mean QS evaporation rate observed.

3.11 Particle Imaging

The phenomena associated with convective structure and penetration depth in transient film evaporation has been discussed previously. An experiment was devised in order to further explore the convective behavior during transient evaporation. The experimental concept was to deposit some type of fluid-visualization tracer (particles, dye, PH indicator) at the bottom of the evaporating film, which would allow detection of the convective structures as they engaged the entire film and reached the solid surface. This naturally assumes that the convective behavior starts at the film surface and propagates downward through the film.

The original experiment designed called for two sets of particles, one set, slightly lighter than working fluid and another set slightly heavier. Such particles, properly coated particles could fluoresce at different wavelengths, potentially requiring two different light sources. Our goal was to be able to differentiate the convective behavior at the free surface from that at the bottom of the film

It was decided that sinker tracers would be easier to implement, as well as have the least impact on the experimental conditions since they would not affect the heat transfer between the liquid and vapor. To evaluate the practicality of this technique, a preliminary open-air test was then conducted with Teflon shavings. The density of Teflon is 2.2 g/cm3, which is approximately 65% heavier than DCM. The shavings were produced in-house by sliding a blade across the edge of a Teflon block. The resulting “particles” had a considerable size and shape spread, going in from 3 mm curls down to about 0.2 mm particles. Teflon was chosen as a good material due to its chemical compatibility with DCM, its higher density, and the ease of removing it from the test chamber. A DCM film was directly deposited on the evaporating surface, and the Teflon shavings were added to it. Due to the relatively high vapor pressure of

DCM, evaporation in the film naturally commenced without the need for superheating in this case. Real-time visualization of the Teflon particles revealed several technical issues. Some of the biggest particles did not sink due to surface tension, and the resulting meniscus surrounding the floating particles made it difficult to detect any useful motion as well as visually disturbing large areas of the film, making it difficult to detect the "sinker" particles. In the case of the sinking particles, the largest particles that made it to the bottom were apparently were too heavy to be displaced by any of the convective structures. The smallest detectable particles were observed to move, presumably under the action of the convective activity. However, it was quickly noted that their motion did not follow any of the visible convective cells indicated by simultaneous schlieren imaging. Rather, the particles appeared to move in an approximately linear fashion, which would suggest high Stokes numbers. These particles were also difficult to visualize, at times completely disappearing from the camera when transitioning under the dark edges of the convective cells. Both schlieren and shadowgraph imaging techniques were attempted, and they both yielded very similar results. After the preliminary results with the Teflon tracers, it was decided not to perform further visualization experiments with particles.

Another option considered was to employ dyes, rather than particles, as a fluid visualization technique. A special "heavy" dye mixture was prepared in house by dissolving Cesium Chloride (CsCl) in water and adding colorant. This solution was immiscible with DCM. The relatively high density (3.99 g/cm^3) and solubility of CsCl in water (approximately 0.5 volumetrically) ensured the dye layer could be deposited between the DCM layer and the copper substrate. Although the dye layer proved to be stable in terms of staying below the DCM layer, and not mixing with it for extended periods of time, none of the tests did lead to successful visualization of the penetration depth evolution.

Chapter 4. Reduced-Gravity Experiments

4.1 Background and Motivation

Many space-based applications, such as humidity control, capillary pumped loops, and water purification depend heavily on phase change. [[43]] Long-term human missions like those proposed by NASA depend critically upon successful and efficient phase change in a microgravity environment. However, relatively little is known about the physical processes behind microgravity evaporation, in particular that of thin liquid films. The current state of knowledge of film evaporation processes under reduced-gravity conditions highlights the need for zero-g experiments, in order to achieve a better understanding of this process [[44]]. The low-gravity experiment undertaken as part of this research aimed to describe the fundamental investigation of the mechanisms operative during film evaporation processes in reduced gravity and the corresponding impacts on the dynamic film structure and on the heat transfer. Also of interest is the evolution of the convective structure within evaporating films in reduced gravity, where thermocapillary effects may persist but buoyant convection will be greatly diminished. The impact of all of the above on the heat transfer due to the film evaporation is also a central consideration in this work. In addition to terrestrial applications, the high heat flux associated with phase change in an important consideration in spacecraft thermal control applications.

In principle, evaporating films in microgravity should be simpler to study than those in standard-gravity conditions, because all convective behavior due to buoyancy (*RB* convection) effectively disappears in reduced gravity. In the absence of buoyancy, other interfacial phenomena such as thermo-capillary driven convection (*MB*, non-uniform evaporation rate and vapor recoil may become the driving forces [[45]]. It should be noted that, unlike the case of

heated films, the Marangoni effects during film evaporation are expected to be considerably weaker due to the suppression of surface temperature variations induced by the evaporation [[30]].

However, the practical challenges and limitations associated with conducting experiments in microgravity add a considerable layer of complexity to the problem. A significant limitation is the limited test times (approximately 15-20 seconds for the aircraft case), for experiments which need minutes to execute, as seen in the normal-gravity results presented in Section 3. Another concern is the poor low-gravity quality aboard the aircraft, and although drop towers can provide much more stable micro-gravity values, they offer even less test time (5 seconds or less). The relatively high cost of conducting experiments in microgravity also represents another limitation.

As part of the present investigation, film evaporation experiments under reduced-gravity conditions were conducted aboard the zero-g aircraft. The experimental system, procedures and preliminary results from such tests will be described in the following sections.

4.2 Experiment System Overview

As previously mentioned, the reduced-gravity experiment was very similar in terms of basic operating principles to the laboratory experiment. Therefore, both contained analogous systems and overall components. However, the fact that tests were conducted aboard a reduced-gravity platform induced several changes to the system. These changes resulted from reduced experimental times, reduced maximum allowable size and weight of the experimental system, and increased structural strength of the required of joints, brackets, and components in general. The test platform consisted of the Zero-G Corporation Boeing 727 aircraft flown out of Ellington AFB, in conjunction with NASA. The aircraft flies in a specific parabolic trajectory in order to achieve the desired reduced gravity levels, which could be near-zero, Lunar or Martian. The

experimental system was rigidly attached to the floor of the airplane, therefore, undergoing the same reduction in effective gravity levels.

The experimental procedure on board the aircraft involved establishing a preheated film in the test chamber at the start of each low-gravity interval. Evaporation was initiated by rapidly decreasing the pressure of the saturated vapor in a similar fashion to the laboratory experiments conducted in this investigation, while also keeping a constant temperature of the evaporating surface. Evaporation was stopped at the end of each low-gravity cycle. Due to the limited experimental times and system footprint, the controls system were considerably different from the laboratory set up. A volume-compensation technique was implemented for rapid control of the chamber pressure. Additionally, the copper block was not water cooled, which would have required a relatively heavy and bulky chiller. Instead, the plate temperature was controlled by a set of compact and lightweight thermo-electric coolers (TEC's).

Arguably, the biggest impact upon the aircraft system was the required compliance with high g-loads set forth by the NASA Reduced Gravity Office (RGO). The most stringent of these requirements specified that the entire system would be able to structurally withstand 9 g's in the forward direction of flight. The resulting high structural strength required of all components largely dictated the materials, frame type, fabrication and positioning of equipment in the system.

4.3 Hardware Description

The experiments that were conducted in reduced gravity were analogous to the ones conducted in the lab. Therefore, the experimental system shown in Fig. 4.1 was analogous in terms of basic functioning parts, systems, and functions carried by each of the components. Each system in the reduced-gravity experiment will be simply described in the following sections.

4.3.1. Fluid Handling System

The fluid handling system consisted of closely analogous components to that of the laboratory system. The biggest difference in terms of functioning parts consisted of the volume compensation bladder, expansion chamber, and buffer tanks, which will be described below. However, both systems aimed to achieve a controlled isolated environment in which the working liquid and vapor could be thermodynamically controlled.

The main component of fluid handling system was the test cell, which contained the working fluid. This chamber was constructed of steel in order to ensure compliance with the high g-load requirements set by the RGO as mentioned above. The evaporating surface consisted of a copper block similar to the one used in the lab experiments. The copper block had a flat surface at the top on which film evaporation was carried out and it contained several ports for the ultrasound transducers and temperature probes on the underside. The copper block attached rigidly to the test cell through 12 5/16 bolts to comply with the high loading already stated. A Teflon ring with a mating angle of 45 degrees was added to the evaporating surface with the purpose of eliminating the meniscus, which in reduced gravity would have a major impact on the thermocapillary effects. The top of the test cell consisted of a glass plate used for the schlieren system, and overall optical access. A side port of the test cell was sealed with a copper block ¼ of an inch thick, and cooled from the outside by a set of TEC's. The surface of the block exposed to the vapor inside the cell acted as a condensing surface on which excess vapor could be collected. Two ports in the front of the chamber allowed for instrumentation access, as well as a way of admitting the working fluid.

Another chamber port directly communicated with an expanding/contracting bladder, which was housed inside a pressure controlled chamber. The expansion chamber connected to

the vacuum pump, as well as two tanks which acted as pressure buffer devices. A three-way valve controlled the flow of air into or out of the expansion chamber. By controlling the pressure of this chamber, the volume of the bladder was also controlled, therefore effecting relatively big changes in pressure inside the test cell, and hence controlling experimental conditions. It should be noted that the main reason for changing the lab EPR to the bladder as a mean to control the test cell pressure was to minimize weight and preclude the need for a separate vapor-supply and exhaust system. This change was essential in meeting the NASA specified weight and size specifications.

Two solenoid valves controlled flow of vapor and/or from various parts of the system. Two safety valves were also included in the system, which would discharge vapor outside the aircraft cabin in case of over pressurization.

4.3.2 Diagnostics Systems

The diagnostics systems consisted of the shadowgraph to capture the convective behavior, ultrasound to record the film thickness, and thermodynamic probes to gather temperature and pressure data. There were also LabVIEW-based control systems which directed the valves, light source and pump.

The shadowgraph system was very similar to the one employed for laboratory tests. This system had to be considerably more compact, rigid, and light than the lab-based one. A smaller parabolic mirror (6 in diameter, f6) was used in this case, and several adjustable mounting brackets were fabricated. The light source used during flight was the LED described previously.

The ultrasound system was identical to the one used in the lab, as was the post processing of the thickness data.

A USB 6351 National Instruments acquisition card was the centerpiece of the diagnostics systems in the reduced-gravity experiments. The NI card relayed the temperature data from the evaporating surface and the vapor inside the test cell to the computer, the pressure inside the test and expansion chambers, and g-loading data. The NI card also carried out control tasks through several DIO channels. These included light source, vacuum pump, fans, and most importantly, the bladder that effectively controlled the superheat level.

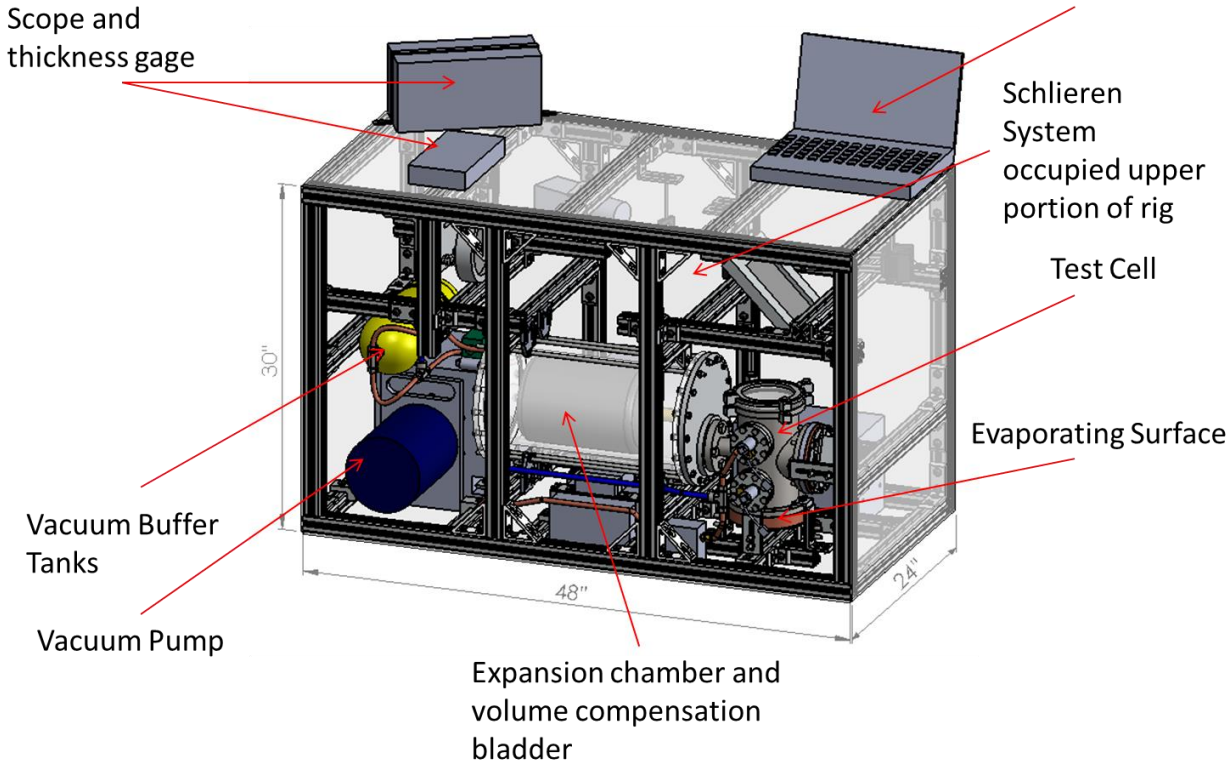

Figure 4.1. Reduced gravity experimental equipment with outlined dimensions and main subsystems and components highlighted.

The working fluid of choice was once again was dichloromethane (CH_2Cl_2) for the reasons stated previously. The amount of fluid needed to run the experiment was approximately 30 ml (about 1 fluid ounce).

Based on laboratory results, the establishment of the evaporation flow patterns for DCM films of the thicknesses considered here (approximately 3 mm) require time scales of at least 15 seconds. The 15-20 seconds of reduced gravity available on board parabolic-trajectory aircraft were expected, in principle, allow examination of the transient behavior associated with the onset of film evaporation, and provide some insight into the subsequent quasi-steady state evaporation condition.

4.4 Experimental Procedure

The overall experimental procedure aboard the parabolic-trajectory aircraft, while aiming for the same thermodynamic conditions as those in the lab experiments (a sufficiently degassed chamber before inclusion of the liquid, impulsive decrease of chamber pressure to induce superheat...), was conducted in a considerably different manner. This was mostly due to the effects of aircraft in terms of timing, safety and available resources.

The test cell was degased prior to take off (although for a much shorter time than the 24 hours typically allowed in the lab) yet, to a sufficiently satisfactory level. Once this level was reached, liquid DCM was introduced into the test cell. This was done by connecting a syringe with to the chamber, with a valve separating both systems. Once the valve was opened, DCM flowed into the test cell. This processed was repeated while on the ground a minimum of 3 times, in order to ensure that all non-condensables were evacuated from the system. Approximately 60 ml of working fluid were then introduced in the test cell, but were not evacuated. Instead, that liquid was kept as a liquid layer for the experimental runs. At this point, the experimental system

was set to a fail-safe mode, which lasted through aircraft take-off. During this time, no work could be performed as research crew remained seated, separated from the experimental rigs on board the aircraft.

Once the aircraft reached a given altitude and experiments were allowed to be accessed, the controls and diagnostics systems were activated once again. At this point, the experiment proceeded similarly to the laboratory tests. The pressure in the test cell was set to a near null superheat, and a few impulsively superheated tests were conducted in order to ensure proper operating conditions. The pressure was controlled indirectly by changing the volume of the bladder in the manner already described. A complete check of all diagnostic systems was also conducted during this period.

As indications through the on-board g-meter display were given that a reduced-gravity cycle was about to begin, the impulsive superheat was applied to the film, in order to coincide with the reduce gravity duration. Once the microgravity cycle ended, conditions were set to a near null superheat. This process repeated for the next microgravity cycles. Various experimental procedures were tried during each of the two flights. One of these included conducting the experiment with the vacuum pump turned off, relying on the vacuum tanks to provide the "negative" pressure. Another approach was to impulsively apply the superheat, but rather than keeping a set pressure in the test cell, let the pressure slowly build up as the film evaporated.

4.5 Results

The experimental rig was flown aboard the Zero-G aircraft on two consecutive days. The first flight consisted of mainly troubleshooting while the second flight yielded a large amount of visual, ultrasound, and temperature/pressure data. All mechanical aspects of the system (pump, pressure control, volume-expansion system, heaters/cooler, diagnostics, etc.) functioned as

designed. The Martian- and Lunar-gravity intervals on the second flight day provided a useful opportunity to establish operating conditions prior to the start of the series of zero-g parabolae. In total 80 reduced-gravity parabola were flown.

The nominal low gravity duration provided by NASA (AOD 33899) is 23 seconds. However, significant g-jitter was encountered in essentially all reduced-gravity cycles. The fluctuations in gravity values have been reported to be as high as 0.02 g during the low gravity cycles [[46]] due to factors such as turbulence and pilot proficiency. These values are of the same order of magnitude as the low gravity levels measured during the current tests. The g-jitter, along with the brief negative-g intervals, resulted in shortened actual micro-gravity durations, and severe bulk motion of the fluid. Typical g-values experienced during reduced gravity cycles are shown in (Fig. 4.2). The initial spike to +0.01 g, seen in the figure between 2 and 4 seconds, had the most severe impact upon film stability. Taking the regular *g* direction to be negative, this reach into the positive range is equivalent to briefly and effectively inverting the test chamber. Since the fluid is not rigidly attached to the aircraft that resulted, in many cases, in the fluid moving off of the evaporating surface. This was confirmed visually and noted during the tests. The consequences of such bulk motion were that the liquid at the evaporating surface could not be thermally controlled and that the proposed experiment of a flat evaporating liquid from a constant temperature surface could not be reliably achieved. The temperature of the chamber walls was not regulated, therefore, liquid which came into contact with the relatively warmer walls in many cases, almost instantaneous resulted in boiling, which in some cases was observed as even occurring on the surface of the optical port, exactly opposite the intended test surface. It should be noted that the main cause of the positive g spike was to quickly reach reduced gravity

conditions at the beginning of each parabola. This is advantageous for many other experiments, but is extremely detrimental to the present one.

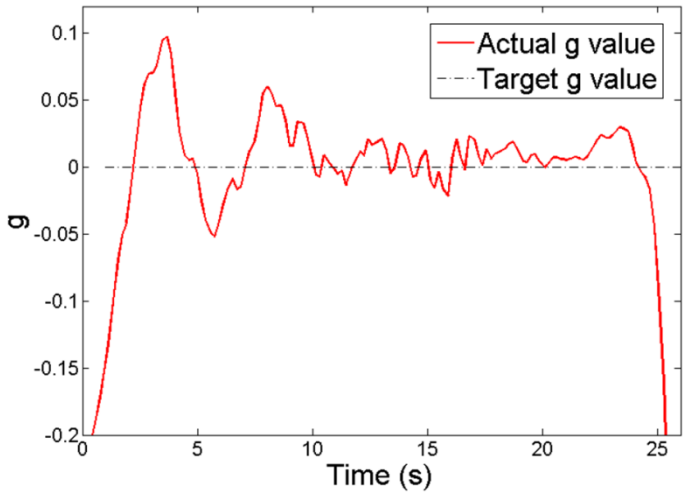

Figure 4.2. Typical *g*-loads experienced during a micro-gravity cycle aboard the aircraft. Notice the initial significant, upward acceleration at the start of the test interval.

Another undesired side effect of the bulk fluid motion was a low energy return of the ultrasound signal used to determine the film thickness, which rendered most thickness data unusable. Ultrasound techniques have been described before [[36]] and in Section 2.3.2 so a thorough discussion will not be included at this point. The typical aircraft post processed waveform looked as shown in Fig. 4.3. In it no resolvable film echo is present; hence, no film thickness it was able to be determined.

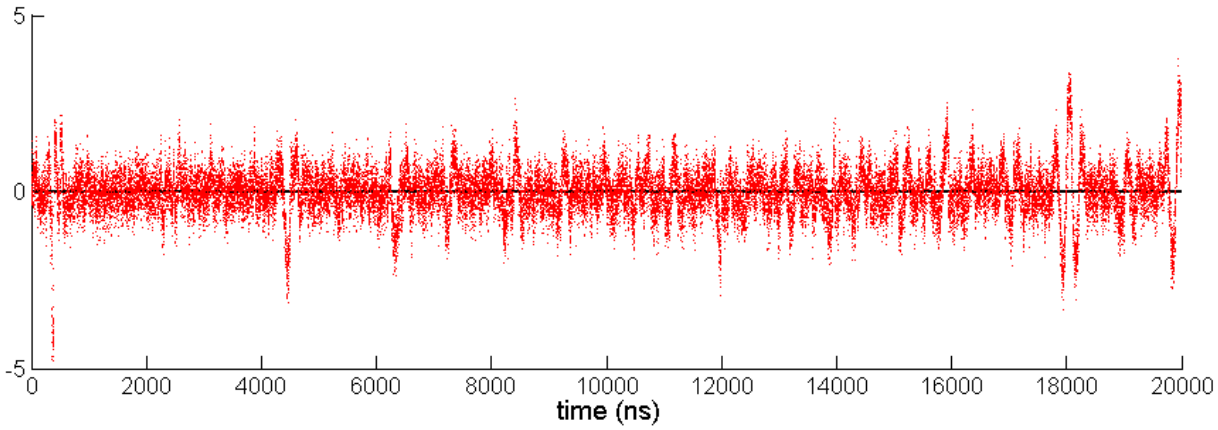

Figure 4.3. Representative processed ultrasound reading obtained during flight.

In order to confirm the proper operation of the ultrasound system, and to confirm that mechanical vibrations and bulk fluid motions indeed were the cause of the generally unusable data, laboratory experiments were run subsequent to the zero-g experiments with both undisturbed films and films subject to vibrations from the integrated vacuum pump as well as other artificially-induced mechanical vibrations. When the film was undisturbed mechanically, the post-processed files yielded quality fits to the data which can be interpreted, in turn, into the expected film thickness as seen in the laboratory experiments (Fig 4.4).

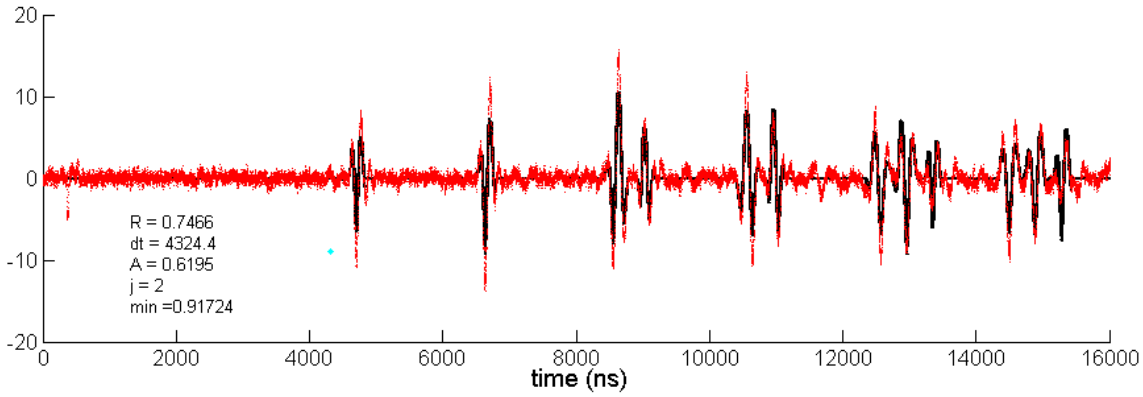

Figure 4.4. Processed ultrasound signal of a static, undisturbed film in the lab. The film thickness is approximately 4 mm. Acquired signal (red) and simulated signal (black).

Even after turning the vacuum pump on, and disturbing the system with an intensity similar to that experienced during the flight test (Fig 4.5), the signal was still usable (Fig 4.6) though the fitted R value was low (0.2267 for the signal shown below)

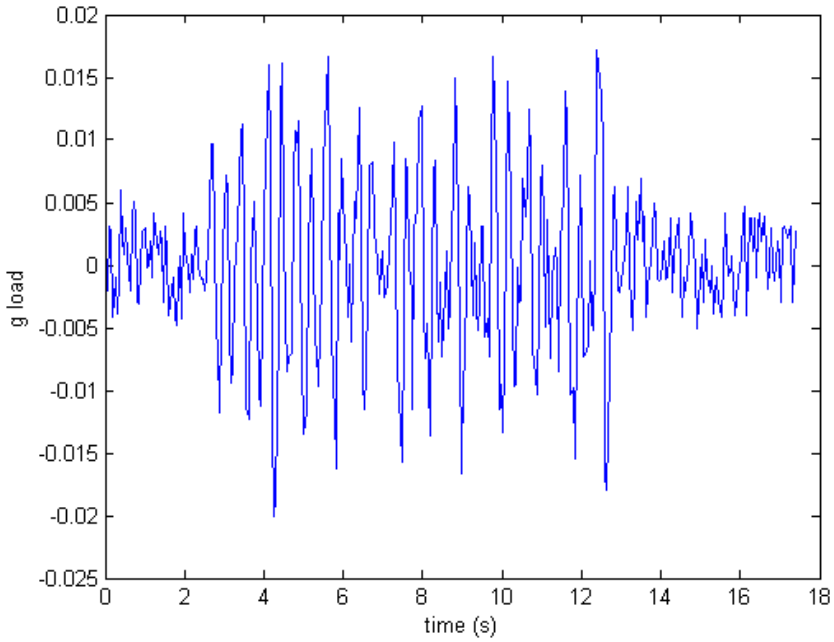

Figure 4.5. G-loading trace of "moderate" disturbances applied to a liquid film in standard lab (1 *g*) conditions

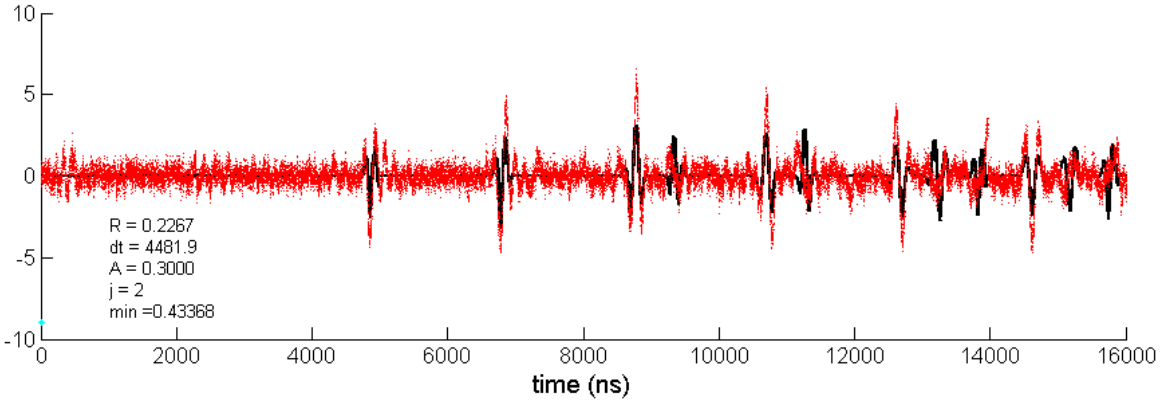

Figure 4.6. Processed ultrasound signal of a non-evaporating film, with the pump on, and moderately perturbed.Thickness is about 4 mm. Acquired signal (red) and simulated signal (black).

However, once the pump was on, and the system was mechanically perturbed with higher intensity (approximately twice in magnitude of the disturbances recorded on board the aircraft), as seen in Fig. 4.7, the data generated was essentially identical to that obtained during flight (Fig. 4.8). This indicates that motion due to aircraft vibrations, and not the vacuum pump, was the main source of noise during reduced-gravity tests. That lab disturbances of higher intensities were needed to achieve the same effects on the ultrasound signal as those observed during flight testing could reasonably be expected given the significant stabilizing effect of gravity upon the film in the laboratory. Film instabilities created by disturbances in the aircraft, particularly those experienced in the first few seconds of the microgravity cycle, can grow significantly faster if gravity is effectively null, but are damped out considerably quicker under normal-gravity conditions. This is in close agreement with published numerical simulations [[31]], which found that instabilities grow at a much faster rate in a reduced gravity environment than a standard 1-g. It should also be noted that the vacuum pump was shut off during some low-gravity cycles, which did not yield any appreciable improvement in the data.

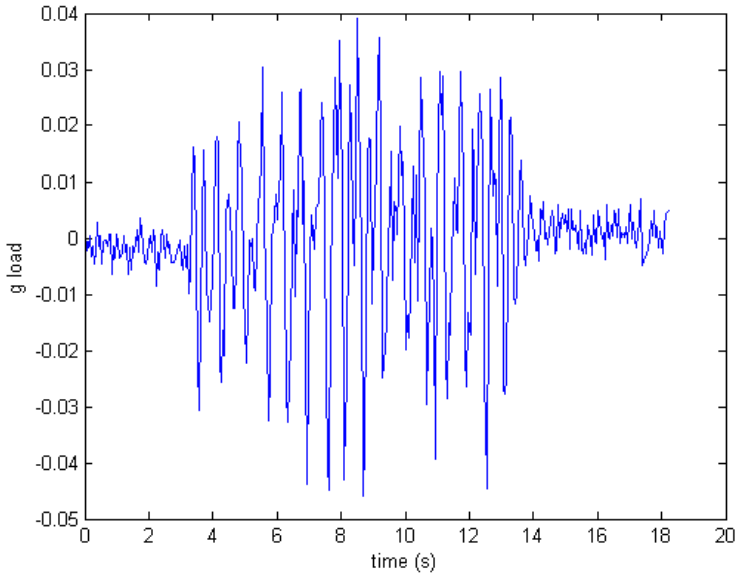

Figure 4.7. G-loading trace of disturbances applied to a liquid film in standard lab (1 *g*) conditions

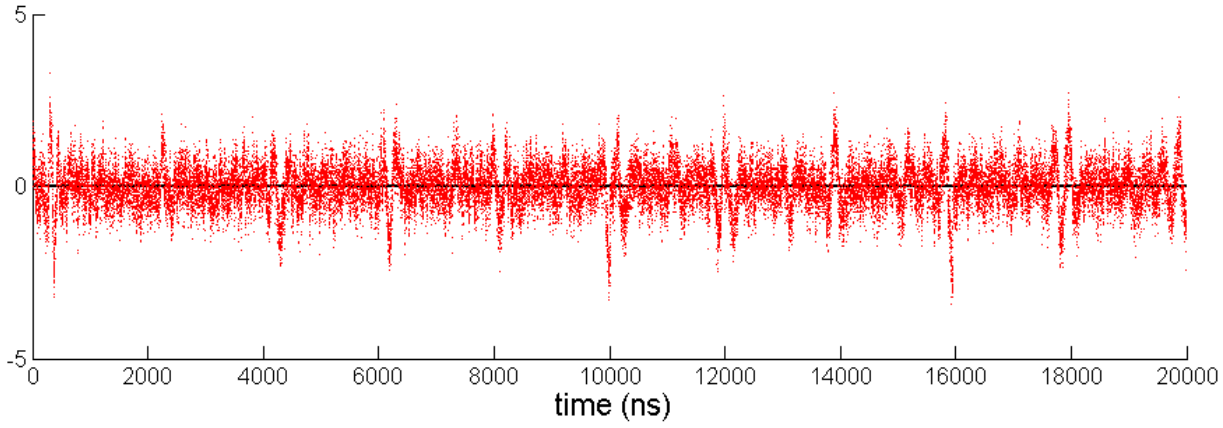

Figure 4.8. Processed ultrasound signal of a non-evaporating film, with the pump on, and mechanical vibrations. No film thickness can be resolved from the data.

The bulk motion the fluid during the reduced gravity cycles also had a negative effect on the quality of the shadowgraph images. The lifting fluid due to the upwards acceleration already referenced, in many cases reached the optical port, which resulted in unclear and low quality

shadowgraph images. Misalignments in the optical system resulting from the installation issues on board the aircraft, also contributed to the poor quality of the recorded images.

For the reasons mentioned above, which resulted in unstable evaporating films in zero-gravity, the test cell configuration should be redesigned in order to ensure the stability of the evaporating films during zero-g intervals. Ultimately, this may indeed point to a long-duration space experiment as the best platform to perform comprehensive studies of film evaporation under microgravity conditions. In that case, films can formed on the desired surface by condensation only, in a fashion similar to that which has successfully been employed in the laboratory at the UW, without introducing significant mechanical perturbations or gravity-level inversions, while also allowing for fully-sufficient test times.

Chapter 5. Conclusions

This work researched the behavior of evaporating films under unsteady conditions, in particular pressure-modulated superheating. Non-intrusive diagnostic techniques were employed, including a dynamic ultrasound thickness measurement system. From those measurements, the heat flux through the film surface could be calculated. The ultrasound system was determined to be accurate to ±10% of the film thickness while the precision was ±1μm. These tests validated the effective use of this ultrasound technique for the dynamic, non-intrusive measurement of the thicknesses of thin films. Convective structures and general film instabilities were recorded using a double-pass schlieren system. The main findings from each experiment are summarized below.

5.1. Comparison Experiments

The present results were compared with previous experiments by Kimball [30] for both the quasi-steady and impulsively superheated evaporating film cases. For all cases conducted, the results were in close agreement with those reported by Kimball in terms of dimensionless parameters, heat flux and convective evolution. For the case of impulsively superheated films, the heat flux peaks reported at t_1 and t_2 (conductive and convective respectively) were also observed in the present work. These time scales served as normalization parameters for phenomena studied in consequent experiments with t_1 being 1 second and t_2 being 11 seconds.

5.2. Pressure Modulated Evaporating Films under Slow Quenching Conditions.

These tests were conducted following several combinations of intervals where superheat was on or off. The interval duration was deemed “short” or conductive if it was approximately equal to t_1, and “long” or convective if it was close to t_2. It was concluded from these tests that

the quenching of the evaporation during the "off" portion of the cycle was not sufficient to reset the film to isothermal conditions, so unsteady effects resulted in final heat flux peak values which were consistently diminished in both magnitude and duration than those observed during the first cycle which was similar to an ISF (Impulsively-superheated Film). In addition, convective structure appears to persist in many cases even after evaporation is stopped. The convective structure evolution after just a few cycles also behaved differently than the typical ISF case, in some cases exhibiting a complex, multi-wavelength convective structure behavior not seen in under ISF or QS (Quasi-steady) conditions. No cycle combination from this type of quenching led to a gain in the total heat rejected when compared to the QS case.

5.3. Pressure Modulated Evaporating Films under PID Quenching Conditions

Experiments conducted following this quenching method were only the convective/convective type. This method did achieve a full isothermal reset of the film during quenching, however, this occurred at the expense of extremely diminished total evaporation rates due to high re-condensation levels during quenching cycles. In some cases convective structure appears within the film under pressure-modulated conditions even when the evaporation intervals are sufficiently short that conduction is expected to be the only heat transfer mode within the film.

5.4. Pressure Modulated Evaporating Films under Fast Quenching Conditions

Several cycle combinations were tried with this quenching method. Given the fast nature of the quenching, severe hydrodynamic disturbances resulted in large portions of the experiments yielding low quality data, or no data at all. The data that were collected prove useful in validating that these tests would yield the fastest evaporation rates. Also, just as in the case of the slow

quenching method, the heat flux and convective structure evolution underwent significant changes after just a few cycles. In some cases convective structure appears within the film under pressure-modulated conditions even when the evaporation intervals are sufficiently short that conduction is expected to be the only heat transfer mode within the film.

5.5. Quasi-Steady Evaporating Films with Mechanical Disturbance

A set of QS evaporating films were mechanically disturbed at their natural sloshing frequency in order to examine the impact of surface instabilities on evaporation rates. No changes to the constant evaporation rate were reported during, or after the mechanical disturbances were applied.

5.6 Reduced Gravity Experiments.

An experimental rig was built analogous to the one used in the lab to conduct ISF experiments, in order to explore ISF aboard NASA's reduced gravity aircraft. The goal was to observe fluid mechanics effects that are difficult to detect under terrestrial gravity, where buoyancy masks weaker phenomena. Inherent aircraft noise of both large and small magnitude (g-jitter) disrupted the stability of the films so no evaporation was observed in a controlled environment. Ground tests conducted post-flight validated the mechanical vibrations as the source of instabilities.

Chapter 6. Recommended Future Work

Several experiments in the field of film evaporation seem like a natural progression to the results discussed in the present work.

Findings were reported in this document related to the eddy velocity associated with convection in evaporating films. However, a more thorough investigation should be conducted, and is currently being proposed as a continuation to the work presented here, in order to measure the fluid velocities associated with the phenomena discussed in previous chapters. The proposed research involves the use of 3DPIV flow visualization technique, which allows for a true, instantaneous measurement of the eddy rotation velocity. Such technique could also potentially investigate the penetration depth of the eddies during the transient stages of evaporation.

It was shown in Chapter 4, when discussing the reduced gravity experiments that the stability of liquid films decreases with gravity. Therefore, true long-term, microgravity platforms are needed to successfully investigate film evaporation in the absence of gravity (i.e. ISS or sounding rockets). As mentioned previously, such experiments would lead to increase understanding of phenomena such as vapor recoil and *MB* instabilities.

Continued work with numerical simulations can also lead to increased understanding of the physical phenomena involved in film evaporation. CFD simulations continue to become more powerful, therefore, high fidelity models can be a key factor in guiding future experiments.

There are some specific recommendations to future experiments which can improve both the quality and quantity of data collected. For example, a constant challenge during all experiments was nucleate boiling. Nucleation almost always started at the interface between the Teflon jacket and the surface of the copper substrate. Since these were two separate parts that were assembled together, small imperfections existed along the edges. These imperfections

tended to trap gases, which in then turned to nucleation sites even at small superheat levels. This technical challenge can be avoided by eliminating this interface, and machining an evaporating surface from one piece of material. This change can significantly increase the ease of the experimental process.

Another challenge encountered during experiments stemmed from the hydrodynamic blowing effect that the incoming vapor from the generator had upon the liquid film. It can be recalled that such disturbances severely affected (and in some cases completely voided) measurement techniques. One way to address this problem is by eliminating the incoming vapor as the preferred method to null the superheat. A viable alternative would be to use high speed temperature controllers in future evaporating substrates, so that superheat can be controlled directly in the test cell. This method would eliminate mechanical moving parts which were also a source of disturbances during the experiments.

Bibliography

[1] Sashin, S. A. "Models for droplet transient heating: Effects on droplet evaporation, ignition, and break-up." *International Journal of Thermal Sciences*, pp. 610-622, 2005.

[2] Cammenga, H. "Evaporation Mechanisms of Liquids." *Current Topics in Materials Science, 5*, 1980

[3] Schatz, M. N. "Experiments on Thermocapillary Instabilities." *Annual Review of Fluid Mechanics, 33*, pp. 93-127, 2001.

[4] Umemura, A. "Interactive Droplet Vaporization and Combustion - Approach from Asymptotics." *Progress in Energy and Combustion Science, 20*(4), pp. 325-372, 1994.

[5] Luda, M. P. "Pyrolysis of fire retardant anhydride-cured epoxy resins." *Journal of Analytical and Applied Pyrolysis, 88*(1), pp. 39-52, 2010.

[6] Wang, H. G. "Characteristics of an evaporating thin film in a microchannel." *International Journal of Heat and Mass Transfer, 50*(19-20), pp. 3933-3942, 2007.

[7] Hill, S. A. "DRAFT Thermal Management Systems Roadmap – Technology Area 14." November 2010.

[8] Kim, J. C. "Design of an improved heater array to measure microscale wall heat transfer." *Third Microgravity Fluid Physics Conference*, pp. 165-170, Cleveland, OH, 1996.

[9] Hallinan, K. H. "Effects of thermocapillarity on an evaporating extended meniscus in microgravity." *Second Microgravity Fluid Conference*, pp. 247-252, Cleveland, OH, 1994.

[10] Faghri, A. K. "Evaporation on/in capillary structures of high heat flux two-phase devices." *Third Microgravity Fluid Physics Conference*, pp. 189-194, Cleveland, OH, July 1996.

[11] Ostrach, S. "Low-gravity fluid flows." *Annual Review of Fluid Mechanics*, pp. 313-345, 1982.

[12] Chun, K. S. "Heat transfer to evaporating liquid films." *Journal of Heat Transfer, 93*, pp. 391-396, 1971.

[13] Sharma, A. R. "Dynamics and Lifetimes of Thin Evaporating Liquid Films: Some Non-Linear Effects." *PhysicoChemical Hydrodynamics*, Vol. 10 , No. 5/6, pp. 675-691, 1998.

[14] Sharma, A. R. (1990). "Energetic Criteria for the Breakup of Liquid Films on Non-Wetting Solid Surfaces. *J. Colloid & Interface Science,* Vol. 137, No. 2, pp. 433-445, 1990.

[15] Oron, A. D. "Long-scale evolution of thin liquid films." *Reviews of Modern Physics,* Vol. 69, No. 3, pp. 931-980, 1997.

[16] Danov, K. A. "The stability of evaporating thin liquid films in the presence of surfactants. I. Lubrication approximation and linear analysis." *Phyics of Fluids,* Vol. 10, No. 1, pp. 131-143, 1998.

[17] Bankoff, S. "Taylor instability of an evaporating plane interface." *American Institute of Chemical Engineers,* Vol 7, pp. 485-487, 1961.

[18] Bankoff, S. "Stability of liquid film down a heated inclined plane." *International Journal of Heat and Mass Transfer,* Vol. 14, pp. 377-385, 1971.

[19] Yih, C. S. "Stability of parallel laminar flow down an inclined plane." *Physics of Fluids,* Vol. 6, pp. 623-628, 1963.

[20] Hosoi, A. "Evaporative instabilities in climbing films." *Journal of Fluid Mechanics,* Vol 442, pp. 217-239, 2001.

[21] Oron, A. "Formation of patterns induced by thermocapillarity and gravity." *Journal of Physics (France),* Vol. 2, pp. 131-146, 1992.

[22] Burelbach, J. B. "Nonlinear stability of evaporating/condensing liquid films." *Journal of Fluid Mechanics,* Vol. 195, pp. 463-494, 1988.

[23] Bénard, H. "Les tourbillons cellulaires dans une nappe liquide." *Rev. Gen. Sci. Pure Appl,* vol. 11, pp. 1261-1271, 1900.

[24] Rayleigh, L. "On convection currents ina horizontal layer of fluid when the higher temperature is on the under side." *Philosophical Magazine and Journal of Science,* Vol. 32, pp. 529-546, 1916.

[25] Koschmieder, E. L. *Bénard Cells and Taylor Vortices.* Cambridge University Press, 1993.

[26] Chandrasekhar, S. *Hydrodynamic and Hydromagnetic Stability*. Clarendon Press, 1961.

[27] Koschmieder, E.L., and Pallas, S.G. "Heat transfer through a shallow, horizontal convecting fluid layer." *Journal of Heat and Mass Transfer*, pp. 991 1002, 1974.

[28] Pearson, J. R. "On convecton cells induced by surface tension." *Journal of Fluid Mechanics,* Vol. 4, No. 5, pp. 489-500, 1958.

[29] Nield, D. A. "Surface tension and buoyance effects in cellular convection." *Journal of Fluid Mechanics,* Vol. 19, pp. 341-352, 1964.

[30] Kimball, J.T. “Interfacial Instability, Convective Structure, and Heat Transfer in Liquid Films Undergoing Phase Change.” Ph.D. Dissertation, University of Washington, 2010.

[31] Narendranath, A.D, *et al*. "The Effect of Gravity on the Stability of an Evaporating Liquid Film." *Journal of Microgravity Science and Technology*, pp. 189-199, 2014.

[32] Hinkenbein, T.E. and Berg, J.C. "Surface Tension Effects in Heat Transfer Through Thin Liquid Films.” *International Journal of Heat and Mass Transfer,* Vol 21, No. 9, pp. 1241-1249, 1978.

[33] Zhang, N., Chai, A. T. "Experimental Study of Marangoni-Bénard convection in a liquid layer induced by evaporation." *Experimental Heat Transfer*, Vol. 11, pp.187-2005, 1998.

[34] Behringer, R. P. and Ahlers, G. "Heat transport and temporal evolution of fluid flow near the Rayleigh-Bénard instability in cylindrical containers." *Journal of Fluid Mechanics*, pp. 219-258, 1982.

[35] Villarroel, F. "Heat transfer in fluids by Bénard convection." M.S. Thesis, University of Maryland, 1967.

[36] Kimball, J.T., Bailey, M.R. and Hermanson J.C. "Ultrasonic measurement of condensate film thickness." *The Journal of the Acoustical Society of America*, Vol. 124, No. 4, pp. 196-202, 2008.

[37] Segel, L.A, and Stuart, J.T. "On the question of the preferred mode in cellular thermal convection." *Journal of Fluid Mechanics*, Vol. 13, No. 2, pp 289- 306, 1962.

[38] Meyer, C.W., Ahlers, G., and Cannell, D.S., "Stochastic influences on pattern formation in Rayleigh-Bénard convection: Ramping experiments," *Physical Review A*, Vol. 44, No. 4, pp. 2514-2537, 1991.

[39] Garon, A. M, and Goldstein, R. J., “Convection, Velocity and Heat Transfer Measurements in Thermal Convection." *The Physics of Fluids*, Vol. 16, No. 11, pp. 1818-1825, 1973.

[40] Koschmieder, E. L., Biggerstaff, M. I. "Onset of surface-tension-driven Bénard convection." *Journal of Fluid Mechanics*, Vol. 167, pp. 49-64, 1986.

[41] Dubois, M. and Berge, P. "Experimental study of the velocity field in Rayleigh-Bénard convection." *Journal of Fluid Mechanics,* Vol. 85, No. 4, pp. 641-653, 1978.

[42] Silverman, S and Abramson, N. "Lateral Sloshing in Moving Containers." *The Dynamic Behavior of Liquids in Moving Containers*, pp. 13-78, 1966.

[43] Hill, S. A., Kostyk, C., Motil, B., Notardonato, W., Rickman, S., and Swanson, T., "DRAFT Thermal Management Systems Roadmap - Technology Area 14," National Aeronautics and Space Administration, November 2010.

[44] Weislogel, M.M., "Survey of Present and Future Challenges in Low-g Fluids Transport Processes," TDA Research, Inc., NASA Contract C-74461-N, 2001.

[45] Narendranath, A.D., Hermanson, J.C., Struthers, A.A., Kolkka, R.W. and Allen, J.S., "Stability of an Evaporating Liquid Film Under Nonequilibrium Conditions with Variable Gravity," *Proceedings of Fluids Engineering Division Summer Meeting, Microfluidics*, Paper no. FEDSM2012-72283, Puerto Rico, 2012.

[46] Kim, J., McQuillen, J., and Balombin, J. "Microheater Array Boiling Experiment," *AIAA*, Conference and Exhibit on International Space Station Utilization, October 2001.